

https://dspace.org/

An electron paramagnetic resonance study of proton induced damage in plastic scintillators for the ATLAS detector

Pelwan, Chad Dean

2017

http://hdl.handle.net/10539/23553

Pelwan, Chad Dean (2017) An electron paramagnetic resonance study of proton induced damage in plastic scintillators for the ATLAS detector, University of the Witwatersrand, Johannesburg, <http://hdl.handle.net/10539/23553>

Downloaded from a DSpace repository. https://dspace.org/

University of the Witwatersrand

An electron paramagnetic resonance study of proton induced damage in plastic scintillators for the ATLAS detector

Author:
Chad Pelwan (441424)

Principal Supervisor:
Prof. Bruce Mellado

Co-supervisor
Prof. Jonathan Keartland

Co-supervisor:
Prof. Daniel Joubert



A Dissertation submitted to the Faulty of Science, University of the Witwatersrand, Johannesburg, in fulfilment of the requirements for the degree of Master of Science.

April 2017

Declaration

I, Chad Dean Pelwan, declare that this Dissertation entitled, "An electron paramagnetic resonance study of proton induced damage in plastic scintullators for the ATLAS detector", and the work presented in it, are my own. It is being submitted for the Degree of Master of Science at the University of the Witwatersrand, Johannesburg. It has not been submitted before for any degree or examination at any other university.

Signed: 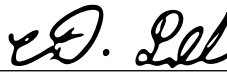

Date: 20/04/2017

"Well, I must endure the presence of a few caterpillars if I wish to become acquainted with the butterflies."

— Antoine de Saint-Exupéry, The Little Prince

Abstract

Plastic scintillators, situated in the Tile Calorimeter (TileCal) of the ATLAS detector at the Large Hadron Collider (LHC), play an integral part in the detection of diffractive, energetic hadronic particles that result from high energy proton-proton collisions. As these particles traverse the plastic, the resultant decay of the polymer base emits luminescent light which acts as a signature of this interaction. However, the deleterious radiation environment in which the plastics are situated ultimately degrade the plastic through the formation of free radicals which initiate chemical reactions and alter the structure of the plastic. Radical formation was studied using electron paramagnetic resonance (EPR) spectroscopy in six plastic scintillator types of either polystyrene (PS) or polyvinyl toluene (PVT) base, and computational EPR studies were conducted on two small monomer structures and two large polymer, plastic-like computer models. Damage was simulated in the computational models by removing an increasing number of hydrogen atoms. Plastic samples, of volume 500 $\times$500 $\times$ 250 µm, were to subjected protons accelerated to 6 MeV using the tandem accelerator at iThemba LABS, Gauteng, to increasing target doses of 0.8 MGy, 2.5 MGy, 8.0 MGy, 25 MGy, 50 MGy, and 80 MGy. The experimental EPR data taken after two weeks of the sample exposure to air indicate the presence of peroxy-type radicals that initiate chemical reactions, discolour the plastic, and decrease the efficiency of the plastic. Furthermore, the data suggests that damaged PS and PVT samples are susceptible to different mechanisms of radiation damage. However, results pertaining to the decrease in the g-factor and the increase in normalised EPR intensity suggest that all plastics behave similarly using an EPR analysis as a function of dose. Thus, the EPR analysis could not identify a specific plastic that would perform better than the existing plastics used in the TileCal. The computational chemical potential results indicate that electron transfer between damaged pristine and damaged models is possible. In the two small damaged models, the computational EPR data indicate the presence of a various stable akyl-like radicals depending on the site from which the hydrogen atoms are removed. In the two large damaged models, these results indicate a number of alkyl-, benzyl-, and cyclohexadienyl-like radicals.

To my parents, my sister, and Julia.

Acknowledgements

I wish to acknowledge Prof. Bruce Mellado for offering this project to me. I would also like to convey my sincere gratitude to my co-supervisors; thank you for early morning meetings and late night emails, for pushing me, supporting me, and believing in this project as much as I do. Thank you to Prof. Jonathan Keartland who showed me the ropes in the Magnetic Resonance lab, and who helped me "remain calm" through testing times. Dankie aan Prof. Daniel Joubert wat die studie verryk het met die DFT ontlyding, dat hy my ook geleer die belangrikste ding oor navorsing is om nooit te stagneer nie.

Thank you to iThemba LABS, Gauteng, for granting me permision to use the 3 MV tandem accelerator. To Dr. Morgan Madhuku, Mr. Fritz Baltzun and Mr. Oleg Pekar for assisting me with the sample irradiation, fine tuning the beam optics, and beam current analysis.

In addition, I would like convey thanks to the following people:

- Prof. Elias Sideras-Haddad for his encouragement and guidance throughout the project.
- Mr. Gerrard Peters for his assistance with sample polishing.
- Prof. Manuel Fernandes for finding and creating the computational models, and assistance in understanding radiation damage on a molecular scale.
- Dr. Moise Dongho Nguimdo for assisting me with the initial DFT calculations.
- Dr. Vincenzo Marsicano and Mr. Will Wright for their assistance with the EPR spectrometer.
- The office of P242, in particular: Rob, Stef, Shell-May, Harshna, and Scotty.
- My family.
- My friends and colleagues.

I wish to express my gratitude to the National Research Foundation (NRF) and iThemba LABS for financial support. The opinions expressed and conclusions arrived at, are those of the author and are not necessarily to be attributed to the NRF or iThemba LABS.

Contents

Declaration ii

Abstract iv

Acknowledgements vii

Contents ix

List of Figures xiii

List of Tables xvii

Nomenclature xix

1 Introduction 1
- 1.1 Motivation of Investigation . . . 1
- 1.2 Aims and Objectives . . . 4
- 1.3 Dissertation Outline . . . 5

2 The ATLAS Experiment 7
- 2.1 The ATLAS Detector . . . 8
  - 2.1.1 The Tile Calorimeter . . . 10
  - 2.1.2 Minimum Bias Trigger . . . 12
  - 2.1.3 Radiation Environment in the ATLAS Detector . . . 13

3 Overview of Scintillators and Radiation Damage 15
- 3.1 Introduction . . . 16
- 3.2 Interaction of Charged Particles with Matter . . . 16
  - 3.2.1 Stopping Power . . . 18
- 3.3 Luminescence in Organic Molecules . . . 20
- 3.4 Plastic Scintillators . . . 23
  - 3.4.1 Scintillator Manufacturing Process . . . 25
- 3.5 Applications of Scintillators . . . 25
  - 3.5.1 Scintillation Detectors . . . 26
- 3.6 Effects of Radiation Damage in Plastic Scintillators . . . 27
  - 3.6.1 Gas Evolution and Free Radical Formation . . . 28
  - 3.6.2 Cross-linking and Unsaturation . . . 29
  - 3.6.3 Effects on Optical Properties . . . 29

3.6.4 Exposure to Oxygen and Recovery 30

4 Electron Paramagnetic Resonance: Theory and Applications 31
4.1 Magnetic Moment and Angular Momentum 32
4.1.1 Spin Magnetic Moment 33
4.1.2 Magnetic Field Quantities and Units 33
4.1.3 Paramagnetism 34
4.2 Electron Paramagnetic Resonance 34
4.2.1 Resonance Theory 35
4.2.2 Spin Relaxation and Resonance Line Shape 36
4.2.3 Chemical Shifts and the Effective g-factor 39
4.3 The Spin Hamiltonian 40
4.3.1 The Electron-Zeeman Interaction 41
4.3.2 The Zero-Field Interaction 44
4.3.3 The Hyperfine Interaction 44
4.4 Organic Molecules in the Triplet State 45
4.5 EPR Signal Changes in Irradiated Plastics 46
4.6 Density Functional Theory 47
4.6.1 Magnetic Shielding 49
4.6.2 GIPAW Method 50
4.6.3 Calculation of EPR Parameters 51
4.6.4 Chemical Potential Calculations 51

5 Experimental and Computational Techniques 53
5.1 Monte Carlo Simulations of Damaged Plastics 54
5.2 Investigated Plastic Scintillators 55
5.3 Scintillator Sample Preparation 56
5.4 Sample Irradiation 59
5.4.1 Absorbed Dose Calculation 61
5.5 Continuous-wave EPR Spectroscopy 62
5.6 Computational Models 66
5.6.1 Structural Relaxation 68
5.6.2 QE-GIPAW Calculations 69

6 Results and Observations 71
6.1 Discolouration and Brittleness 71
6.2 Experimental EPR Results and Observations 72
6.2.1 Spectral Shift 72
6.2.2 Relative Decrease in g-factor 73
6.2.3 Peak-to-peak Variation 74
6.2.4 Relative Intensity Increase 75
6.2.5 Shoulder Formation 76
6.3 Computational Results and Observations 77
6.3.1 Chemical Potential Results 77
6.3.2 Simulated EPR Spectra 78

7 Discussion 83
7.1 Experimental Results Discussion 83

7.1.1 Discolouration Following Irradiation . . . 83
7.1.2 Spectral Shape . . . 84
7.1.3 Normalised Intensity Increase . . . 85
7.1.4 Decrease in g-factor . . . 86
7.1.5 Peak-to-peak Variation . . . 86
7.1.6 Summary . . . 87
7.2 Computational EPR Discussion . . . 88
7.3 Future Work . . . 89

8 Conclusion **91**

Bibliography **106**

A Analysis of Experimental Parameters **107**
A.1 Integrated EPR Spectra Fits . . . 107
A.2 Integrated Current Analysis . . . 114
A.3 Key Parameter Values . . . 114

B Computational Parameters **123**
B.1 EasySpin EPR Simulation Code . . . 123
B.2 EPR Spectrum Averaging . . . 125
B.3 Chemical Potential Results for Toy Model . . . 126

C Performance of $E_{\mathrm{T}}^{\mathrm{miss}}$ in the Search for a Higgs boson with a Di-photon Decay at $\sqrt{s} = 13$ TeV **129**
C.1 The Madala Hypothesis . . . 130
C.2 Data and Sample Simulation . . . 130
C.3 Reconstruction and Identification of Objects . . . 131
C.3.1 Jet Selection . . . 131
C.3.2 Photon Selection . . . 131
C.3.3 Lepton Selection . . . 131
C.3.4 Overlap removal . . . 132
C.3.5 $E_{\mathrm{T}}^{\mathrm{miss}}$ Reconstruction . . . 132
C.4 Event Selection and Categorisation . . . 134
C.5 Results . . . 135
C.5.1 $E_{\mathrm{T}}^{\mathrm{miss}}$ Muon TST Distribution . . . 135
C.5.2 $E_{\mathrm{T}}^{\mathrm{miss}}$ RefTau TST Distribution . . . 136
C.5.3 $E_{\mathrm{T}}^{\mathrm{miss}}$ RefEle TST Distribution . . . 137
C.5.4 $E_{\mathrm{T}}^{\mathrm{miss}}$ RefGamma TST Distribution . . . 138
C.5.5 $E_{\mathrm{T}}^{\mathrm{miss}}$ RefJet TST Distribution . . . 139
C.5.6 $E_{\mathrm{T}}^{\mathrm{miss}}$ Total TST Distribution . . . 140
C.5.7 Sum of $E_{\mathrm{T}}^{\mathrm{miss}}$ for TST . . . 143
C.6 Conclusion . . . 144

List of Figures

2.1 An illustration of the ATLAS detector. 8
2.2 The TileCal of the ATLAS detector. 10
2.3 Regular integrated read-out module including various components in the TileCal. 11
2.4 A segmentation of the TileCal modules displaying ITC scintillator positions relative to the readout cells. 12
2.5 Dimensions of the MBTS and its distance from the IP. 13
2.6 Simulated radiation contour map of the total ionising dose in the TileCal region over one year. 14

3.1 A classical depiction of an undistributed trajectory of a charged particle where a is the atomic radius and b is the impact parameter. 17
3.2 Stopping of H ions in polystyrene. 20
3.3 Jablonski energy level diagram for an organic molecule with π-electrons. . . . 22
3.4 Representation of MO bonding in a benzene molecule. 23
3.5 Monomers of PS and PVT used as bases in plastic scintillators. 24
3.6 Common primary (PTP) and secondary (POPOP) fluors added to plastic scintillators to aid scintillation. 25
3.7 Schematic of a photomultiplier tube connected to a scintillator. 27
3.8 Benzyl radical (a) and cyclohexadienyl-type radical (b) that form in irradiated PS. 28
3.9 Diffusion of oxygen into styrene forming an unstable peroxy intermediate which further forms stable products and radicals. 30

4.1 An infinitesimal magnetic moment, $d\vec{\mu}$, due to a current loop. 32
4.2 Electron spin levels in a magnetic field for a spin 1/2 system. 36
4.3 First derivative of a Lorentzian line indicating the peak-to-peak width. 38
4.4 Sample coordinate system and the magnetic field vector in a unit sphere defining the elevation and azimuthal angles and the absorption and derivative EPR line shape for a randomly orientated sample with axial symmetry, respectively 43
4.5 Triplet energy levels in an organic molecule. 46
4.6 Magnetic shielding for the nuclear sites in isolated molecules for the all-electron response. 50

5.1 TRIM simulation of 6 MeV hydrogen ions traversing PS and the ion ranges for PS and PVT. 54
5.2 Photographs of the six plastic scintillators used in the study (not pictured to scale). 56

5.3 Photographs of the Buehler IsoMet low speed saw and the bottom and top view of the aluminium holders. . . . 57
5.4 Photograph of the Struers metallographic polishing machine and aluminium sample holders. . . . 58
5.5 Photograph of a completed (Dubna) sample mounted into a brass holder with putty-like adhesive. . . . 58
5.6 A computer generated representation of the tandem accelerator at iThemba LABS, Gauteng. . . . 59
5.7 Photograph of beam line leading to the microprobe chamber. . . . 60
5.8 Photograph of the nuclear microprobe connected to the carousel with sample holder in place. . . . 61
5.9 Schematic of a CW X-band EPR spectrometer. . . . 62
5.10 A cylindrical microwave cavity and an EPR critically coupled resonator indicating the microwave magnetic and electric field components in the TE011 mode. . . . 63
5.11 Low temperature EPR set up. . . . 65
5.12 A computationally generated representation of damaged toy model styrene monomer, with two hydrogen atoms removed. Hydrogen and carbon atoms are represented by the red and grey spheres, respectively. . . . 66
5.13 A computer genated representation of a MUKLAF molecule and the complete MUKLAF model. . . . 67
5.14 A computer genated representation of a PolySty molecule and the complete PolySty model. . . . 68

6.1 Effect of dose on EPR spectra for each plastic scintillator type taken at 80 K within 2 weeks of irradiation. . . . 72
6.2 Effect of dose on the relative change in the g-factors at 80 K. . . . 74
6.3 Effect of dose on the peak-to-peak width at 80 K. . . . 75
6.4 Effect of dose on the relative intensities normalised to the volume of the irradiated spot. . . . 76
6.5 Simulated EPR spectra for all models. Pristine models are represented by solid black lines whereas the damaged models are represented by the solid green, blue, and red lines for the 1, 2, and 3 hydrogen atom removal. . . . 79
6.6 Simulated EPR spectrum of radical with **A**-tensor principle values set to zero, and the integrated EPR spectrum with fit. . . . 80
6.7 Simulated EPR spectrum of radical from a damaged PolySty model with two hydrogen atoms removed which include hyperfine parameters. . . . 81

A.1 Triple Gaussian fits for all EJ200 samples at 80 K. Misfits to spectra can be attributed to the low number of data points around the central peak. However, increasing bin size resulted in skewed fit. . . . 108
A.2 Triple Gaussian fits for all EJ208 samples at 80 K. . . . 109
A.3 Triple Gaussian fits for all EJ260 samples at 80 K. . . . 110
A.4 Triple Gaussian fits for all Bicron samples at 80 K. . . . 111
A.5 Triple Gaussian fits for all Protvino samples at 80 K. . . . 112
A.6 Triple Gaussian fits for all Dubna samples at 80 K. . . . 113
A.7 Beam current for irradiated EJ200 samples. . . . 115
A.8 Beam current for irradiated EJ208 samples. . . . 116
A.9 Beam current for irradiated EJ260 samples. . . . 117

A.10 Beam current for irradiated Bicron samples. 118
A.11 Beam current for irradiated Dubna samples. 119
A.12 Beam current for irradiated Protvino samples. 120

B.1 A computer generated model of the labelled, damaged Styrene model. 125
B.2 Averaging of EPR spectrum for vinyl toluene model for a single hydrogen atom removed for various sites on the monomer. 126

C.1 The production mechanism of H via gluon-gluon fusion (a), and the decay of H to two dark matter candidates, χ, and a Higgs boson, h. 130
C.2 Control plots for the TST terms for the total $E_{\mathrm{T}}^{\mathrm{miss}}$ muon distribution. . . . 135
C.3 Control plots for the TST terms of the $E_{\mathrm{T}}^{\mathrm{miss}}$ RefTau distribution. 136
C.4 Control plots for the TST terms of the $E_{\mathrm{T}}^{\mathrm{miss}}$ RefEle distribution. 137
C.5 Control plots for the TST terms for the total component of $E_{\mathrm{T}}^{\mathrm{miss}}$ RefGamma distribution. 138
C.6 Control plots for the TST terms for the total component of $E_{\mathrm{T}}^{\mathrm{miss}}$ RefJet distribution. 139
C.7 Control plots for the TST terms for x-component of $E_{\mathrm{T}}^{\mathrm{miss}}$ Total distribution. 140
C.8 Control plots for the TST terms for y-component of $E_{\mathrm{T}}^{\mathrm{miss}}$ Total distribution. 141
C.9 Control plots for the TST terms for the total component of $E_{\mathrm{T}}^{\mathrm{miss}}$ Total distribution. 142
C.10 Control plots for the TST terms for the sum of $E_{\mathrm{T}}^{\mathrm{miss}}$ distributions. 143

List of Tables

3.1 Variable meanings and values in the Bethe-Bloch Equation. 18

5.1 Investigated plastic scintillators and relevant properties. 55

A.1 Key parameter values for EJ200, EJ208, and EJ260. 121
A.2 Key parameter values for Bicron, Dubna, and Protvino. 122

B.1 Chemical potential and the absolute value of first DFT excitation for both majority and minority spin channels for the single hydrogen atom removal in the Vinyl toluene model. 127
B.2 Chemical potential and the absolute value of first DFT excitation for both majority and minority spin channels for the two hydrogen atom removal in the Vinyl toluene model. 128

C.1 The four optimised categories utilised in the study. 134

Nomenclature

Acronyms

AO Atomic Orbital

ATLAS A Toroidal LHC Apparatus

BR Branching Ratio

BSM Beyond Standard Model

BZ Brillouin Zone

CAB Core and Bond

CERN Organisation européenne pour la recherche nucléaire

CMS Compact Muon Solenoid

CW Continous Wave

DFT Density Functional Theory

EB Extended Barrel

EM Electromagnetic

EPR Electron Paramagnetic Resonance

FRET Förster Resonance Energy Transfer

GIPAW Gauge Including Projected Augmented Wave

HEP High Energy Physics

HO Highest Orbital

ID Inner Detector

IP Interaction Point

ITC Intermediate Tile Calorimeter

LABS Laboratory for Accelerator-Based Sciences

LAr Liquid Argon

LB Long Barrel

LDA Local Density Appromixation

LHC Large Hadron Collider

MBTS Minimum Bias Trigger Scintillators

MeV Mega Electronvolt

MO Molecular Orbital

NMR Nuclear Magnetic Resonance

PAW Projected Augmented Wave

PMT Photomultiplier Tube

POPOP Di-phenyloxazolyl

ppm Parts Per Million

PS Polystyrene

PTP p-Terphenyl

PVT Polyvinyl toluene

QCD Quantum Chromodynamics

QE Quantum Espresso

SCT Semiconductor Tracker

SNICS Source of Negative Ions by Caesium Sputtering

SO Spin Orbit

SRIM Stopping Range of Ions in Matter

TileCal Tile Calorimeter

TRIM Transport of Ions in Matter

TRT Transition Radiation Tracker

TST Track Soft Term

USPP Ultrasoft Pseudopotential

UV Ultraviolet

VASP The Vienna Ab Initio Simulation Package

XC Exchange-correlation

Symbols

$\Delta\mathbf{g}$ Deviation from **g**-tensor (with respect to free electron **g**-tensor)

ΔB_{pp} Peak-to-peak width of EPR spectrum

Δg Deviation from g-factor (with respect to free electron g-factor)

η Pseudorapidity

$\sqrt{s}$ Centre-of-mass energy

$\varepsilon_{\mathrm{HO}}$ Highest occupied Kohn-Sham eigenvalue

E_{cut} Energy cut-off

E_{loss} Average energy lost per particle

g g-factor

g_0 g-factor of un-irradiated spectrum

g_{a} g-factor of secondary peak obtained from fit

I_0 Normalised intensity of un-irradiated spectrum

p_{T} Transverse particle mometum

pp Proton-proton

$E_{\mathrm{T}}^{\mathrm{miss}}$	Transverse missing energy
A	Hyperfine tensor (with pricipal components A_{xx}, A_{yy}, and A_{zz})
g	**g**-tensor (with pricipal components g_{xx}, g_{yy}, and g_{zz})
Å	Angstrom
Cs	Caesium
S/N	Signal-to-noise ratio

Chapter 1

Introduction

Plastic scintillators are organic hydrocarbon compounds capable of detecting energetic particles and ionising radiation. The interaction results in electronic excitations of the aromatic polymer structure which de-excites through a process (known as fluorescence) where light, usually in the UV-visible region, is emitted [1]. This light acts as a signature for the interaction. The quick time-of-flight measurements of the scintillator make them an integral part of many scientific and industrial fields where there is a need to detect and identify energetic particles [2]. This has applications in physics, and in particular in high energy physics (HEP). Here, plastic scintillators are used to indirectly measure the charge and momentum of energetic particles that traverse the material. Information is then relayed to a larger, more complex detection system and is used to reconstruct the trajectories of, and other important parameters associated with, the particle.

1.1 Motivation of Investigation

The Large Hadron Collider (LHC) is based at l' Organisation européenne pour la recherche nucléaire (CERN) near Geneva, Switzerland. It is the largest particle accelerator and HEP experiment built to date and, during the Run I data taking period (2009 - 2012), operated at

a centre of mass energy, $\sqrt{s}$, of 7 TeV from proton-proton (pp) collisions. Centred at one of the eight collision points of the LHC, is a general purpose detector referred to as the ATLAS (A Toroidal LHC Apparatus) detector.

In July of 2012, ATLAS, along with another general purpose detector CMS (Compact Muon Solenoid) also located at the LHC, independently announced the discovery of the SM Higgs Boson [3, 4] in pp collisions at an integrated luminosity of approximately 4.8 fb^{-1} and 5.9 fb^{-1}, respectively. The discovery of the Standard Model (SM) Higgs boson completed [3] the SM theory, which is a quantum field theory of elementary particles that unifies three of the four fundamental interactions: the strong, weak, and electromagnetic [5].

By interacting with the Higgs field and its associated mediator, the Higgs boson, massless subatomic particles such as bosons and fermions gain mass through the so-called Higgs Mechanism. This mechanism is a result of a spontaneous symmetry breaking which results in a non-zero scalar field that couples to the gauge fields of the bosons and fermions. This coupling results in mass terms that correspond to these subatomic particles.

However, since its discovery, a multitude of unexplainable features associated with the Higgs boson [6], its decays [7], and its productions [8] have been observed that do comply with the SM predictions from both ATLAS and CMS. In an attempt to explain theses features, The HEP group at the University of the Witwatersrand[1] have suggested the existence of a heavy scalar "Madala" boson, H, which couples to an intermediate scalar, S, and then to a dark matter candidate, χ, as well as other SM particles. The dark matter candidate is a possible source for missing transverse energy ($E_{\mathrm{T}}^{\mathrm{miss}}$) that could explain the excesses observed [9]. Using this model, it was hypothesised that the Higgs would "recoil" against χ thus gaining transverse momentum, p_{T}. A study was conducted for the search of events with large $E_{\mathrm{T}}^{\mathrm{miss}}$ and a Higgs boson decaying to two photons using 3.2 fb^{-1} of pp collisions at $\sqrt{s} = 13$ TeV with the ATLAS detector [10]. The author had contributed to it by investigating the reconstruction of $E_{\mathrm{T}}^{\mathrm{miss}}$. These plots, along with a brief discussion on the analysis, are presented in Appendix C.

Currently, the LHC operates at $\sqrt{s} = 13$ TeV which was reached at the start of Run II (2015 - 2018). The LHC intends to increase its integrated luminosity by a factor of ten by 2022. Several upgrades have already been implemented at the LHC in 2015 and, in the upcoming years, the detection systems and accelerator technologies are to be replaced to accommodate

[1] For more information please visit: http://hep.wits.ac.za

the increase in energy and luminosity [11]. In particular, a sub-detector within ATLAS, referred to as the Tile Calorimeter (TileCal), employs plastic scintillators [12] in its detection system. These scintillators exhibit luminescence through their interaction with ionising, energetic particles. Their relatively high light output, and high resolution capabilities make them are a vital component in the detection of subatomic particles such as quarks, gluons, and hadronic jets. However, the subsequent increase in luminosity significantly impacts the radiation environment of the TileCal and the plastic scintillator [13]. It is, therefore, imperative that these components withstand the deleterious effects of this environment. If this is not possible, they are to be replaced in preparation for the increased energy and luminosity.

The ionising effects on the plastic scintillators due to their interaction with energetic particles result in the formation of excited species, referred to as free radicals. These radicals form when bonds in the plastic polymer break, and they initiate chemical reactions that alter the structure of the plastic which ultimately damage it [14]. Damaged plastic scintillators display decreased light output compared to their un-damaged counterparts [15], and this continues to decrease as damage increases [16]. Understanding the radicals which initiate the damage to the plastic scintillators could be of assistance when choosing a scintillator that shows the most resistance to radiation.

The upgrade of the plastics in the TileCal scheduled for 2018 intends to replace those scintillators which have received the most damage with more radiation resistant ones. This investigation seeks to determine the radials formed when plastic scintillators are ionised by energetic particles, and the changes they induce in the plastics. Plastic scintillators of either polystyrene (PS) or polyvinyl toluene (PVT) base are investigated. These plastics are irradiated with relatively low energy 6 MeV protons. The iThemba Laboratory for Accelerator-Based Sciences (LABS), Gauteng, provided the facilities necessary to accelerate the protons. Six grades of scintillators were investigated during this investigation: three PVT based Eljen Technology plastics, one PVT based plastic developed by Saint Gobain Crystals, one PS based IHEP (Institute of High Energy Physics) plastic, and one PS based ISMA (Institute for Scintillating Materials of National Academy of Sciences of Ukraine) plastic. Electron paramagnetic resonance was used to investigate the radical formation in each of the plastics before and after irradiation.

In addition to this, in an attempt to quantify the damaged incurred by the plastics, a computational investigation into four plastic-like models was undertaken. Damage was

modelled by simply removing atoms from the system.

1.2 Aims and Objectives

The primary aim of this investigation is to gain a comprehensive understanding of the effects of proton-induced radiation damage on plastic scintillators. These energies are much smaller in magnitude when compared to those utilised in high energy particle detectors. The investigation further aims to understand the molecular and structural changes undergone in the plastic scintillators by investigating the possible radical formation induced by the proton interaction.

The investigation will also aim to perform a comparative study by investigating effects of radiation damage in a number of plastic scintillators with different molecular structures and added dopants. Furthermore, it aims to computationally reconstruct approximate plastic structures and the ionising effects to them produced by the protons.

The information gained from the comparative investigation and the computational modelling could assist in choosing a plastic scintillator to replace those currently employed in the Tile Calorimeter (TileCal) of the ATLAS detector during the Phase 2 upgrade in 2018. This investigation could possibly shed light on the deterioration of the mechanism responsible for scintillation.

To achieve these aims, the following objectives have been set:

1. Perform electron paramagnetic resonance spectroscopy on various proton irradiated plastic scintillators exposed to increasing absorbed dose.
   - Study the possible long-lived radical formation and any other structural changes.
2. Perform a computational DFT electron paramagnetic resonance on smaller, damaged plastic-like models.
   - Replicate experimental signal structures.
   - Study short-lived radicals and any other structural changes.

1.3 Dissertation Outline

This dissertation is divided into eight chapters. The first chapter presents the motivation of the investigation and the aims and objectives that were set. The second chapter details the structure and importance of the ATLAS detector, and deleterious radiation environment that plastic scintillators are exposed to. Chapter three presents the literary overview of radiation damage in scintillators. Chapter four presents the theoretical background utilised in electron paramagnetic resonance and its computational calculations. The details of the sample preparation, apparatus utilised, and experiments are detailed in chapter five. In chapters six and seven, the results and observations, and associated analysis and discussion are presented, respectively. Chapter eight presents the conclusions of findings from the investigation. In addition, a brief summary of each chapter is presented at the beginning of chapters 2, 3, 4, and 5.

Chapter 2

The ATLAS Experiment

In this chapter the ATLAS detector at the Large Hadron Collider and it's main components are introduced. Emphasis is placed on the TileCal and the plastic scintillators employed in and around it; the minimum bias trigger scintillators are discussed in a similar manner. Finally, the radiation environment these plastic scintillators experience is discussed along with the consequences of prolonged exposure.

2.1 The ATLAS Detector

Centred at one of the collision points at the CERN LHC is the ATLAS detector [17]. This general purpose detector illustrated in Figure 2.1 is 46 metres in length, 25 metres in height, and weighs approximately 7000 metric tonnes.

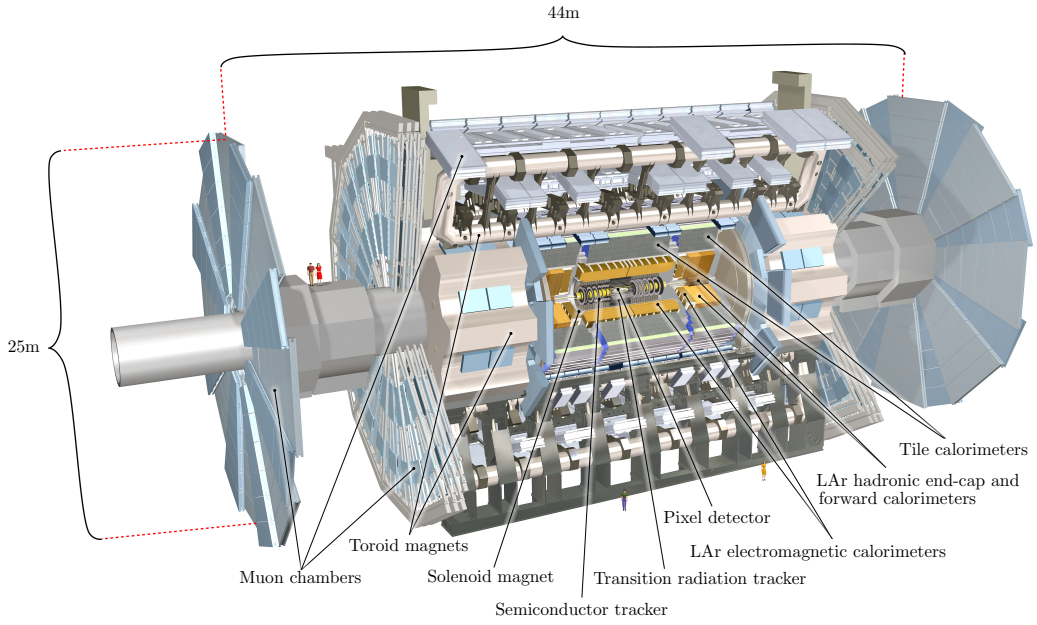

FIGURE 2.1: An illustration of the ATLAS detector [CERN©].

The beam pipe, which extends along a 27 km long radius around the LHC, is situated at the centre of the cylindrically symmetric detector. Travelling along the beam pipe, are two beams of bunched protons which collide at the so-called interaction point (IP) at the centre of the detector. The energies and paths of the emergent particles produced after this collision is recorded through their interaction with the detector.

The co-ordinate system ATLAS employs [18] is defined by the IP which is set as the origin. The z-axis is defined along the beam axis and the perpendicular x-y plane defines the transverse plane which is used when making measurements on particle momenta, referred to as p_T. The subsequent dimensions and angles used to define spatial co-ordinates in this system are therefore r, the radical dimension which measures the distance between an event and the beam, and ϕ, the azimuthal angle, around the beam axis. However, the usual polar angle θ which measures angles from the x-axis around the beam axis is replaced by

pseudorapidity, $\eta \equiv \ln \tan(\theta/2)$ which is Lorentz boost invariant. Using this convention, the spatial properties between two objects is calculated as $\Delta R = \sqrt{\Delta\phi^2 + \Delta\eta^2}$.

ATLAS is composed of four main components, each sensitive to the various types of particles produced after collisions. These components, shown in Figure 2.1, are the Inner Detector (ID), the magnetic system, the muon spectrometer, and the electromagnetic (EM) and hadronic calorimeters.

The ID [19] with $|\eta| < 2.5$ consists of three sub-detectors: the Pixel detector, the Semiconductor Tracker (SCT), and the Transition Radiation Tracker (TRT). These sub-detectors aid the ID in determining the momenta of charged particles. A 2 Tesla magnetic field curves the trajectories of charged particles forming tracks and resulting in ionisation. Two technologies along with millions of channels are used to reconstruct the vertices of these particles. Silicon microstrips are employed in the Pixel detector and SCT to detect ionising radiation.

The calorimeters have a coverage up to $|\eta| = 4.9$. They encapsulate the ID and utilise different technologies in order to measure energies of electrons, hadrons and photons. The calorimeters are comprised of the EM calorimeter, Tile calorimeter (TileCal), forward calorimeter, and end-cap calorimeters. The calorimeters "sample" a fraction of energy from incident particles which produce showers of energy. The TileCal is discussed in more detail in Section 2.1.1.

The Muon spectrometer surrounds the calorimeters and detects muons. Muon tracks are bent by the magnetic field of eight toroidal magnetics; these curve the trajectories of the muons.

2.1.1 The Tile Calorimeter

The TileCal [12], depicted in Figure 2.2, is a central part of the ATLAS detector along with the liquid argon (LAr) detector. These detectors make measurements on and identify hadrons, taus, leptons, and in particular a shower of additional particles (quarks and gluons) referred to as jets [20]. Not directly measured but rather reconstructed by the TileCal, is transverse missing energy ($E_{\mathrm{T}}^{\mathrm{miss}}$) which is a measure of the presence of undetectable particles being produced in the collisions. These include neutrinos or hypothetical particles which have similar properties to the neutrino.

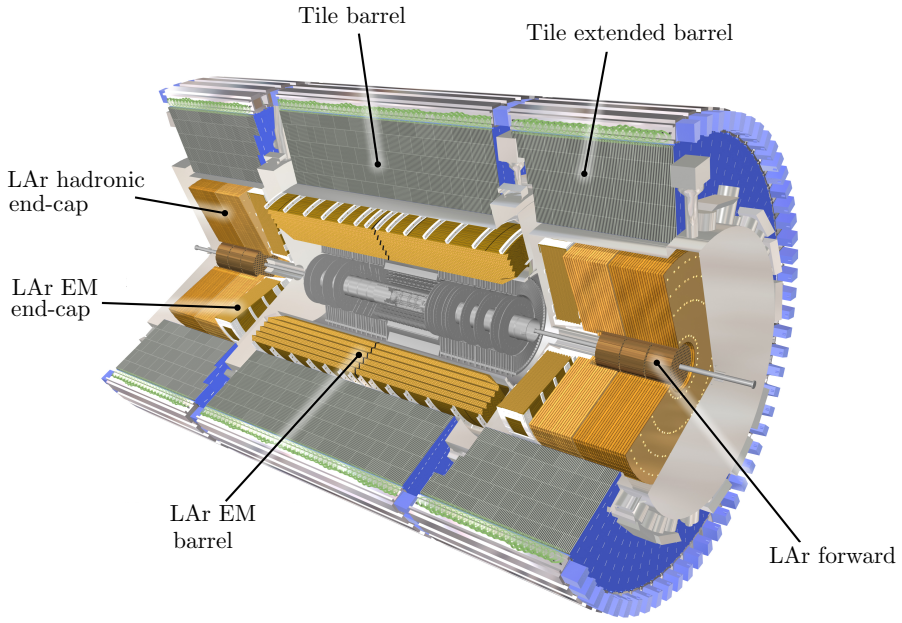

FIGURE 2.2: The TileCal of the ATLAS detector [CERN©].

The TileCal has a coverage of $|\eta|< 1.7$ and is comprised of a central long barrel (LB) and two retractable extended barrels (EB) on either side. These cylindrical barrels are made up of 64 modules each with coverage $\phi = 0.1$ and consists of 4 mm steel plates sandwiching 3 mm thick plastic scintillators. These scintillating tiles are made from polystyrene (PS) and the tiles are orientated perpendicular to the axis beam.

After a collision, resultant energetic hadrons traverse the detector and interact with steel plates. This interaction which further results in a shower of energy within calorimeter. More detail regarding the particle-matter interaction is discussed in more detail in Section 3.2. In

this instance, however, the energy after the particle's energetic interaction with the steel plates is absorbed by the scintillating plastics and re-emitted as fluorescent light. The fluorescent nature of the scintillating material is discussed in Section 3.3. Figure 2.3 depicts the regular integrated read-out module with its various components.

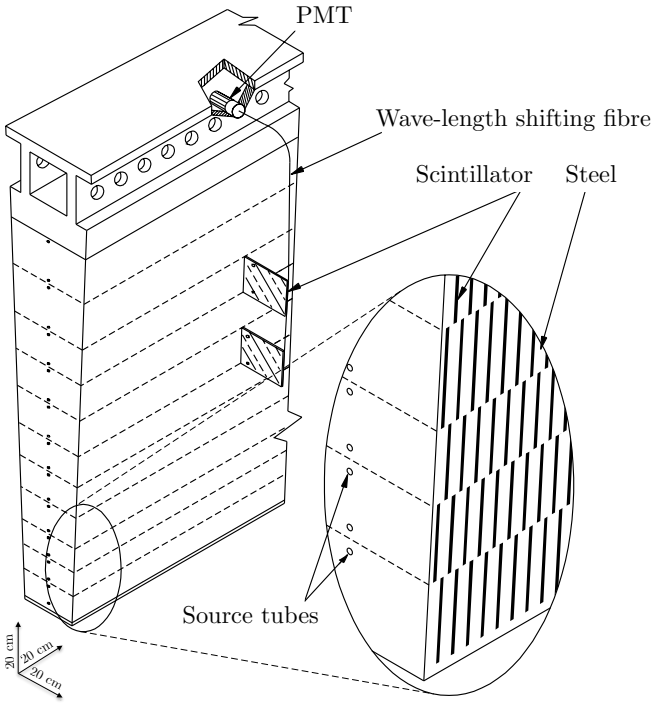

FIGURE 2.3: Regular integrated read-out module including various components in the TileCal. Adapted from [17].

Wave-length shifting optical fibre bundles, which couple to each side of grouped scintillating tiles known as read-out cells, collect and guide the produced light to photomultiplier tubes (PMTs). The incoming light from read-out cells is converted to an electrical signal by the PMTs (see Section 3.5.1). This electrical signal is digitised and used to reconstruct properties pertaining to the particle [17].

TileCal modules are segmented into three longitudinal layers: A, BC, and D; this segmentation in η and depth of the TileCal modules is illustrated in Figure 2.4. The upper left shaded area is the central barrel and the upper right shaded area is the extended barrel of the TileCal, respectively. Additional gap scintillator modules are situated below the Intermediate Tile Calorimeter (ITC) region at $1.0 < |\eta| < 1.2$. The ITC cover the region $0.8 < \eta < 1.0$ and is situated in the extended barrel in both D4 and C10 modules as depicted in

Figure 2.4. Furthermore, cryostat scintillator modules are situated in the LAr EM End-cap calorimeters [21] at $1.2 < |\eta| < 1.6$. Gap and crack scintillators are therefore situated in the E1 and E2, and E3 and E4 modules, respectively.

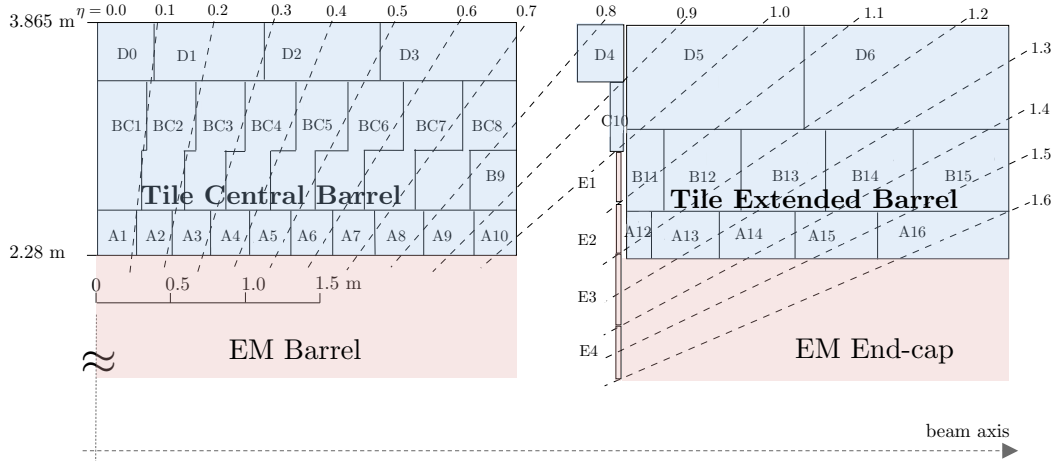

FIGURE 2.4: A segmentation of the TileCal modules displaying ITC scintillator positions relative to the readout cells.

These scintillators have independent read-outs and provide signal which is used to correct for energy losses in the transition (gap) region between the Tile EB and EM Barrel and End-cap. This energy loss is associated to the gap region being filled with auxiliary infrastructure including services, cables, and power supplies [17].

2.1.2 Minimum Bias Trigger

The parton model of Quantum Chromodynamics (QCD) [5] excellently describes *hard* interactions coming from incoming particles with large p_{T}. These predictions agree well with data from high energy proton-proton (pp) collisions at the LHC [22]. Minimum bias events provide insight into *soft* interactions in the low-energy regime for non-perturbative QCD.

In order to select such events, three triggers [23] are employed: randomly selected bunch crossings, randomly selected bunch crossings together with SCT space point trigger, and the minimum bias trigger scintillators (MBTS). The minimum bias trigger is experimentally defined as a trigger used to accept inelastic events which have a minimum energy threshold or geometrical acceptance [24].

The dimensions of MBTS are depicted in Figure 2.5. They are constructed from 2 cm thick PS plastic scintillators and are situated on the inner surface of the LAr End-cap cryostats. In total, there are 16 counters which cover a range of $2.1 < |\eta| < 3.8$. Half the counters form the inner ring and the other half form the outer ring [13].

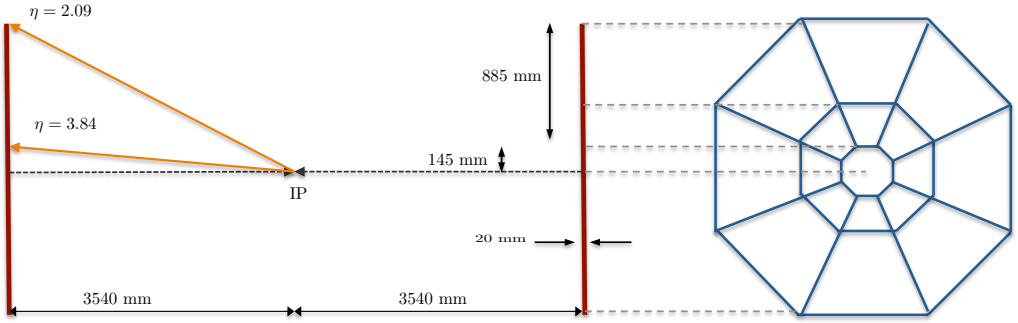

FIGURE 2.5: Dimensions of the MBTS and its distance from the IP. Adapted from [25].

2.1.3 Radiation Environment in the ATLAS Detector

Collisions at the IP are the primary source for background radiation in the LHC [17]. The deleterious effects this radiation has on the components and performance of the ATLAS detector was important to understand prior to the Run I data-taking-phase of the LHC. In order to optimise shielding in ATLAS, the particle fluence and absorbed dose was simulated. The GCALOR [26] simulation package, which simulates large scale high energy physics (HEP) experiments, was mainly used when calculating the optimum shielding that ATLAS required. In addition to this, FLUKA [27] simulated the hadronic and EM cascades produced by extremely energetic particles.

Figure 2.6 depicts GCALOR simulations for the ionising dose closest to the IP for the TileCal region per year. These simulations assume a centre-of-mass energy[1] $\sqrt{s} = 14$ TeV, and a nominal luminosity[2] of 10^{34} cm^{-2}s^{-1}. The locations of the various sub-detectors and calorimeters are shown, as well as a contour scale to the right indicating the integrated dose per year. The MBTS detector region is indicated by the white rectangular shape to the right of the TRT. These calculations estimate that the TileCal readout system is exposed to less than 30 Gy per year [17].

[1] A Lorentz-invariant energy describing the total energy arising from the collision of two energetic particles.
[2] The number of events per unit time for a given interaction cross-section.

Prior radiation damage studies conducted [28] on the TileCal region at an integrated luminosity equivalent to 10 years running nominal luminosity expect that a total dose deposited in the plastic scintillators situated at an $\eta = 0$ and $\eta = 1.5$ be 264 Gy and 381 Gy, respectively, for charged and neutral particles.

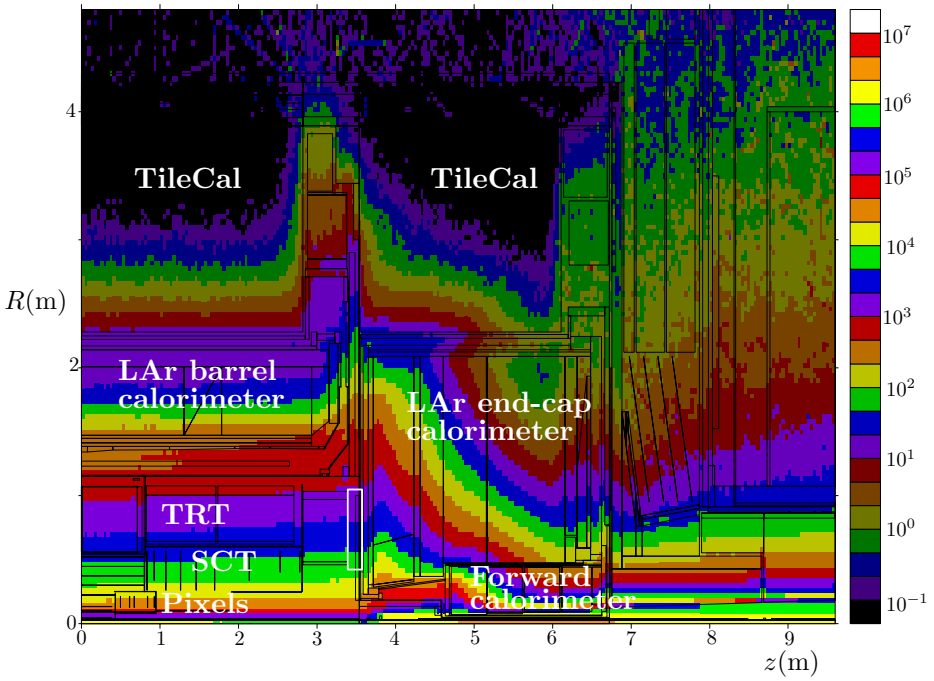

FIGURE 2.6: Simulated radiation contour map of the total ionising dose in the TileCal region over one year at $\sqrt{s} = 14$ TeV and a nominal luminosity of 10^{34} cm^{-2}s^{-1}. Adapted from [17].

After the Run I data taking phase of the LHC (2009 - 2012), which operated at $\sqrt{s} = 7$ TeV, the estimated absorbed dose revived by MBTS was between 0.1×10^4 and 0.4×10^4 Gy [29]. Further measurements conducted at $\sqrt{s} = 13$ TeV suggest that the MBTS be replaced and that these serve as thermal neutron shields for the calorimeter [25].

Chapter 3

Overview of Scintillators and Radiation Damage

In this chapter the concept of energy loss along the passage of a charged particle in matter is introduced. This results in radiation damage and defect creation within the material. The absorbed radiation dose due to this charged particle-matter interaction is subsequently calculated. Focus is then placed on scintillators and their luminescent properties, their importance in particle detection, and the effects of radiation damage on their luminescence based particle detection ability.

3.1 Introduction

Particle detection relies on the interactions between particles and matter which is dependent on the properties of both the particle and material. Scintillation detectors can be organic or inorganic in nature and are defined as materials that, when excited by high-energy particles, emit a fluorescent pulse of light [30]. The light produced acts as a signature of the interaction. Scintillation detectors play an integral part in many fields where there is a need to detect energetic particles. Radiation damage caused by the interaction of energetic particles with plastic scintillators is widely studied [2]. However, this damage is not well understood due to its complexity [31] and, presently, radiation-hard plastics are being developed and optimised for their desired properties [32].

3.2 Interaction of Charged Particles with Matter

A particle passing through a material experiences interactions depending on its own physical properties such as charge and magnetic moment [33]. These properties determine the type of interactions with the fields present within the material such as the electromagnetic (EM) and strong nuclear fields. In the case of charged particles, such as electrons, protons, and alpha particles, EM and nuclear interactions result in elastic and inelastic scattering, electronic excitations and ionisations, and nuclear reactions [34]. These interactions take place with certain probabilities (cross-sections) [35] and ultimately result in the incoming, traversing particle losing energy. This energy loss, in many respects, characterises the interaction and constitutes a measure for energy transfer to the atomic structure of the material. It carries information which ultimately can be used for the detection and description of the incoming particle. The total energy loss can be regarded as the sum of *electronic energy loss* (through inelastic collisions with atomic electrons) and so called *nuclear energy loss* (elastic collisions with the atomic nuclei).

Figure 3.1 represents a classical depiction of the undisturbed trajectory of a charged particle moving in the vicinity of an atom with atomic radius a. As long as the impact parameter b is much larger than a, that is $b \gg a$, inelastic scattering through Coulombic electronic interactions occur. Here, the Coulomb field is dominant and results in electronic excitations. A fraction of the particle's transferred energy is absorbed by the material, and emitted as

Cherenkov radiation if the particle in the material moves faster than the speed of light in that material.

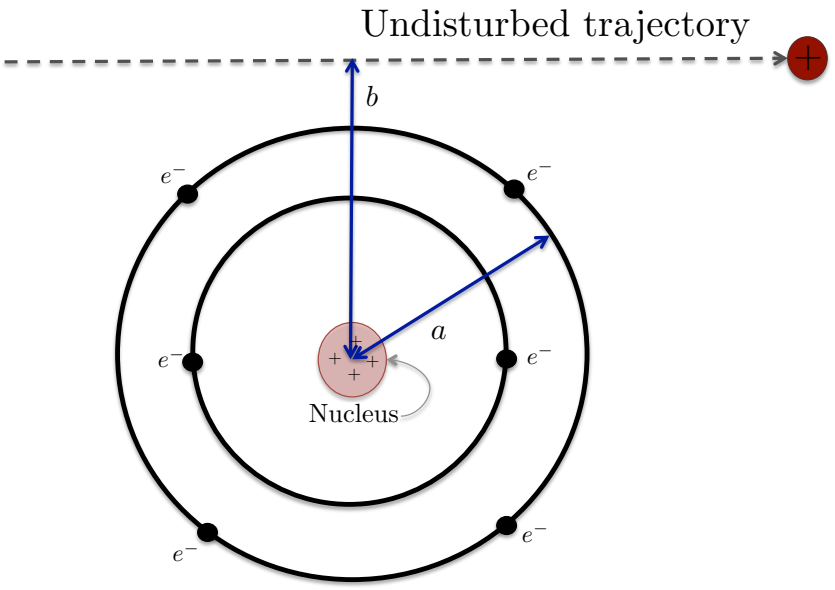

FIGURE 3.1: A classical depiction of an undistributed trajectory of a charged particle where a is the atomic radius and b is the impact parameter. Adapted from [34].

However, when the trajectory of the particle is closer to the atom such that b is comparable to a, inelastic collisions are more likely to occur between the particle and individual atomic electrons. These inelastic collisions, due to the Coulombic field between the incoming particle and the electrons of the atoms in the molecule of the material, result in electronic excitations and ionisations with characteristic cross-sections. In some cases, the transferred energy is sufficiently high such that the ejected electron itself causes a notable secondary ionisation. These electrons are referred to as δ-rays. The two above mentioned cases for inelastic electronic collisions account for the electronic energy loss by the particle and a deviation from its initial trajectory.

Elastic collisions with nuclei, resulting in nuclear energy loss, are less frequent than inelastic electronic collisions. This process occurs when $b \ll a$ in Figure 3.1. A Coulomb interaction occurs between the particle and atomic nucleus. Although small, the energy loss is sufficient, however, to overcome the so-called displacement energy for individual atoms of the material (which is of the order of a few tens of eV). The displacement energy is the minimum amount of kinetic energy required to displace an atom from its position in a material [36].

The displacement of atoms results in many defects in the material, such as vacancies and interstitials. In particular, the vacancies that form are significant in characterising the radiation damage [37] induced along the path of the incoming particle. For incoming particles with energies above the Coulomb barrier, as defined by the nuclei of the material, nuclear reactions also occur.

3.2.1 Stopping Power

The average energy lost per unit length $-dE/dx$ (often referred to as the stopping power) is a function of momentum. The stopping power of a material can be described using the Bethe-Bloch equation [38] for moderately relativistic charged particles and is given by

$$-\frac{dE}{dx} = \frac{Kz^2Z}{A\beta^2}\left[\frac{1}{2}\ln\left(\frac{2m_ec^2\beta^2\gamma^2E_{\max}}{I^2}\right) - \beta^2 - \frac{1}{2}\delta(\beta\gamma) - \frac{C}{Z}\right]. \tag{3.1}$$

Table 3.1 displays the variables on the right hand side of Equation 3.1. Correction terms $\delta(\beta\gamma)$, the density correction, and C, the shell correction, are added to the equation and become significant for both low and high energy cases.

Variable	Meaning	Value
K	-	$4\pi N_A r_0^2 m_e c^2$
z	Charge of incident particle	-
m_e	Rest mass of electron	-
r_0	Classical Bohr radius	e^2/m_ec^2
Z	Atomic number of material	-
N_A	Avagadro's number	-
c	Speed of light	-
A	Relative atomic mass	-
β	Velocity of incident particle	v/c
γ	Lorentz factor	$1/\sqrt{1-\beta^2}$
I	Average excitation energy	-
$\delta(\beta\gamma)$	Density dependent correction to energy loss	-
$E_{\max}$	Maximum kinetic energy transferred to an electron	-
C	Shell correction	-

TABLE 3.1: Variable meanings and values in the Bethe-Bloch Equation.

In all cases, the energy loss decreases as the incident particle's energy increases. However, Equation 3.1 only holds if the incident particles velocity is much larger than that of the atomic electrons. If the incident velocity is smaller, the energy loss increases with an increase in incident particle energy, and reaches a maximum when the two energies are comparable. Finally, the Bethe-Bloch equation applies to materials made up of pure elements.

The average stopping power for materials that are either mixtures or compounds is better approximated [33] using Bragg's rule [39]. This approach uses a linear combination of each individual elements stopping power weighted by the amount percentage of electrons belonging to that element. Its accuracy is limited as electronic energy loss depends on the nature of the material. The stopping power for mixtures or compounds is given by the following

$$\frac{1}{\rho}\left(\frac{dE}{dx}\right) = \sum_{1}^{i} \frac{w_i}{\rho_i}\left(\frac{dE}{dx}\right)_i \qquad i = 1, 2, 3, \cdots, \tag{3.2}$$

where w_i and ρ_i is the fraction of weights and densities of elements, respectively. Bragg's rule is inaccurate when there are bond changes [40] within a mixed or compound material. These changes alter the charged state of the ion within the material which subsequently alter the particle-matter interaction. Bond changes are taken into consideration by the Core and Bond (CAB) approach [41]. These bond corrections are applied to the chemical bonds associated for each stopping power to each linear combination in Equation 3.2. The corrected stopping power is a superposition of atomic cores which simply follows Bragg's rule added to the stopping due to bonds between electrons [42] given by

$$-\left(\frac{dE}{dx}(z)\right) = (\alpha z)^2 \left[\sum \text{cores} + \sum \text{bonds}\right], \tag{3.3}$$

where α is the fractional effective charge of the incident particle, z. The effect of these corrections can be seen in Figure 3.2.

Figure 3.2 shows the correlation between experimental data and Bragg's rule stopping estimate for polystyrene, and the CAB approach, respectively. The CAB approach takes the bonding effects between hydrogen and carbon and the single and double bonds between carbon atoms into consideration. A stronger correlation is seen between the experimental data [43–46] with the CAB approach than the simplified Bragg's rule. This is for the interaction between hydrogen ions H and polystyrene with a chemical composition $(C_8H_8)_n$. This particular compound and ion interaction is chosen as it is important to the current study.

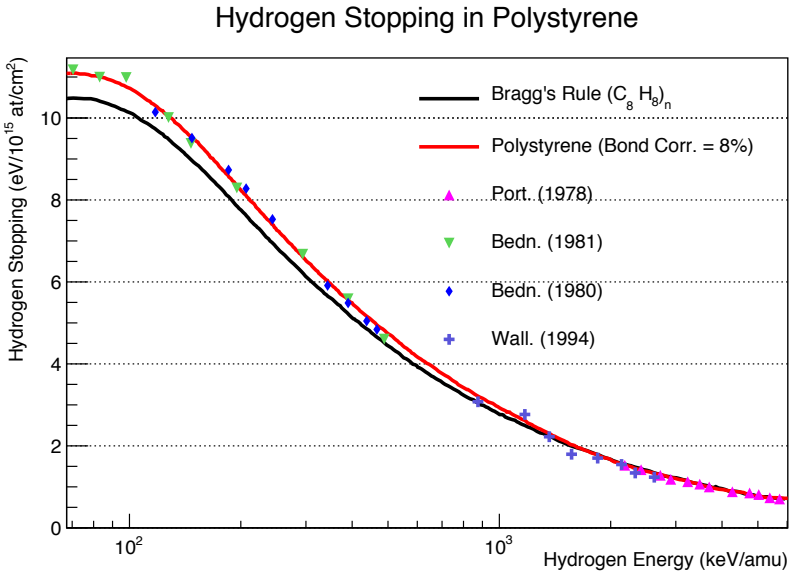

FIGURE 3.2: Stopping of H ions in polystyrene, adapted from [47].

An arbitrary trajectory is taken by the traversing particle. It continuously slows down in the material through electronic and nuclear interactions [48]. Assuming energy loss is constant, the particle comes to a complete stop at projected range, R_p. This projected range is a projection of the average pathlength, R_t. For an ion with initial energy E_0 and direction this is calculated for a particle using

$$R_t(E_0) = \int_0^{E_0} dE \, \frac{1}{dE/dx}. \tag{3.4}$$

The integral limits indicate that a particle will disperse all its initial energy into the material. The total energy loss results in a dose absorbed by the material [34].

3.3 Luminescence in Organic Molecules

The transferred energy of an incident particle is absorbed by the material and results in excitations of the atomic electrons. The subsequent photon emission from the de-excitation of these electrons is referred to as luminescence [1]. Luminescence is characterised by the fact that the emitted photon energy from the excited material is smaller than that of the absorbed

energy. This phenomenon is divided into two sub-processes: fluorescence and phosphorescence which are related to the singlet and triplet states of the electrons, respectively.

Fluorescence is defined as the spontaneous emission of light from transitioning electrons from a singlet excited orbital state to a singlet orbital ground-state [49]. This pair of electrons differ in spin orientation. Phosphorescence is defined as the emission of light from a transitioning electron in a triplet excited orbital state to a singlet ground-state. This pair of electrons have the same spin orientation and, as a consequence, the decay for phosphorescence is usually longer [50] than that of fluorescence.

In organic molecules the number of emitted photons is described by an exponential equation of the form

$$N(t) = N_0 \, e^{(-t/\tau)}, \tag{3.5}$$

where N is the number of emitted photons after time t, N_0 is the number of created photons, and τ is the decay time due to fluorescence. Simultaneously activated energy states give rise to complex absorption and emission spectra. These states include electronic, vibrational, and rotational energies. The π-electron[1] structure in organic molecules gives rise to its luminescent properties. In the case of electronic excitations, singlet states, S_n, correspond to all electrons in the molecule having a paired spin. Triplet states, T_n corresponds to a set of unpaired electrons [51]. The probability of occupying either a singlet or triplet state depends on the orbital energies of the valence electrons and the electrostatic exchange strengths between electrons of parallel spin in the ground state [52]. A transition between these states can be induced by the absorption of an energy of a particular frequency [53]. This process is further investigated in Chapter 4 when the triplet state of an organic molecule is revisited.

Figure 3.3 depicts electronic excitations and de-excitations in an excited organic molecule with π-electron structure. Fluorescent light is emitted when there is a transition from the S_{10} state to one of the lower lying electronic s states, S_{0m}. There is a small overlap between the optical absorption and emission spectra (referred to as the *Stokes shift*) where the excitation energy is greater than the de-excitation energy. This is shown by the downward pointing arrows from state S_{10}. There is a Stoke shift except for the $S_{10} \rightarrow S_{00}$ case (not shown in diagram). The transition from these states undergoes internal conversion, where no photons are emitted, and the molecular spins remain in the singlet state. This is then followed by vibrational relaxation where the electron loses energy to other molecules through collisions [51]. This

[1] A π-electron refers to the electrons resides in a π bond. These are formed in double or triple bonds or conjugated p orbitals that overlap.

process is similar in the inter-system crossing de-excitation, where no photons are emitted but the molecule is now exist in the triplet state. Again, this is followed by vibrational relaxation and this de-excitation yields phosphorescent light. The characteristic delayed phosphorescent light is due to that fact that the life-time of the T_{10} triplet state is longer than that of the first singlet state. Delayed fluorescence may also be observed when a thermally excited electron in T_{10} is promoted to S_{10} and de-excites to S_{0m}.

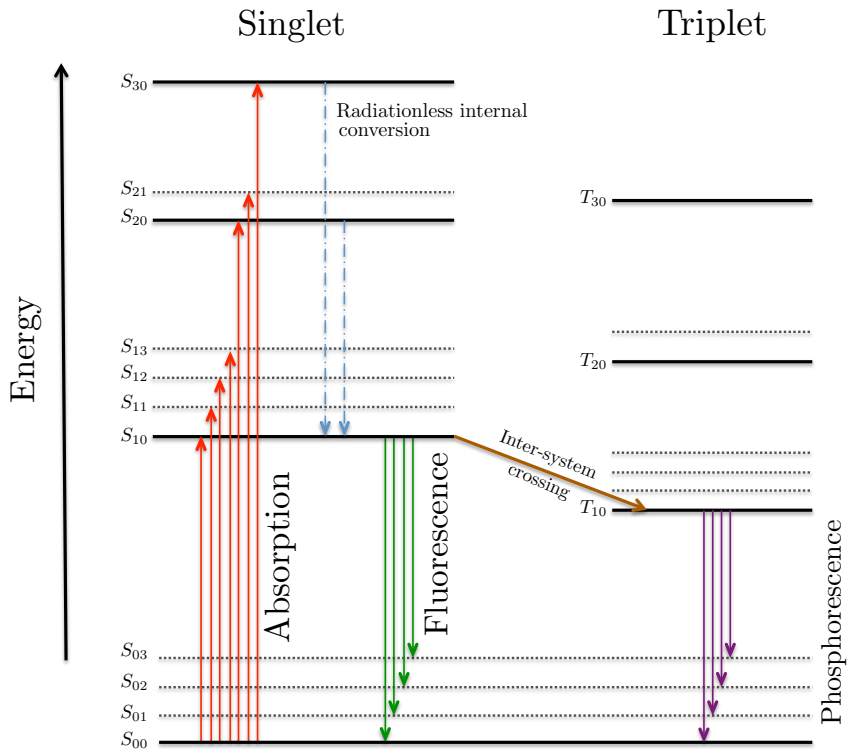

FIGURE 3.3: Jablonski energy level diagram for an organic molecule with π-electrons.

However, a secondary photon can be absorbed which promotes the electron to a higher singlet state. This process is depicted by the upward pointing lines from S_{00} and occurs if the excitation light is in resonance with the absorption into higher states. Non-radiative de-excitations, such as the vibrational relaxations, can be grouped into one general process called "quenching". Quenching decreases the number of fluorescent photons as, in some cases, it causes an inter-system crossing from S_{10} to T_{10}. The ability to convert an incident particle's energy to fluorescent light is a desired property of organic molecules. The fluorescent efficiency of an organic molecule associated with this property is defined as the fraction

of absorbed energy converted to fluorescent light. Therefore, it is desirable for quenching mechanisms in organic molecules to be reduced.

3.4 Plastic Scintillators

Plastic scintillators are fluorescent organic hydrocarbon compounds that consist of linked benzene-ring derivatives. These compounds are used as an aromatic polymer base [30]. Figure 3.4 depicts a circular π-bond of a benzene ring where electron densities in the aromatic p-orbitals interact and become delocalized below and above the plane of the ring. Furthermore, molecular orbital (MO) theory predicts that atomic orbitals (AOs) which overlap constructively form a bonding MO. Alternatively, destructive interference results in an anti-bond MO causing a dissociation of the atoms [54]. Since there are six AOs in benzene, there are also associated six MOs: three bonding (π) and three anti-bonding (π^*) and therefore there are three aromatic transitions $\pi \rightarrow \pi^*$. These transitions have bands associated to them and for benzene these absorption bands occur at 180 nm, 200 nm, and 256 nm, respectively, which corresponds to the UV-visible range [55].

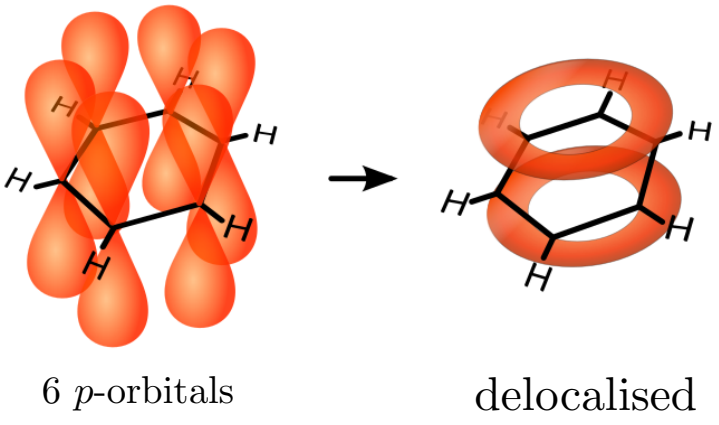

FIGURE 3.4: Representation of MO bonding in a benzene molecule.

Thus, the aromatic nature of these benzene derivatives, and therefore scintillators, allow for fluorescence in the excited material. The most commonly used benzene derivatives used as plastic bases are polyvinyl toluene (PVT) and polystyrene (PS). The monomers of PS and PVT are displayed in Figure 3.5. The styrene monomer, seen on the left of Figure 3.5, is a benzene derivative with a terminal double bond functional group. It is also referred to

as ethenylbenzene. It has no additional isomers and has the chemical formula C_8H_8. The vinyl toluene monomer, see on the right in Figure 3.5, also has a terminal double bond functional group and an additional methyl group. It has three isomers, namely 1-ethenyl-2-methylbenzene, 1-ethenyl-3-methylbenzene, and 1-ethenyl-4-methylbenzene. These all have a chemical formula C_9H_{10}.

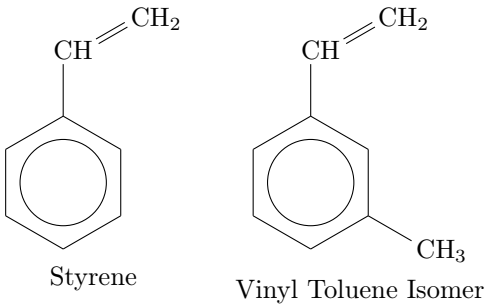

FIGURE 3.5: Monomers of PS and PVT used as bases in plastic scintillators.

On their own, the plastics have a very low light yield but by adding a small percentage (between 0.3% and 4%) of a particular aromatic compound the light yield increases. These aromatic compounds, referred to as fluors, are also fluorescent in nature and are dissolved into the plastics. Fluors act as wavelength shifters as they absorb short wavelengths emitted by the plastic base and re-emit at longer wavelengths [56]. Two fluors are usually dissolved into a plastic. These are referred to as the primary and secondary fluors.

The de-exciting plastic base transfers non-radiative energy to the primary fluor through a long range dipole-dipole coupling mechanism which is referred to as the Förster resonance energy transfer (FRET) [57]. The primary fluor also decreases the decay of the scintillator since the average distance between fluor and base is less than the wavelength of light released. Secondary fluors are also added to improve the scintillation characteristics. They absorb excited energy from the primary fluor and re-emit a photon with a longer wavelength around 400 nm [58]. The main advantage of adding primary and secondary fluors is that a larger fraction of fluorescent scintillation occurs which can be coupled to a PMT better at 420 nm [59].

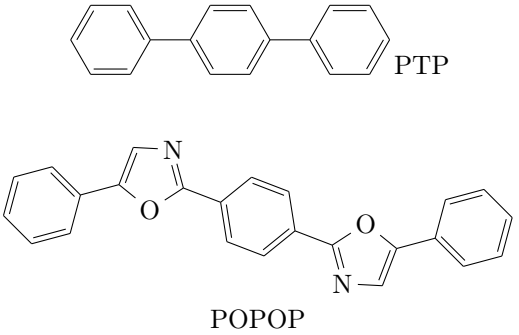

FIGURE 3.6: Common primary (PTP) and secondary (POPOP) fluors added to plastic scintillators to aid scintillation.

The most common primary fluors used are p-Terphenyl (PTP) as a primary fluor and diphenyloxazolyl-benzene (POPOP) as the second secondary fluor. Together, these can increase a plastic's scintillation efficiency by 40% if concentrations of 4% and 0.002% are added respectively [60]. Figure 3.6 above depicts the molecular representations for the aromatic primary and secondary fluors PTP and POPOP, respectively.

3.4.1 Scintillator Manufacturing Process

Three main manufacturing methods exist for the production of plastic scintillators. Batch cell casting involves heating up liquid monomers with their fluors in a mould. Once cooled, a solid plastic is formed which can be shaped and polished into a desired shape. The second technique is the injection moulding technique and is most commonly used in mass production [59]. Here, granulated plastics and their dopants are placed into a heated screw cylinder. The mixture is melted, mixed and squeezed out a nozzle where it can be shaped. Finally, the third technique, called the extrusion technique, is similar to the injection technique in that granulated plastics and their dopants are heated in a moulding machine. This mixture is pushed through a dye in order to obtain a particular profile.

3.5 Applications of Scintillators

In general, scintillators and scintillation detectors have a wide variety of applications in scientific and industrial fields [61]. Analytical applications for scintillation counters include

measuring the radioactivity through the detection of radioactive tracers. These traces become concentrated in human tissue after having been intravenously administered. In the medical field, scintillators form part of various tomographic scanners and detect these radioactive substances in patients in order to provide reconstructed internal images of their body.

The use of plastic scintillators has been outlined specifically for the ATLAS experiment in Section 2.1. In general, in high energy physics (HEP) experiments, scintillators are used to determine whether the track formed by a charged particle should be reconstructed or not. In electromagnetic and hadronic calorimeter measurements, plastic scintillators surrounded by materials that possess a large atomic number to measure particle energy changes. Finally, time-of-flight measurements can be made done with plastic scintillators.

3.5.1 Scintillation Detectors

The luminescent nature of scintillators when struck by energetic particles is a desired feature in scintillation detectors. Scintillating materials are optically coupled directly to photodetectors or via wavelength shifting fibres to form a scintillation detector. Common photodetectors are PMTs which are tubes kept under vacuum that can measure a range of photon energies [62]. These energies are converted into electrical pulses which are analysed.

Figure 3.7 depicts a PMT that is sensitive to the wavelength emitted by the scintillator and consists of an anode, a photocathode, and series of dynodes coated in an alkaline substance that emit electrons when struck by photons. These photoelectrons are accelerated and focused onto the first in a series of a dynodes by an electrode. Once at the dynode, the electrons undergo secondary emission and are multiplied; this process is repeated until the last dynode is reached and electrons are "collected" at the anode. A current is produced from these electrons proportional to the light emitted from the scintillator. This current is amplified and can be analysed as an electrical signal via the connector pins.

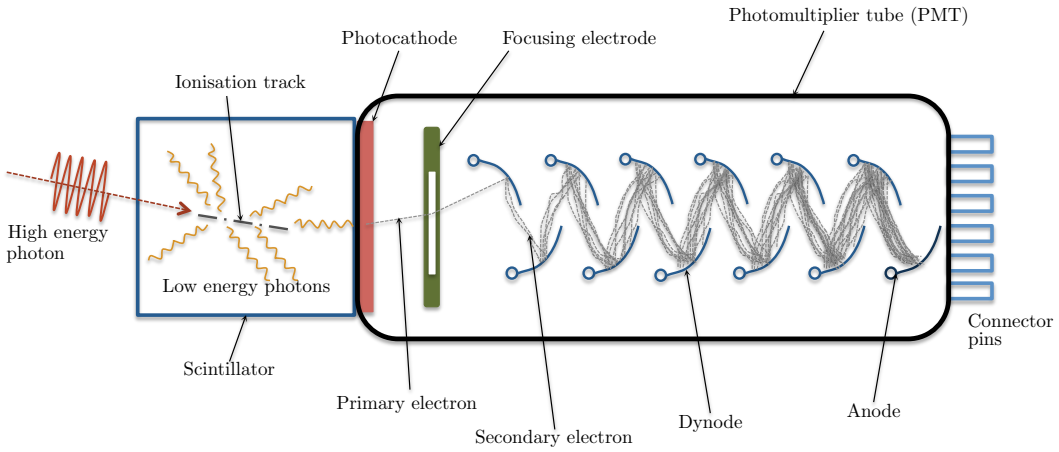

FIGURE 3.7: Schematic of a photomultiplier tube connected to a scintillator.

The resultant amplitude of the electrical pulse yielded by a scintillation detector is proportional to the excitation energy of the scintillator [33]. Therefore, energy can be measured reliably by the scintillator detector and it is used as an energy spectrometer. Scintillator detectors exhibit great precision in determining time differences between events and have fast recovery times. These characteristics allow them to accept high count rates. Finally, scintillator detectors distinguish between different particles by discriminating between the characteristic pulse shape created as a result of the particle interacting with the scintillating material.

3.6 Effects of Radiation Damage in Plastic Scintillators

Many factors play a role when considering the effects of radiation damage in plastics scintillators. The type of particle interaction with the plastics has been briefly considered in the previous sections. However, factors including the total absorbed dose, the dose rate, the composition and concentration of the added fluors, post-irradiation environment, and the time taken for plastics to recover after irradiation, all contribute to the type of damage seen in plastics. These factors and their emergent features in the bulk material are considered in this section.

In general, radiation damage to plastics results in the formation of tracks and excited species (which include hydrogen atoms, unpaired electrons, and low molecular weight macro-radicals). These excited species form when bonds break within the polymer. They initiate chemical

reactions [14] that alter the structure of the polymer backbone[2] of the plastic. This ultimately degrades the mechanical and chemical properties of the plastic. The chemical changes to the polymer result in the following processes: the evolution of various gases, the formation of double and triple bonds (referred to as unsaturation), degradation of the backbone, and cross-linking between polymers in the plastic [63].

3.6.1 Gas Evolution and Free Radical Formation

Gas evolution, in general, results from bonds breaking in long chained molecules through their interaction with ionising radiation. This process is referred to as main chain scission and results in the formation of either ion pairs, or free radicals and unpaired electrons depending on the type of bond broken. Hydrogen is the most common gas that is formed from irradiated plastics that do not contain oxygen [14].

In both PVT and PS, the removal of a hydrogen atom (dehydrogenation), occurs primarily between C − H [64, 65]. This, subsequently, results in the formation of free radicals. In PS, the two most common free radicals that form are a benzyl and cyclohexadienyl-type radicals [65] depicted in Figure 3.8 (a) and (b), respectively. The benzyl radical is formed as a result of dehydrogenation from the styrene monomer leaving a carbon atom with an unpaired electron. The cyclohexadienyl-type radical is formed by the addition of a hydrogen to the styrene monomer resulting in the formation of hydrogen gas.

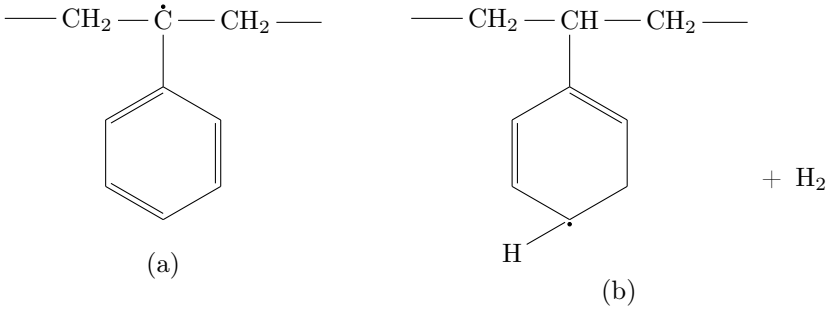

FIGURE 3.8: Benzyl radical (a) and cyclohexadienyl-type radical (b) that form in irradiated PS. Adapted from [65].

Gas evolution also occurs in irradiated PVT [64]. These include hydrogen gas, C_2H_2, and C_3H_5 [66]. In both PVT and PS, the yield of total gas increases with an increased absorbed

[2]Continuous linear chain of covalently bonded atoms leading to the simplest representation of a molecule.

dose [67]. Finally, the formation of alkyl radicals or fraction or alkyl-like radicals have been observed in irradiated plastics due to dehydrogenation [68]. These include, but are not limited to, the following: $-CH^{\bullet}-$, $-CH_2^{\bullet}-$, and $-CH_3^{\bullet}-$, $-CH^{\bullet}CH_3$, and $-C^{\bullet}(CH_3)-$.

3.6.2 Cross-linking and Unsaturation

Cross-linking refers to covalent bonds that form between two polymer chains [69]. The free radicals, induced by the ionising radiation, combine to produce these cross-links which, with increasing radiation damage, result in the formation of a three dimensional network [70]. A discolouration emerges as a results of the formation of the network [15] and continues with an increase in dose. This increase also leads to unsaturation and, ultimately, an increase in yield of carbon-carbon bonds, namely $C=C$ and $C\equiv C$ [71]. This is primary due to dehydrogenation of $C-H$ bonds. Furthermore, the degradation of the polymer by unsaturation forms of new electronic transitions [72, 73] and absorption bands [74] referred to as "colour centres".

Both radiation induced cross-linking and unsaturation degrade the backbone of the polymer. This degradation has unwanted implications on the plastic's optical and mechanical properties.

3.6.3 Effects on Optical Properties

Radiation damage decreases the transmittance of light, the luminescence intensity, and the pulse height at relatively high doses [75]. Above a minimum absorbed dose [76] these profiles are altered by the presence of radiation induced radicals. These radicals act as quenchers and decrease the transmittance, shifting it to higher wavelengths. There is little to no change in position of the luminescence curve with an increases dose. However, the decrease in emitted light is confirmed by a decrease in the pulse height [15].

Doping the plastic also has an effect on the transmittance and emission intensity [75]: undoped plastics show a smaller resistance to radiation damage than doped plastics. Thus, the addition of primary and secondary fluors to plastic scintillators retards the decrease in transmission and emission intensity [77] (below a certain dose) indicating that these added fluors are less susceptible to radiation damage than the base.

3.6.4 Exposure to Oxygen and Recovery

During irradiation, the diffusion of oxygen into the polymer results in the formation of peroxide radicals and other oxygen containing products. The stable products and radicals act as quenching agents [78] that reduce fluorescent light. Figure 3.9 depicts the interaction with styrene and oxygen.

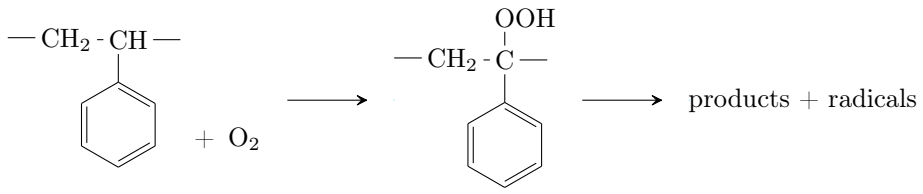

FIGURE 3.9: Diffusion of oxygen into styrene forming an unstable peroxy intermediate which further forms stable products and radicals. Adapted from [65].

The oxygen diffuses into the styrene forming peroxy intermediate which further form excited radicals and stable products. The amount of oxygen that diffuses into the plastic is dose rate dependent. The process shown in Figure 3.9 also occurs post-irradiation, but is temperature dependent [79]. The excited radicals have a varying lifetime depending on the environment plastics are kept in post-irradiation and can be observed for up to several weeks [15]. In an oxygen containing environment (air), the interaction between the radicals and oxygen results in the formation of C = O and C − H groups [80].

Finally, plastic scintillators recover after some time depending on the dose they absorbed and conditions under which they are kept. The recovery process is accelerated by the presence of heat (annealing) and oxygen. A fraction of the absorption properties recover when irradiated to low doses [81] and later come into contact with oxygen.

Chapter 4

Electron Paramagnetic Resonance: Theory and Applications

In this chapter the magnetic interaction between a material and an externally applied magnetic field is discussed in a classical and semi-classical manner. A quantum mechanical approach is taken to discuss the complete magnetic interaction between a material and magnetic field when discussing principles underlying electron paramagnetic resonance, and the interpretation of the resultant spectroscopic signal features receive attention. Finally, a quantitative computational model is introduced which could prove vital in understanding the experimental results.

4.1 Magnetic Moment and Angular Momentum

A handful of analogous systems exist which explain the concept of the magnetic moment. The classical description of a loop current, depicted in Figure 4.1, is one such example whereby a current I, resulting from an accelerated charge, circulates in an infinitesimal loop of area dA.

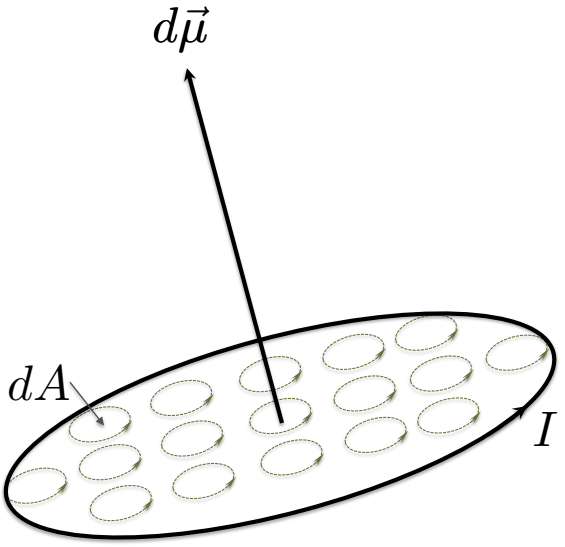

FIGURE 4.1: An infinitesimal magnetic moment, $d\vec{\mu}$, due to a current loop.

In the presence of a magnetic field, a resulting infinitesimal magnetic quantity emerges as a result of a torque on the current loop. For loop of finite size, having an area A, the sense in which an infinitesimal current loop circulates cancels with its neighbouring loops, leaving only the contribution from the total perimeter of the loop. The magnetic moment, $\vec{\mu}$, is then the summation of all infinitesimal contributions from $d\vec{\mu}$ and is to the current multiples the total area, that is,

$$\vec{\mu} = \int d\vec{\mu} = I \int dA = IA \quad \text{J T}^{-1}, \tag{4.1}$$

which has units joules (J) per tesla (T). The use of the unit tesla is justified in Section 4.1.2, where the magnetic field units are discussed. Magnetic moments in solids are associated with the angular momenta of the electrons. There are two such momenta that the electrons posses: 1) the orbital angular momentum and 2) the intrinsic angular momentum. The magnetic moment is related to the angular momentum via a proportionality factor, γ, known as the gyromagnetic ratio, that is

$$\vec{\mu} = \gamma \vec{J}. \tag{4.2}$$

The magnetic moment points in the same direction as $\vec{J}$, the total angular momentum vector (whether it is orbital or intrinsic). In general the gyromagnetic ratio is given by

$$\gamma = g\frac{q}{2m}, \tag{4.3}$$

where q and m are the charge and mass of the circulating particle, respectively, and g is the g-factor.

4.1.1 Spin Magnetic Moment

In the case of an isolated electron, the magnitude of $\vec{\mu}$ is calculated by considering the electron's intrinsic angular momentum (spin) and its magnetic moment. In the presence of a uniform, external magnetic field in the z-direction, the spin angular momentum, with quantum number $S = 1/2$, takes one of two different spin orientations. Along the direction of the magnetic field, the magnetic moment is given as

$$\mu_z = -\frac{e}{2m_e}m_s\hbar, \qquad m_s = \pm 1/2 \tag{4.4}$$

where m_e is the mass of the electron and m_s is the quantised spin angular momentum number. The magnetic moment of the electron is a physical constant caused by its spin angular momentum, referred to as the Bohr magneton [82], is defined then as follows

$$|\vec{\mu}| = \mu_B \equiv \frac{|e|\hbar}{2m_e} = 9.27400949(80) \times 10^{-24} \quad \text{J T}^{-1}. \tag{4.5}$$

For a free electron the magnetic dipole moment of the electron is $1.00161\mu_B$. This is an important result and is used in Section 6.3 to give an indication of the number of unpaired electrons there are in a given system.

4.1.2 Magnetic Field Quantities and Units

EPR is applied to materials containing a large ensemble of electrons and radicals; thus, when discussing the magnetisation of a material, one is concerned with its bulk magnetisation, $\vec{M}$. This is defined as the moment per unit volume and is related to the applied magnetic field by a dimensionless proportionality factor known as the bulk magnetic susceptibility, χ. The susceptibility measures the extent to which a material can be magnetised in the presence of

an external magnetic field. Therefore, the magnetisation is expressed as

$$\overrightarrow{M} = \frac{\chi}{\mu_0}\overrightarrow{B}, \tag{4.6}$$

where μ_0 is the permeability of a vacuum. Generally, χ is defined in terms of the $\overrightarrow{H}$ (the external magnetic "field"). However, the field that an electron experiences, $\overrightarrow{B}$ (the magnetic flux density), is related to $\overrightarrow{H}$ via $\overrightarrow{B} = \mu_0(\overrightarrow{H} + \overrightarrow{M})$. It should be noted firstly that $\overrightarrow{B}$ refers to the total magnetic field externally applied, whereas $\overrightarrow{H}$ includes contributions from sufficiently close particles [83], and secondly that the dimensions of these vector field quantifies differ; in particular the units of $\overrightarrow{B}$ are tesla (T = kg $s^{-1}C^{-1}$ = 1 × 10^4 Gauss). This justifies the dimensions of the magnetic moment (Equation 4.1). The measure of the magnetic field intensities are expressed in Gauss (G) throughout this dissertation.

4.1.3 Paramagnetism

A paramagnet has a $\chi > 0$ implying that the magnetisation is in the same direction as the magnetic field (Equation 4.5). More specifically, the magnetic moments in the material are magnetised by their interaction with the applied magnetic field, and lose this magnetisation when the field is no longer applied; the randomly reorientating magnetic moments result in the materials demagnetising.

As previously outlined, the magnetic moments of a material are intrinsically linked to the spin of the electrons in a material. More precisely, the spin of an atomic or a molecular orbital containing exactly one electron in them (an unpaired electron) causes this magnetisation when it lifts the degeneracy of the spin angular momentum [84]. Additional paramagnetic contributions arise from the material's protons and other radicals. Their contributions are several orders of magnitude smaller than those of the unpaired electrons' but provide information about the local magnetic environment of the material.

4.2 Electron Paramagnetic Resonance

Electron paramagnetic resonance spectroscopy is a technique concerned with the magnetic behaviour of large ensembles of paramagnetic species and their interaction with an externally applied magnetic field and EM radiation [83]. Resonance occurs when EM radiation, in the

microwave range, is applied to a system containing paramagnets, and this matches the energy level spacing of the microwave photons [85]. The electron's paramagnetic contribution to the total magnetic susceptibility can be studied using the resonance method in a detailed and precise manner.

4.2.1 Resonance Theory

The magnetic moment in the presence of an externally applied magnetic field, in its vector representation, has a potential energy $U = -\vec{\mu}^T \cdot \vec{B}$[1]. Therefore, a simple Hamiltonian describes this energy interaction of a single electron and is given by

$$\hat{\mathcal{H}} = -\vec{\mu}_e^T \cdot \vec{B} \tag{4.7}$$

where $\vec{\mu}_e$ is the electron's spin magnetic moment where the negative sign arises due to the electron's negative charge. The externally applied magnetic field then defines the z-direction, and the energy (now denoted by E) of the electron in the magnetic field is

$$E = g_e \mu_B m_s B_0, \tag{4.8}$$

where B is the magnitude of the magnetic field and g_e is the g-factor for the free electron. The electron g-factor is one of the most accurately measured constants in physics [86] with a value of

$$g_e = 2.0023193043617(15). \tag{4.9}$$

Since there is a restriction placed on the value of m_s (Equation 4.4), the electron can exist in either the lower energy state (denoted by $|\beta\rangle$) or a higher state (denoted by $|\alpha\rangle$). The differences in the energies associated to the two so-called electronic *Zeeman energies* is easily calculated by applying the spin condition for the two spin states to Equation 4.8.

[1] The T superscript represents the transpose of the matrix.

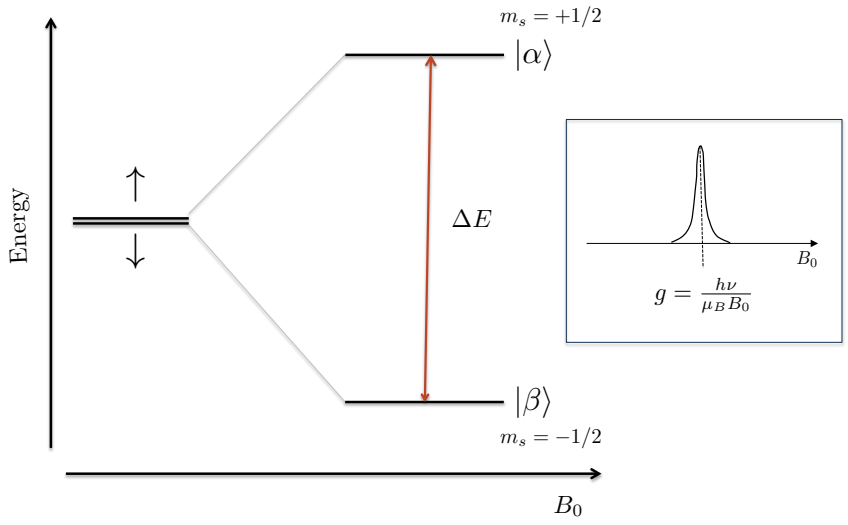

FIGURE 4.2: Electron spin levels in a magnetic field for a spin 1/2 system.

In the absence of an externally applied magnetic field, the two energy states are said to be degenerate as they have the same energies. The application of the magnetic field lifts these energy degeneracies of the spin states. A transition between these states may be induced with the application of an electromagnetic field with a resonant frequency, ν, which has a photon energy matching ΔE. That is,

$$\Delta E = h\nu = g\mu_B B_0. \tag{4.10}$$

Equation 4.10 is known as the *resonance condition* and is valid for systems with $S = 1/2$ as depicted in Figure 4.2. Experimentally, the transition between the two spin states results in an absorption peak shown on the right in Figure 4.2. The omission of the subscript e on the g-factor is due to the fact that the magnetic field experienced at each spin species is an effective one. This will be discussed in more detail in Section 4.2.3.

4.2.2 Spin Relaxation and Resonance Line Shape

The absorption of the resonant radiation is only detected if there is a difference in population between the two spin levels [52]. The resonance spectrum, as shown in Figure 4.2, cannot be a sharp δ-distribution but rather acquires a Gaussian or Lorentzian shape, and is referred to as the line shape. The broadening of this peak is related to the interaction of the spins

which is rigorously derived from the Bloch equations [87]. These equations describe the bulk magnetisation of magnetic moments in the presence of a static or oscillating magnetic field as a function of time. This sophisticated description will not be discussed in any detail in this study, as accurate measurements for the relaxation parameters could not be measured due to the limitations of the available spectroscopy techniques. Instead, a qualitative discussion is provided which concerns the interaction between the spin and its atomic surroundings at thermal equilibrium.

In a static magnetic field, for a system containing N electrons, the population of spins in the lower state (N_β) is slightly larger than those in the upper state (N_α). The ratio between the number of spins in these states follows the Maxwell-Boltzmann distribution

$$\frac{N_\alpha}{N_\beta} = \exp\left(-\frac{\Delta E}{k_B T}\right) = \exp\left(-\frac{g\mu_B B_0}{k_B T}\right), \tag{4.11}$$

where k_B is the Boltzmann factor and T is the absolute temperature. Thus, there is a change in spin populations which results from a net energy absorption and a resonant absorption line.

The application of an oscillating magnetic field results in an exponential decay (in time) in the difference in spin population levels which eventually equalises. This equalisation is known as *saturation* and eventually results in the disappearance of the resonance absorption line shape. A vital criterion for the application of the magnetic field is that there be an interaction between the spins and surrounding system (generally referred to as the lattice which includes degrees of freedom not associated to spin). The transfer of energy from the magnetic field causes a reorientation of the spins and any excess of energy is transferred to other degrees of freedom. This process of non-radiative transitions between the two states $|\alpha\rangle$ and $|\beta\rangle$ is referred to as the spin-lattice relaxation, and the time taken for energy to be transferred to the other degrees of freedom is called the spin-lattice relaxation time, denoted by τ_1.

However, there is a second relaxation mechanism that is associated with the *unsaturated* line shape involving the interaction between spins via a magnetic dipole coupling. The relaxation mechanism, referred to as spin-spin relaxation, characterises the effect that the relative energies of the spin levels, not the lifetimes, can fluctuate due to the interaction between spins. The interaction between spins causes a change in spin orientation and therefore, the spin-spin relaxation time, τ_2, reflects the energy of interaction between the spins.

This investigation does not concern the precise measurements of τ_1 and τ_2 but rather the effects on the linewidth of the EPR spectra. In order to obtain accurate values for τ_1, the so-called power saturation technique is employed and for τ_2, a pulsed EPR technique is utilised. In this study, however, continuous wave (CW) EPR is employed whereby the continuous irradiation of a material placed in a magnetic field to detect absorption spectrum (see Section 5.5). The characteristic EPR spectrum is the derivative of the absorption line shape.

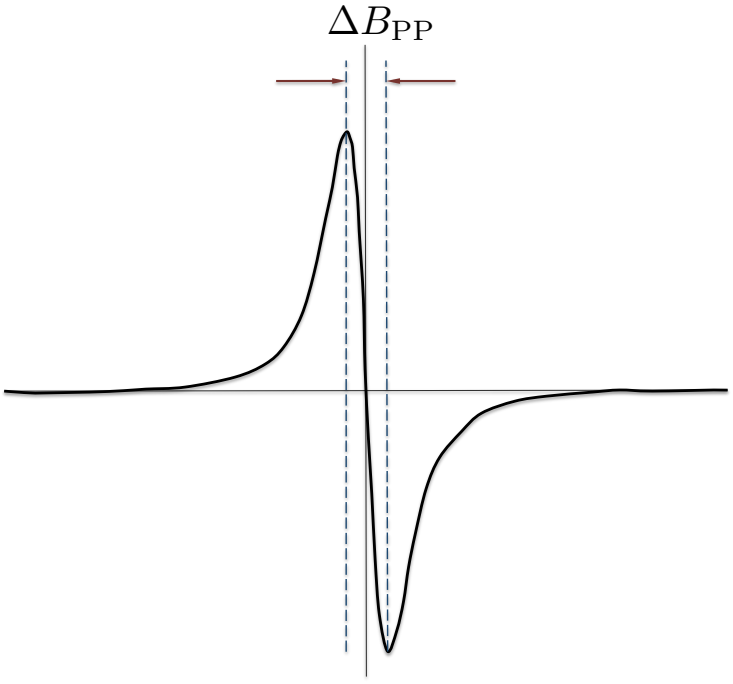

FIGURE 4.3: First derivative of a Lorentzian line indicating the peak-to-peak width.

Both spin-spin and spin-lattice relaxation times contribute to the broadening of the linewidth. The peak-to-peak width of the EPR spectrum (ΔB_{PP}), as shown in Figure 4.3, is proportional $1/\tau_2$ [88] in CW EPR (and also $1/\tau_1$ is other cases) when the magnetic field is varied (swept) and the electromagnetic frequency is kept constant in order to satisfy the resonant condition.

4.2.3 Chemical Shifts and the Effective g-factor

As mentioned at the end of Section 4.2.1, there is an effective magnetic field that is experienced by the spin species in a material which magnetises it. This is given by

$$\vec{B}_{\text{eff}} = \vec{B}_{\text{ext}} + \vec{B}_{\text{local}} \tag{4.12a}$$

$$\vec{B}_{\text{eff}} = (1 - \sigma)\vec{B}_{\text{ext}}, \tag{4.12b}$$

where in Equation 4.12a this field consists of the induced magnetic field and many local magnetic fields that are independent of it. These additional local fields arise from the magnetic effects of induced electronic currents. The subscript ext of $\vec{B}$ is left out of the notation from this point onwards for simplicity. Equation 4.12b captures the total effective field effects on the magnetic moments and includes a screening constant σ which is of the order of 10^{-6} [83]. The screening constant is analogous to the so-called "chemical shift" parameter σ_n in nuclear magnetic resonance (NMR). This magnetic screening alters the interaction in Equation 4.7 giving rise to the effective g-factor (and magnetic moment) [52].

Variations to the effective g-factor occur as a result of spin-orbit (SO) coupling which provides electrons with a small amount of orbital angular momentum and ultimately changes the electron's magnetic moment. The observed deviation in the g-factor

$$\Delta g = g - g_e \tag{4.13}$$

describes the difference between the effective g-factor and that of the free electron. There are a range of g-factors that a material can exhibit [83] and Δg can be either positive or negative in sign which increases or decreases g, respectively. The distinct g-factors provide a reasonable identification for paramagnetic species. Section 3.6 outlined the effects of radiation damage on plastic scintillators, and the possible radicals that form. Studying the g-factors of damaged plastics could identify the radicals that form and indicate the magnetic, environmental changes within plastics. Ultimately, signatures of these radicals should appear in the EPR spectra, this is discussed in more detail in Section 4.5.

4.3 The Spin Hamiltonian

Until now the description of EPR has either been classical, or semi-classical. A purely quantum mechanical argument is required to describe the magnetic interactions of spin with its environment. The spin Hamiltonian is a static Hamiltonian that contains the interactions between paramagnetic species with an electron spin S with the externally applied magnetic field and other magnetic moments (nuclei with spin I) in the vicinity of the electron spin. In the ground state, the terms in the Hamiltonian are

$$\begin{aligned}\hat{\mathcal{H}}_0 = &\sum_i \left[\hat{\mathcal{H}}_{\mathrm{EZ}}(i) + \hat{\mathcal{H}}_{\mathrm{ZF}}(i)\right] + \sum_i \sum_k \hat{\mathcal{H}}_{\mathrm{HF}}(i,k) \\ &+ \sum_k \left[\hat{\mathcal{H}}_{\mathrm{NZ}}(k) + \hat{\mathcal{H}}_{\mathrm{NQ}}(k)\right] + \sum_i \sum_{j>i} \hat{\mathcal{H}}_{\mathrm{EE}}(i,j),\end{aligned} \tag{4.14}$$

where indices i, j, and k represent the set of electron spins, the set of neighbouring electron spins, and the set of nuclei, respectively. Equation 4.14 is ordered in terms of the descending energetic contribution. The spin Hamiltonian consists of the following terms:

$\hat{\mathcal{H}}_{\mathbf{EZ}}(i)$**:** The Electron-Zeeman interaction term has already been introduced is Equation 4.7 and describes the interaction between an electron's spin and the externally applied magnetic field. This is the most dominant term in the spin Hamiltonian.

$\hat{\mathcal{H}}_{\mathbf{ZF}}(i)$**:** The Zero-Field interaction is relevant for systems with $S > 1/2$ and describes the dipole-dipole interaction between electrons.

$\hat{\mathcal{H}}_{\mathbf{HF}}(i,k)$**:** The hyperfine interaction describes the interaction between electron and nuclear spin.

$\hat{\mathcal{H}}_{\mathbf{NZ}}(k)$**:** The Nuclear-Zeeman interaction is analogous to the Electron-Zeeman interaction and it describes the interaction between the nuclear spin and the externally applied magnetic field.

$\hat{\mathcal{H}}_{\mathbf{NQ}}(k)$**:** The Nuclear Quadrupole interaction is relevant for systems with nuclear spin $I \geq 1$ that give rise to a nuclear electrical quadrupole moment that interacts with local electric field gradient at the nucleus.

$\hat{\mathcal{H}}_{\mathbf{EE}}(i,j)$**:** The Electron-Electron interaction describes dipole-dipole the coupling between two electron spins.

Although EPR spectroscopy is concerned with the complete spin Hamiltonian, only the Electron-Zeeman, Zero-Field, and hyperfine interactions are relevant to the systems under investigation. This approximate spin Hamiltonian is justified in Sections 4.4 and 4.6.2. The most general expression for the spin Hamiltonian involves the use of tensors which incorporate all possible spatial directions of molecules under investigation.

4.3.1 The Electron-Zeeman Interaction

In the most general description, the interaction between an electron's spin and the external magnetic field is

$$\hat{\mathcal{H}}_{\mathrm{EZ}} = \mu_B \vec{B}^T \cdot \mathbf{g} \cdot \hat{\vec{S}} = \mu_B \begin{pmatrix} B_x & B_y & B_z \end{pmatrix} \cdot \begin{pmatrix} \mathrm{g}_{xx} & \mathrm{g}_{xy} & \mathrm{g}_{xz} \\ \mathrm{g}_{yx} & \mathrm{g}_{yy} & \mathrm{g}_{yz} \\ \mathrm{g}_{zx} & \mathrm{g}_{zy} & \mathrm{g}_{zz} \end{pmatrix} \cdot \begin{pmatrix} \hat{S}_x \\ \hat{S}_y \\ \hat{S}_z \end{pmatrix}, \tag{4.15}$$

where $\vec{B}$ and $\hat{\vec{S}}$ are expressed in terms of their scalar components defined in terms of x, y, and z and $\mathbf{g}$ is known as the $\mathbf{g}$-tensor. Previously, this required the inclusion of a scalar - the g-factor. This is due to the spherical symmetry of the isolated electron discussed in Section 4.1.1. Therefore, its associated spin Hamiltonian (Equation 4.7) has an isotropic, rank[2]-0 (scalar) $\mathbf{g}$-tensor.

The $\mathbf{g}$-tensor elements are determined by a sample's orientation within the magnetic field. In most cases the tensor is symmetric and can be diagonalised via an Euler angle transformation which leads to the the diagonalised $\mathbf{g}$-tensor

$$\mathbf{g}_{\mathrm{diag}} = \begin{pmatrix} \mathrm{g}_{xx} & 0 & 0 \\ 0 & \mathrm{g}_{yy} & 0 \\ 0 & 0 & \mathrm{g}_{zz} \end{pmatrix}, \tag{4.16}$$

which contains the tensor's *principal components* g_{xx}, g_{yy}, and g_{zz}. It should be mentioned that in a liquid solution, the paramagnetic samples can tumble rapidly and randomly. Experimentally, the effective g-factor can be measured which, in the case of a solution, is equal to the averaged trace of the diagonalised $\mathbf{g}$-tensor, that is $\frac{1}{3}(\mathrm{g}_{xx} + \mathrm{g}_{yy} + \mathrm{g}_{zz})$. As is in the case Section 4.2.3, the SO coupling causes these principal components to deviate from the

[2]The rank of a tensor is its total number of indices (either contravariant or covariant). In the case of the $\mathbf{g}$-tensor, there are two contravariant indices i and j such that g can be written as g_{ij}. Thus, the rank of the $\mathbf{g}$-tensor is 2.

g_e values but it also creates an orientation dependence. A quantum mechanical derivation for the deviation in the principal components is done [52] by considering the the total magnetic moment operator which contains contributions from the spin and orbital angular momenta. However, this deviation is neatly expressed in tensor form as

$$\Delta\mathbf{g} = \mathbf{g} - \mathbf{g}_e, \tag{4.17}$$

where $\mathbf{g}_e = g_e\mathbb{1}$, with $\mathbb{1}$ being the identity matrix.

At first glance the differences between Equations 4.13 and 4.17 only seem to come from the formulation of the Electron-Zeeman interaction and indeed, for the isotropic case of the isolated electron, these two equations are equivalent. However, anisotropic systems, such as solids, require the use of $\mathbf{g}_e$ to completely describe the deviation in EPR signatures from that of the free electron's. In spite of this, Equation 4.13 will not be neglected as it is determined experimentally. In fact, the effective g-factor will be calculated directly from the EPR spectra in Section 6.2. Equation 4.17 is used in Section 6.3.2 related to the computational determination of the EPR spectra.

4.3.1.1 Anisotropy of the g-tensor

Within disordered samples, such as polymers, the interaction between the external magnetic field and detected radicals are randomly distributed. This is an anisotropic interaction which arises due to the rotational motion and results in an EPR *powder spectrum*. The absolute orientation of a sample in the magnetic field is described using two angles θ, the elevation angle, and φ, the azimuthal angle.

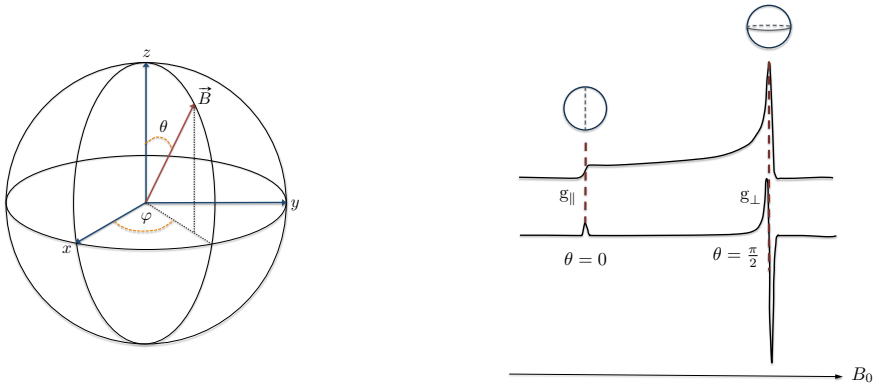

(a) (b)

FIGURE 4.4: (a) Sample coordinate system and the magnetic field vector $\vec{B}$ in a unit sphere defining the elevation angle θ and the azimuthal angle θ and (b) the absorption and derivative EPR line shape for a randomly orientated sample with axial symmetry. The unit spheres above the spectra illustrate the orientational contributions from the principal components. Adapted from [88]

Figure 4.4a depicts the sample orientation in the magnetic field in a unit sphere where θ is the angle between the z-axis and the magnetic field vector $\vec{B}$ and φ is the angle between the magnetic field vector's projection onto the xy-plane and the x-axis. The effective g-factor depends on both angles and in the case where there is axial symmetry, the g_{zz} principal component aligns parallel to the sample frame and both g_{xx} and g_{yy} align perpendicular to it. This is expressed as $g_{zz} = g_\perp$ and $g_{xx} = g_{yy} = g_\parallel$. The effective g-factor value now only has a θ dependence given by

$$g(\theta) = \sqrt{g_\perp^2 \sin^2\theta + g_\parallel^2 \cos^2\theta}. \tag{4.18}$$

The resulting EPR signal and its integrated absorption spectrum are depicted in Figure 4.4b. The unit spheres placed above both spectra illustrate orientational contributions from the principal components and the angles below them illustrate the positions along the signal to which these components contribute. The anisotropic broadening of the powder spectrum results in a characteristic "tail" that forms to one side of the absorption peak.

4.3.2 The Zero-Field Interaction

The Zero-Field interaction describes the dipole-dipole coupling between individual unpaired electron spins for systems that have a total spin $S > 1/2$ and which display no cubic symmetry. In the absence of a magnetic field, the energy splitting expressed by

$$\hat{\mathcal{H}}_{\mathrm{ZF}} = h\hat{\vec{S}}^{T} \cdot \mathbf{D} \cdot \hat{\vec{S}} = h \begin{pmatrix} \hat{S}_x & \hat{S}_y & \hat{S}_z \end{pmatrix} \cdot \begin{pmatrix} \mathrm{D}_{xx} & \mathrm{D}_{xy} & \mathrm{D}_{xz} \\ \mathrm{D}_{yx} & \mathrm{D}_{yy} & \mathrm{D}_{yz} \\ \mathrm{D}_{zx} & \mathrm{D}_{zy} & \mathrm{D}_{zz} \end{pmatrix} \cdot \begin{pmatrix} \hat{S}_x \\ \hat{S}_y \\ \hat{S}_z \end{pmatrix}, \tag{4.19}$$

where $\mathbf{D}$, the zero-field tensor, is symmetric and the sum of its principal components is zero (traceless). The traceless, diagonalised zero-field tensor allows Equation 4.19 to be rewritten in terms of two constants which are defined in terms of the zero-field tensor's principal components such that

$$\hat{\mathcal{H}}_{\mathrm{ZF}} = D(\hat{S}_z^2 - \frac{1}{3}\hat{S}^2) + F(\hat{S}_x^2 - \hat{S}_y^2), \tag{4.20}$$

where $D = (3/2)\mathrm{D}_{zz}$ and $F = 1/2(\mathrm{D}_{xx} - \mathrm{D}_{yy})$. The values of D and F are not unique as they depend on the choice of axes. In Section 4.4 the triplet state in organic molecules is investigated and is a result of the degeneracy removal by the $\hat{\mathcal{H}}_{\mathrm{ZF}}$ interaction.

4.3.3 The Hyperfine Interaction

The most general interpretation describing the interaction between the electrons and nuclear spins is

$$\hat{\mathcal{H}}_{\mathrm{HF}} = h\hat{\vec{S}}^{T} \cdot \mathbf{A} \cdot \hat{\vec{I}} = h \begin{pmatrix} \hat{S}_x & \hat{S}_y & \hat{S}_z \end{pmatrix} \cdot \begin{pmatrix} \mathrm{A}_{xx} & \mathrm{A}_{xy} & \mathrm{A}_{xz} \\ \mathrm{A}_{yx} & \mathrm{A}_{yy} & \mathrm{A}_{yz} \\ \mathrm{A}_{zx} & \mathrm{A}_{zy} & \mathrm{A}_{zz} \end{pmatrix} \cdot \begin{pmatrix} \hat{I}_x \\ \hat{I}_y \\ \hat{I}_z \end{pmatrix}, \tag{4.21}$$

where $\mathbf{A}$, the hyperfine tensor, is generally symmetric and therefore can be transformed into its diagonal form, $\mathbf{A}_{\mathrm{diag}}$. The diagonal tensor may be further decomposed into the sum of two terms

$$a_{\mathrm{iso}}\hat{\vec{S}}^{T} \cdot \hat{\vec{I}} + \hat{\vec{S}}^{T} \cdot \mathbf{T} \cdot \hat{\vec{I}} \tag{4.22}$$

an isotropic contact term and a dipole coupling term. The a_{iso} factor is the isotropic hyperfine coupling constant and proportional to the square of the electronic wavefunction's amplitude at the nucleus.

In general, the interaction energy between the two magnetic moments $\vec{\mu}_e$ and $\vec{\mu}_n$ of the electron and nuclei, respectively, is

$$E = \frac{\mu_0}{4\pi}\left[\frac{\vec{\mu}_e^T \cdot \vec{\mu}_n}{r^3} - \frac{3(\vec{\mu}_e^T \cdot \vec{r})(\vec{\mu}_n^T \cdot \vec{r})}{r^5}\right], \tag{4.23}$$

where $\vec{r}$ is the radius vector from $\vec{\mu}_e$ to $\vec{\mu}_n$ and $r = |\vec{r}|$ is the distance between the them. Thus, the second term in Equation 4.22 introduces the anisotropic hyperfine tensor $\mathbf{T}$ which, ignoring anisotropies of the $\mathbf{g}$-tensor, can be diagonalised via a transformation.

4.4 Organic Molecules in the Triplet State

The triplet state in organic molecules has already been introduced in the discussion on luminescence in organic molecules (see Section 3.3). The quantum mechanical description of the triplet state of a molecule is that its spin is $S = 1$; it therefore has three possible energy eigenvalues: 0 or ± 1. These molecules contain two unpaired electrons that couple to each other via a magnetic dipole-dipole interaction which removes the energy degeneracies and results in an anisotropic EPR spectra.

Many organic molecules display a triplet state illustrated by their integrated EPR spectra [65]. In particular, PS and similar organic molecules display the characteristic triplet state EPR powder spectrum [89, 90]. Describing these spectral features requires that the spin Hamiltonian, for the most part, include the Electron-Zeeman and Zero-Field interactions

$$\hat{\mathcal{H}} = \hat{\mathcal{H}}_{\mathrm{EZ}} + \hat{\mathcal{H}}_{\mathrm{ZF}} \tag{4.24}$$

for two unpaired electrons. The symmetric triplet state functions for the electron pairs with subscripts 1 and 2, respectively, in the higher or lower state ($|\alpha\rangle$ and $|\beta\rangle$) is written as

$$\begin{aligned} |T_{+1}\rangle &= |\alpha_1\alpha_2\rangle\,, \\ |T_0\rangle &= \frac{1}{\sqrt{2}}\,|\alpha_1\beta_2 + \beta_1\alpha_2\rangle\,, \\ |T_{-1}\rangle &= |\beta_1\beta_2\rangle\,. \end{aligned} \tag{4.25}$$

Figure 4.5 depicts the allowed transitions in the triplet state when the magnetic field is in the z-direction. The solid lines indicate transitions for $\Delta m_s = \pm 1$ and the dashed line

indicates the "forbidden" transition for $\Delta m_s = 2$. In lower magnetic fields, the selection rules break down since S_z is no longer a good quantum number. This gives rise to the forbidden transition when the applied frequency is *parallel* to the magnetic field in the z-direction.

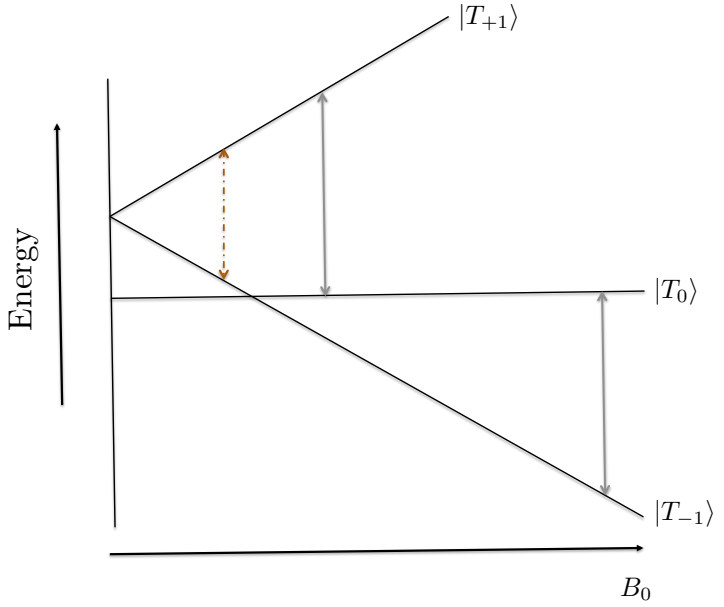

FIGURE 4.5: Triplet energy levels in an organic molecule where the solid lines indicate the $\Delta m_s = \pm 1$ transitions and the dashed line indicates the "forbidden" $\Delta m_s = 2$ transition.

These three transitions result in three absorption peaks. It is expected that in aromatic molecules such as PVT and PS, there would be two electrons likely to occupy degenerate π orbitals in a triplet state. Therefore, the EPR spectrum that could arise for these molecules is that of a π-electron in a triplet state.

4.5 EPR Signal Changes in Irradiated Plastics

Irradiated plastics display notable changes to their EPR signals when compared to un-irradiated ones. Four general features are discussed which arise in these signals and are similar whether the plastic is irradiated with γ-rays, negatively [91] or positively charged particles [92].

EPR linewidth broadening is observed to increase as the dose increases [67]. The peak-to-peak-width, ΔB_{pp} provides an indication of the linewidth broadening as a function

of dose. This can be related to the changes to the polymer base induced by radiation damage.

Shoulder formation has been noted in irradiated PS EPR spectra and is speculatively associated to hyperfine interactions between unpaired electrons and protons in the sample [93]. These peaks can be identified [94] and related to the possible radicals that form during irradiation (see Section 3.6.1).

Absorbed EPR signal intensities and concentration of formed radicals increase [68] or decrease [95] with dose depending on factors such as the dose rate, type of particle interaction, and environmental conditions both during and after irradiation. This implies structural changes to the plastics on a molecular level and that bonds are broken.

Spectral (*g*-factor) shifts have been observed as a function of dose and at low temperatures [96] and related to the absorption signal intensity. This implies that there is a variation in the local magnetic fields experienced by the detected radicals.

4.6 Density Functional Theory

Density functional theory (DFT) is the most successful quantum mechanical approach used to understand the electronic structure in a many-body system [97]. Schrödinger's equation predicts the behaviour of a single electron as well as a large ensemble of electrons and nuclei by describing the electrostatic interactions between the particles

$$\hat{\mathcal{H}}\Psi = E\Psi \tag{4.26}$$

with the use of the Hamiltonian $\hat{\mathcal{H}}$. This complex interaction can be simplified with the use of the Born-Oppenheimer approximation [98] which separates the electronic and nuclear degrees of freedom. This simplification, however, is only useful when attempting to understand a trial system.

The self-consistent Kohn-Sham formalism of DFT [99] employs the notion of a ground state electronic particle density, $n_0(\vec{r})$, which determines the ground state energy of the system through a functional, $E_0[n_0(\vec{r})]$ [100]. This formalism transforms the interacting system into a non-interacting one by defining a set of non-interacting, one-electron orbitals, $\phi_i(\vec{r})$, such

that

$$n_0(\vec{r}) = \sum_{\text{occ}} |\phi_i(\vec{r})|^2, \tag{4.27}$$

which is a summation of the occupied orbitals. Equation 4.26 is then mapped onto a set of N single-particle wavefunction equations

$$-\frac{\hbar}{2m_e}\nabla^2\phi_i(\vec{r}) + \left[V_{\text{ion}}(\vec{r}) + \int d\vec{r}^{\,\prime}\,\frac{n_0(\vec{r}^{\,\prime})}{|\vec{r}-\vec{r}^{\,\prime}|} + V_{\text{xc}}[n_0(\vec{r})]\right]\phi_i(\vec{r}) = \varepsilon_i\phi_i, \tag{4.28}$$

where the first term represent the kinetic energy, the second is the mean-field Coulombic electron-electron repulsion (Hartree interaction), and V_{xc} is the so-called exchange-correlation (XC) interaction between the electrons. Computationally, the first two terms are uncomplicated to calculate; however, the V_{xc} potential is unknown and calculating it requires that approximations be made in order to make progress [101]. The local density approximation (LDA) is one such approximation in which the XC energy at any given point in space is the same as that of an homogeneous electron gas with the same local density. Furthermore, adding in functionals which depend on the gradient density improves the results of many solid-state calculations.

A realistic crystalline system consists of a large number of electrons; by exploiting the translational symmetry of the system, the Kohn-Sham orbitals are expanded using Bloch's Theorem under boundary conditions. The lattice periodicity of the potential described in square brackets in Equation 4.28 requires that the eigenstates of the single particle Hamiltonian take the form

$$\Psi_{n,\vec{k}}(\vec{r}) = e^{i\vec{k}\cdot\vec{r}}u_{n,\vec{k}}(\vec{r}). \tag{4.29}$$

The periodic function $u_{n,\vec{k}}(\vec{r}) = u_{n,\vec{k}}(\vec{r}+\vec{R})$ for all real space lattice vectors, $\vec{R}$, and $\vec{k}$ is the crystal momentum in reciprocal space where unique values for it reside within the first Brillouin Zone (BZ). Solving for a larger number of electrons implies integrating over all crystal momentum vector points or $\vec{k}$-points. However, the Monkhorst-Pack algorithm [102] approximates this solution by visualising the reciprocal space as an equidistant grid of $\vec{k}$-points where the integral only runs over the first BZ.

For aperiodic systems (such as systems containing defects, impurities, and disorder) which do not obey translational symmetry, the *supercell* approximation is utilised within boundary conditions. This approximation isolates the region of interest, such as a defect region, and periodically repeats this "cell" many times so the interaction between neighbouring cells is

minimised. In periodic, defect region studies, eliminating interactions between neighbouring cells requires that the supercells are impossibly large.

Equation 4.28 is mathematically simplified with the choice of a plane-wave basis. The Kohn-Sham eigenstates are now expressed in terms of a reciprocal lattice vector $\vec{G}$, such that

$$\Psi_{n,\vec{k}}(\vec{r}) = \sum_{\vec{G}} c_{n,\vec{k}}(\vec{G}) e^{i(\vec{k}+\vec{G})\cdot\vec{r}}, \tag{4.30}$$

these calculations converge as a function of the basis size. Most importantly, the physical quantities converge by adjusting a single parameter: the cut-off kinetic energy,

$$E_{\text{cut}} \geq \frac{\hbar^2|\vec{k}+\vec{G}|^2}{2m}, \tag{4.31}$$

which defines a sphere of reciprocal lattice vectors. However, the large number of electrons require a large cut-off energy.

A final approximation is implemented which separates the electrons into two categories: core electrons, which are bound (frozen atomic configuration) to the nucleus, and valence electrons. An effective potential, referred to as the *pseudopotential*, replaces the interaction between these two classifications of electrons. This approximation reduces the number of plane-waves required in the all-electron (core and valence) calculation since only the valence electrons are considered; the valence electrons are represented as smooth pseudo-wavefunctions.

4.6.1 Magnetic Shielding

For periodic systems placed in a magnetic field, there is a non-uniform magnetic field produced by the current density which arises from the electronic currents. The induced magnetic response of the system to the external magnetic field is defined by a shielding tensor which relates the two quantities

$$\vec{B}_{\text{in}} = -\boldsymbol{\sigma}(\vec{r})\vec{B}. \tag{4.32}$$

Calculating the shielding tensor requires perturbatively calculating the induced current which, in linear order, consists of diamagnetic and paramagnetic terms [101] and the inclusion of a symmetric gauge as a vector potential.

However, separating the core and valence electrons in a gauge invariant manner results in the disregard of the chemical shifts from the core electrons [103]. In order to include effects

from the the core electrons, their contribution should be purely diamagnetic and the gauge origin must be set at the atomic centre.

4.6.2 GIPAW Method

The projected augmented wave (PAW) method [104] utilises a linear transformation, $\mathcal{T}$, which maps the pseudo-wavefunctions of the valence electrons, $|\tilde{\Psi}\rangle$, onto an all-electron wavefunction: $|\Psi\rangle = \mathcal{T}\,|\tilde{\Psi}\rangle$. This method, however, is computationally taxing when considering a system in a magnetic field. A magnetic field dependant transformation, $\mathcal{T}_{\vec{B}}$, is introduced [105] which is independent of where the gauge origin is set. This transformation imposes a mapping which is exactly invariant and the approach is referred to as the gauge including projected augmented wave (GIPAW) method. The GIPAW method is computationally more viable when extended with an ultrasoft pseudopotential (USPP) [106].

Figures 4.6 shows the computed uncorrected and corrected magnetic shielding for a the nuclear sites in range of isolated molecules. These calculations include GIPAW-USPP scheme along with a large basis set of chemical calculations on the following molecules: CH_4, CH_3F, C_6H_6, TMS, SiH_3F, Si_2H_4, SiH_4, CO, CF_4, SiF_4, PF_3, P_2, and P_4 [107]. The sold line in both figures represent a perfect agreement.

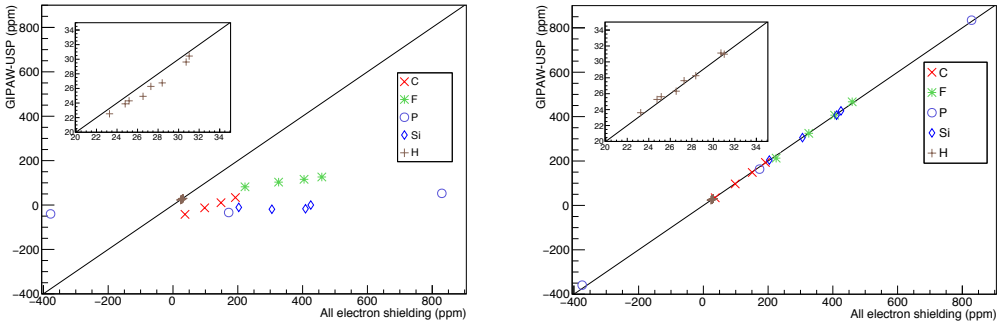

(a) (b)

FIGURE 4.6: Magnetic shielding for the nuclear sites in isolated molecules where (a) only the individual gauges for the atoms are computed, and (b) the GIPAW-USPP method is implemented for the all-electron response. Adapted from [106]

Figure 4.6a displays the uncorrected shielding for the individual gauges for the atoms in the molecules which neglects the effects of the currents arising from the core electrons. It is

clear that the chemical sensitivity is lost and as there is very little agreement, that is, that the data points do not follow the trend of the solid line. Figure 4.6b displays the corrected shielding for the all-electron response and an almost perfect agreement is shown.

4.6.3 Calculation of EPR Parameters

The implementation of the GIPAW-USPP method allows for the calculation of chemically sensitive magnetic properties. In particular, the paramagnetic defects in a system can be studied by considering the following effective EPR Hamiltonian:

$$\hat{\mathcal{H}}_{\text{eff}} = \frac{\alpha}{2}\,\vec{B}^{T} \cdot \mathbf{g} \cdot \hat{\vec{S}} + \sum_{I} \hat{\vec{S}}^{T} \cdot \mathbf{A} \cdot \hat{\vec{I}}, \tag{4.33}$$

where α is the fine structure constant[3]. Calculating the **A**-tensor implements the use a PAW based method [108]; however, the **g**-tensor calculation implements the GIPAW method, specifically in an extended defected crystalline structure [109].

The **g**-tensor calculations begin with the electronic Hamiltonian which include terms up to the order of α^3. Thus, the Electron-Zeeman term is accompanied by the the Electron-Zeeman kinetic energy correction, the SO, and the spin-other-orbit terms. This Hamiltonian is perturbatively expanded leading to Equation 4.17. The $\Delta\mathbf{g}$-tensor contains information from the three additional terms. It's components are of the order of several parts per million (ppm).

4.6.4 Chemical Potential Calculations

Within the constrained DFT formalism [110], the chemical potential appears as a Lagrange multiplier when minimising [83] an N-electron ground-state density given by

$$\mu = \frac{\delta F}{\delta n(\vec{r})} + v(\vec{r}). \tag{4.34}$$

This introduces a so-called universal functional, $F[n(\vec{r})]$, which defines the number of particles and a uniquely determined external potential.

[3]The calculations of these tensors employ atomic units.

If the particle number is changed, the change in the ground state energy is defined as

$$\mu(N) = \left(\frac{\partial E}{\partial N}\right) \tag{4.35}$$

which is the chemical potential. Extending this constraint from wavefunctions to ensembles (which contain wavefunctions with different numbers of electrons) introduces a fractional number of particle numbers [111]. These particle numbers arise in systems allowed to interact with the surroundings and exchange electrons. A derivative discontinuity at each integer of the ground-state energy $E(N)$ arises due to part of the XC energy. The Kohn-Sham eigenenergies ε in a state i are given by

$$\varepsilon_i = \frac{\partial E}{\partial n_i}, \tag{4.36}$$

where n is occupation number. The highest occupied (HO) Kohn-Sham eigenvalue is then equal to the chemical potential, that is

$$\varepsilon_{\mathrm{HO}} = \mu \tag{4.37}$$

which is equal to Equation 4.35. This definition of $\varepsilon_{\mathrm{HO}}$ changes discontinuously. It is now possible to define the eigenenergies of a Z-electron system in terms of the ionisation energy E_{ion} and electron affinity[4] E_{aff}. The HO Kohn-Sham eigenvalue becomes

$$\varepsilon_{\mathrm{HO}} = \begin{cases} -E_{\mathrm{ion}} & \text{if } (Z-1 < N < Z) \\ -E_{\mathrm{aff}} & \text{if } (Z < N < Z+1). \end{cases} \tag{4.38}$$

[4]The electron affinity is the amount of energy spent adding an electron, in the gaseous phase, to a neutral atom to form a negatively charged ion.

Chapter 5

Experimental and Computational Techniques

This chapter details the methodology and sample preparation for the experimental and computational EPR experiments and simulations, respectively. In order to simulate the effects radiation damage has on plastic scintillators in the TileCal, Monte Carlo calculations were performed on PVT and PS samples using protons with 6 MeV energy. This choice of energy was motivated by the limitations of the accelerator employed to accelerate protons at the plastic targets.

Approximate computational models were used to model the polymer structures of the plastics, since these proved computationally complex to model. Ionising radiation damage was simulated by simply removing hydrogen atoms from the structures. EPR parameters were extracted from these calculations for a damaged and undamaged system in the models.

5.1 Monte Carlo Simulations of Damaged Plastics

The Monte Carlo (MC) simulated interactions between ions and matter was computed with the SRIM (Stopping Range of Ions in Matter) [42] software package. This quantum mechanical approach of calculating the stopping power and range of ions accelerated towards a so-called all atom target includes the effects from Coulomb screening, as well as exchange and correlation interactions [42]. In particular, in order to calculate the desired parameters for the interaction between hydrogen ions (protons) and both PS and PVT, respectively, the Core and Bond (CAB) approached is included in the calculations to account for the bond energy changes in materials (see Section 3.2.1).

An extension of the SRIM package is TRIM (Transport of Ions in Matter) which calculates the kinematic information and parameters relating to interactions of the ion while traversing complex targets made of compound materials. Figure 5.1a depicts the track formation of 6 MeV hydrogen ions traversing 600 µm thick PS in the x- and y-direction. The simulations for PVT show similar track formations for 600 µm thick sample. The calculated energy loss due to ionisation was 99.93% for PS and 99.94% for PVT, respectively.

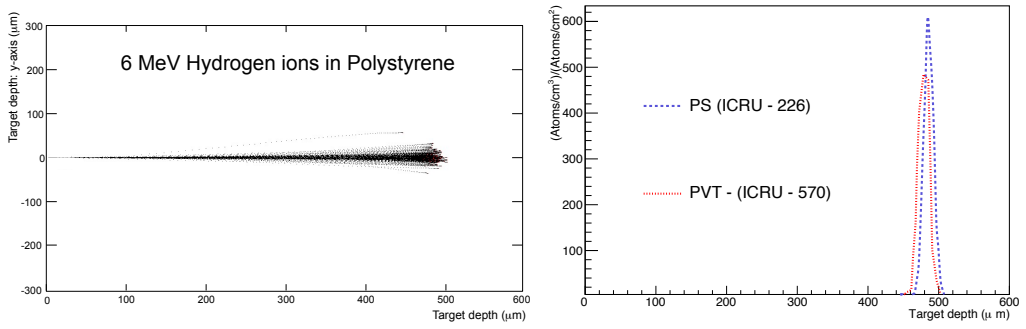

(a) (b)

FIGURE 5.1: TRIM simulations of (a) 6 MeV hydrogen ions traversing 600 μm PS, and (b) the ion ranges for PS and PVT.

Figure 5.1b displays the ion ranges for both PS and PVT[1]. The negative ions stop in both PS and PVT a distance of 484 µm and 476 µm, respectively. Therefore, in order to ensure that ions of this energy do not stop within the plastics, a thickness of between 250 µm and 350 µm

[1]The International Commission on Radiation Units and Measurements (ICRU) labels indicate the compounds used which are available in the SRIM Compound Directory.

was chosen. A smaller thickness, however, would introduce complications when machining the plastic samples. Then for samples of this thickness, an estimated average energy lost per proton (E_{loss}) was between 2.07 MeV and 2.8 MeV [112]. This result was needed in order to calculate the total absorbed dose each sample received.

5.2 Investigated Plastic Scintillators

Six plastic scintillators were investigated; they were either of PS or PVT polymer base. The chemical differences between these two bases has been outlined in Section 3.4.

Scintillator name	EJ200	EJ208	EJ260	Dubna	Protvino	Bicron
Manufacturer	Eljen Technology	Eljen Technology	Eljen Technology	ISMA, Kharkiv	IHEP, Protvino	Saint Gobain Crystals
Polymer base	PVT	PVT	PVT	PS	PS	PVT
Primary fluor	Organic fluors (0.3%)	Organic fluors (0.3%)	Organic fluors (0.3%)	PTP (2%)	PTP (1.5%)	-
Secondary fluor	-	-	-	POPOP (0.03%)	POPOP (0.044%)	-
Wavelength of max. emission (nm)	425	435	490	425	-	425
Density (g/cm^3)	1.023	1.023	1.023	1.06	-	1.032

TABLE 5.1: Investigated plastic scintillators and relevant properties.

Table 5.1 summarises the plastic scintillators investigated and their relevant properties. Each plastic is briefly discussed.

EJ200 is a blue emitting scintillator useful for time-of-flight measurements when they are greater than 1 m in length. They have the largest light output of the studied plastic scintillators (64%) when compared to anthracene.

EJ208 has the longest wavelength of maximum emission of the blue emitting scintillators making it the most desirable scintillator for light collection.

EJ260 is the only green emitting scintillator and has the longest wavelength of maximum emission. These longer wavelength emitting scintillators couple better to photo-sensors and display more resistance to radiation damage than blue emitting scintillators.

Dubna is a general purpose, blue emitting scintillator and is commonly referred to as UPS923A. This scintillator is utilised in the ATLAS detector as the MBTS plastic.

Protvino has a similar chemical composition to the Dubna scintillator apart from the differences in concentration of added fluors. They are also utilised in the ATLAS detector within the Barrel region of the TileCal.

Bicron is commonly referred to as BC408 and has a similar chemical composition to the EJ200 plastic and are also used for time-of-flight measurements. The added fluors have not been made public.

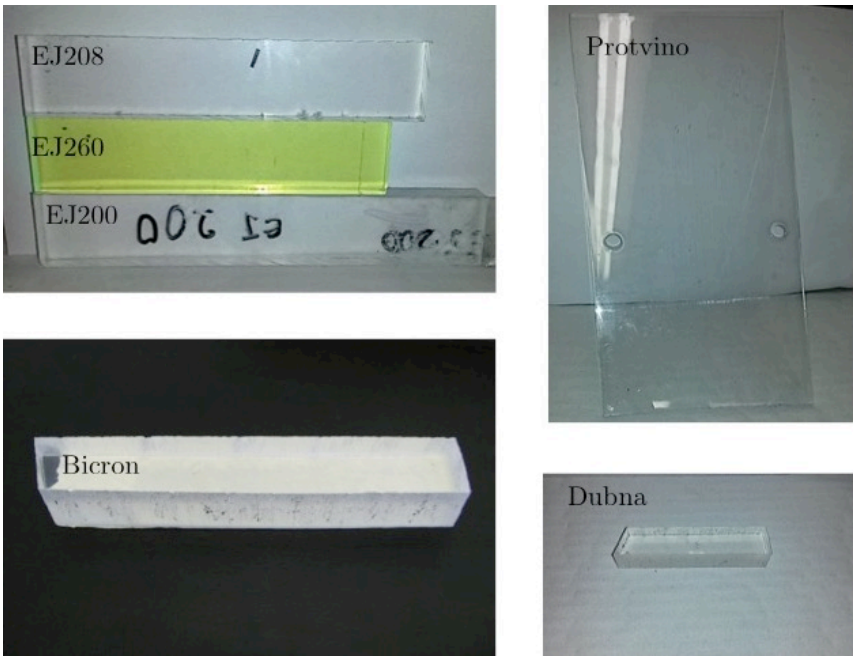

FIGURE 5.2: Photographs of the six plastic scintillators used in the study (not pictured to scale).

Figure 5.2 displays photographs of the six plastics investigated and their varying dimensions (not pictured to scale). The method used to machine the plastics to the desired dimensions is described in the next section.

5.3 Scintillator Sample Preparation

The desired dimensions of each sample were a 5 mm by 5 mm square. This area was required for the samples to fit into the recess of a aluminium holder for polishing. Figure 5.3a is a photograph of a Buehler IsoMet low speed saw which was used to cut the plastics (in this case EJ260) into a 5 mm $\times$ 5 mm rectangular bar. A 225 g load was placed onto the plastic weighting it down onto a lubricated, rotating, diamond finished blade cutting into it. The rectangular bar was then cut into 1 mm thick squares measured with the micrometer on the IsoMet.

Samples were placed into the recess of the aluminium holders in order to be polished to the desired thickness. These holders, shown in Figure 5.3b, were designed with a recess which has dimensions 6 mm × 6 mm × 0.36 mm to accommodate the sample and an attachment to connect to the polisher.

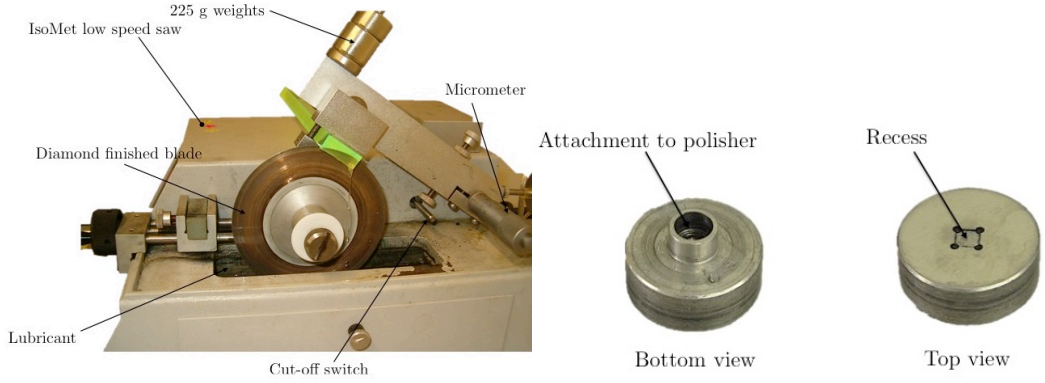

FIGURE 5.3: Photographs of (a) the Buehler IsoMet low speed sample holder cutting an EJ260 plastic, and (b) the bottom and top view of aluminium sample holders.

The samples were mounted in the recess with carbon tape which was chosen as it did not react with the plastics during polishing. A Struers metallographic polishing machine, shown in Figure 5.4 was used to polish the samples. The sample holders, with samples in place, were mounted onto the polishing head where a 2 Newton force pushed it down onto a lubricated polishing cloth. Two polishing stages were implemented: the medium polishing utilised a stage 6 µm diamond suspension on a satin woven polishing cloth; the fine polishing utilised a 1 µm diamond suspension on synthetic fibre cloth.

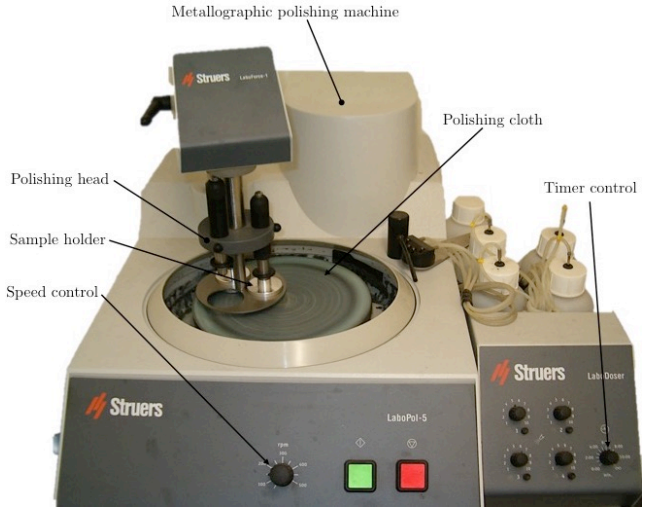

FIGURE 5.4: Photograph of the Struers metallographic polishing machine and aluminium sample holders.

The polishing head's rotation speed and time of polishing were controlled and varied depending on length of time required to polish each sample. Once samples reached the desired thickness, they were carefully removed from the sample holders and the carbon tape was pealed off. Samples were rinsed off in warm water. They were then soaked in ethanol using a Jeken ultrasonic cleaner for 30 minutes to remove any residual from the samples. Samples were then left to dry overnight.

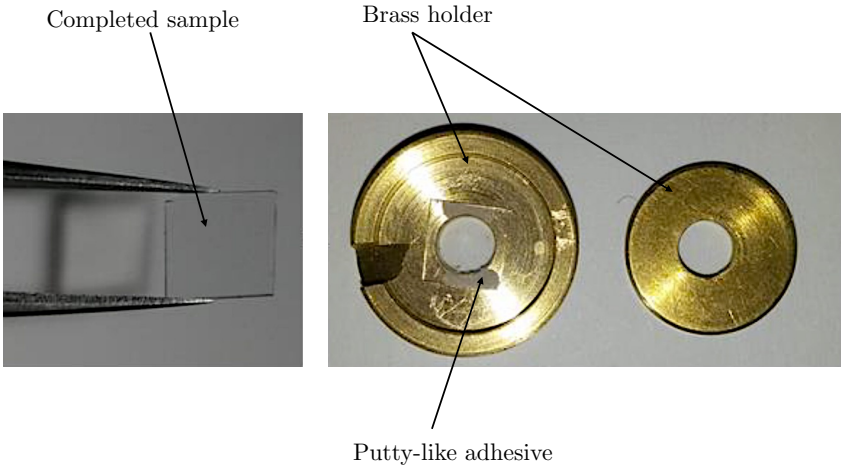

FIGURE 5.5: Photograph of a completed (Dubna) sample mounted into a brass holder with putty-like adhesive.

Figure 5.5 shows the polished Dubna sample which was fitted into a brass holder ready for irradiation. In order to ensure that the sample did not move around during irradiation, a putty-like adhesive was used to mount it onto the brass holder.

5.4 Sample Irradiation

Sample were irradiated to increasing doses with 6 MeV protons accelerated by the 3 MV Van de Graaf accelerator at iThemba Laboratory for Accelerator-Based Sciences (LABS) in Gauteng. Figure 5.6 depicts a computer generated representation of the tandem accelerator.

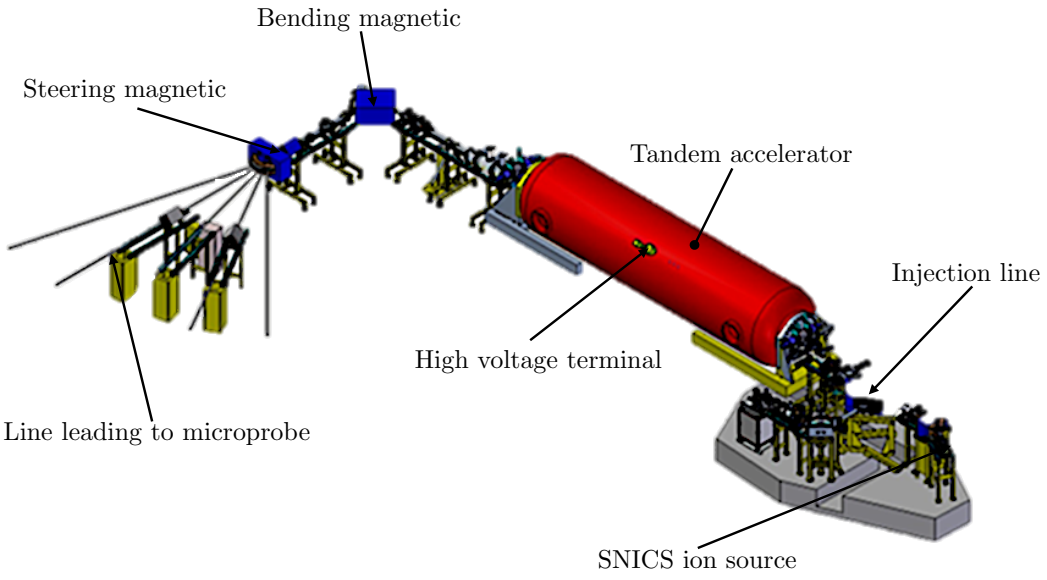

FIGURE 5.6: A computer generated representation of the tandem accelerator at iThemba LABS, Gauteng.

The process of generating an ion beam of 6 MeV protons with which the samples are irradiated is briefly described. A 860 A SNICS (source of ions by caesium sputtering) ion source produced negative hydrogen by ionising caesium (Cs) vapour and accelerating the negative ion beam towards the injection line. Within the injection line, the negative ion beam's energy was stabilised and focused using einzel lenses and it's current monitored by Faraday cups. The beam was accelerated into the grounded tandem accelerator tank by a 3 MV voltage terminal. This voltage was maintained by a Pelletron charging system which utilises cylindrically shaped metallic pellets connected to a belt that continuously recharge the terminal. This charging system accelerated the beam to approximately 3 MeV.

Inside the tank, the beam interacted with a gas stripping canal which was kept at a charged state equilibrium. This interaction removed electrons from the beam resulting in a positively charged beam. The beam was then accelerated towards the end of the tank with the aid of the Pelletron charging system. The resulting positively charged beam that exited the tank was approximately 6 MeV. The beam then entered a bending magnet which bent particles with the desired charge and momentum (in this case protons) towards a steering magnet. The steering magnets, which act as a switch, pass the 6 MeV proton beam down the beam line leading to the nuclear microprobe chamber. Figure 5.7 is a photograph of the beam line

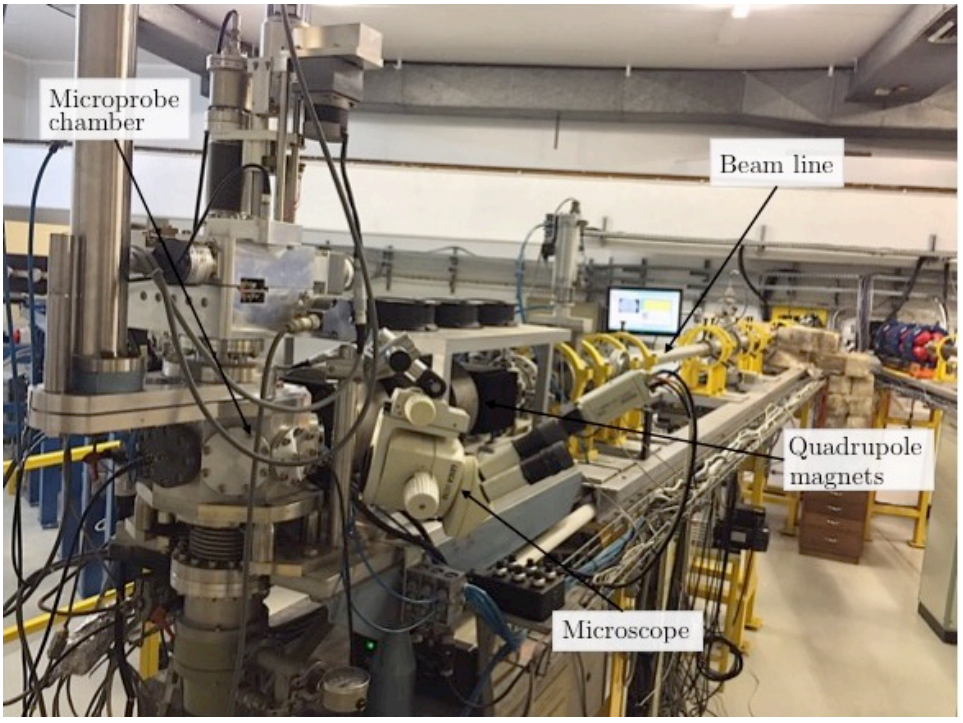

FIGURE 5.7: Photograph of beam line leading to the microprobe chamber.

leading to the microprobe which were all kept under vacuum. The beam passed through slits, and quadrupole magnets, which act as lenses, focused the beam spot onto the sample approximately 25 μm in size. The sample was mounted onto a carousel which housed a mounter for the brass holder. A microscope was used to ensure that the beam was on target with the sample before and during irradiation. In order to achieve uniform irradiation of the sample, the beam was scanned in the x-y plane in parallel lines forming a rectangular shape approximately 1.8 mm by 1.8 mm. The target doses for the irradiated samples were 0.8 MGy, 8.0 MGy, 25.0 MGy, 50.0 MGy, and 80.0 MGy. For each plastic scintillator, two samples were irradiated to these target doses. During irradiation, a feed, depicted in Figure 5.8, measured

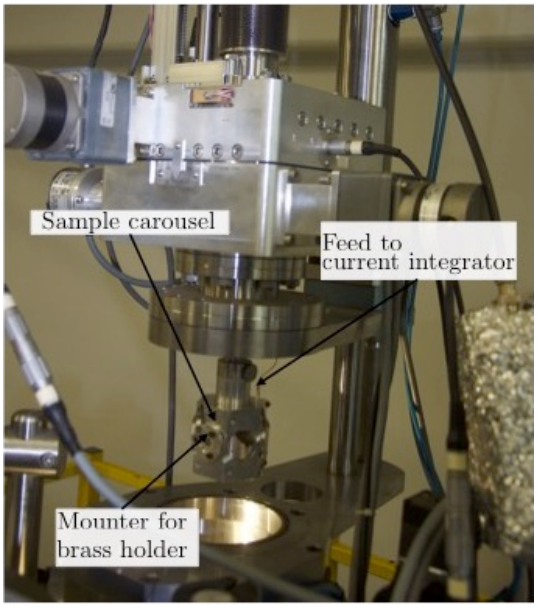

FIGURE 5.8: Photograph of the nuclear microprobe connected to the carousel with sample holder in place.

the integrated beam current every five seconds. Once the target dose was absorbed by the sample, the beam was switched off and the carousel was rotated to an un-irradiated sample. After irradiation, samples were removed from the carousel and brass holders were placed into containers.

5.4.1 Absorbed Dose Calculation

In order to calculate the dose absorbed by each sample during irradiation, the following relation was utilised

$$D_{\mathrm{Abs}} = \frac{i\ t\ E_{\mathrm{loss}}}{m\ q} \quad \mathrm{Gy}, \tag{5.1}$$

where m is the mass of the irradiated spot (calculated using the area of the spot and sample density), q is the charge of the proton, E_{loss} is the average energy lost per proton during irradiation (determined by the TRIM calculations), t is the total duration of irradiation, and i is the integrated beam current measured by the feed connected to the carousel. Appendix A.2 displays the integrated current plots for each sample represented in this study.

5.5 Continuous-wave EPR Spectroscopy

A Bruker ESP-300E EPR spectrometer was used to acquire the EPR spectra. In general, the dimensions of various components in an EPR spectrometer are specific to the microwave frequency required [83]. EPR spectrometers are, therefore, classified by microwave frequency ranges corresponding to the magnetic fields and the components utilised by the spectrometer. The main components of a ESP-300E X^2-band EPR spectrometer is described. The possible experimental arrangement for a general spectrometer is depicted in Figure 5.9.

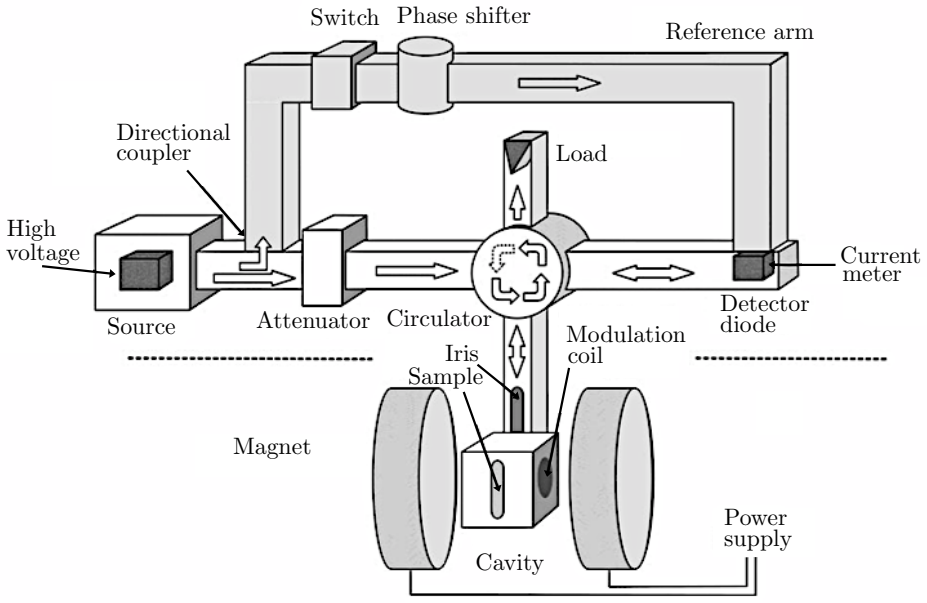

FIGURE 5.9: Schematic of an X-band EPR spectrometer. Adapted from [113].

The source region contains components which provide EM radiation. The magnet system provides a static, stable, and variable magnetic field. The cavity system contains the paramagnetic sample and detects the microwave radiation. The modulation coils amplify the signal from the paramagnetic sample; this signal is then detected by the detector diode. If necessary, the phase of the microwave is corrected by the phase shifter and its power is restored by the reference arm.

Source: The ESP 380-1010 Microwave Bridge provided nearly monochromatic, sinusoidal radiation in the X-band region around 9.5 GHz. This must be mechanically tuned

[2]This letter designation denotes the microwave frequency range in which spectrometer operates. The X-band is the most common frequency range around 9-10 GHz for a g-factor value of 2. The magnetic field is around 3400 G.

to the cavity with the use of a high voltage. The radiation incident on the sample is continuous; hence, CW spectroscopy is possible.

Resonator: In general, the resonator is a metallic, cylindrically (or rectangularly) shaped cavity capable of resonating microwaves through small opening known as the iris (depicted in Figure 5.10a). The size of the iris determines the amount of microwaves entering the cavity and the dimensions of the cavity are related to the corresponding resonant wavelengths. An ER 4118X-MD5 dielectric ring resonator was used which is a universal probe capable of coupling to an X-band spectrometer.

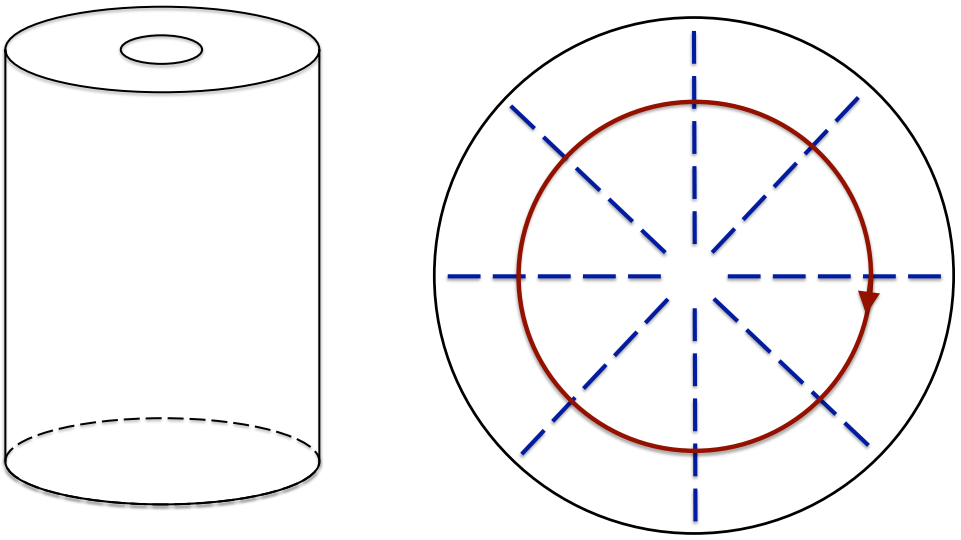

(a) (b)

FIGURE 5.10: A cylindrical microwave cavity (a), and (b) an EPR critically coupled resonator indicating the microwave magnetic and electric field components in the TE011 mode.

The main purpose of this resonator was to amplify the energy density of the incoming microwaves and optimise the detection of resonant absorption. In order to do this, the electric and magnetic components of the standing EM radiation inside the resonator must be exactly out of phase. Figure 5.10b depicted the EM field components for the ER 4118X-MD5 resonator which operates in the $TE011$[3] oscillation mode; the solid

[3]This is a group classification for oscillations within the resonator that only includes an axial components of the magnetic field. The subscript characterise the number of half waves of the EM components that fit within the diameter, circumference, and length of the resonator, respectively.

lines denote the electric field components and the dashed lines denote the magnetic field components. In order to ensure resonant absorption by the sample, the system was tuned to the cavity. This is referred to as critically coupling the cavity.

Magnetic field: A stable, controlled, and uniform magnetic field was generated by two Bruker B-E25 electromagnets which were situated either side of the resonator. The purpose of the magnetic field is to induce the desired splitting of spin energy-levels of the paramagnetic species. A regulated Bruker ER-083-CS power supply stabilised the the magnet and a Hall-effect probe measured and controlled the magnetic field by outputting a voltage proportional to B_0. The homogeneity of the magnetic field was ensured by measuring and calibrating the magnetic field at several points. This calibrates the entire EPR spectrum if the field is swept.

Detector diode: The absorbed microwave frequency re-emitted by a sample was detected by solid-state diodes. The detection of these frequencies are indicated by a changes in current using a current meter. The signal-to-noise ratio (S/N) was improved by the modulation coils which generates a static, alternating magnetic field component at the detector. This alternating signal was amplified and rectified, resulting in the first derivative of the absorption line (discussed in Section 4.2.2).

Figure 5.11 is a picture of the experimental setup in the NMR laboratory at the University of the Witwatersrand.

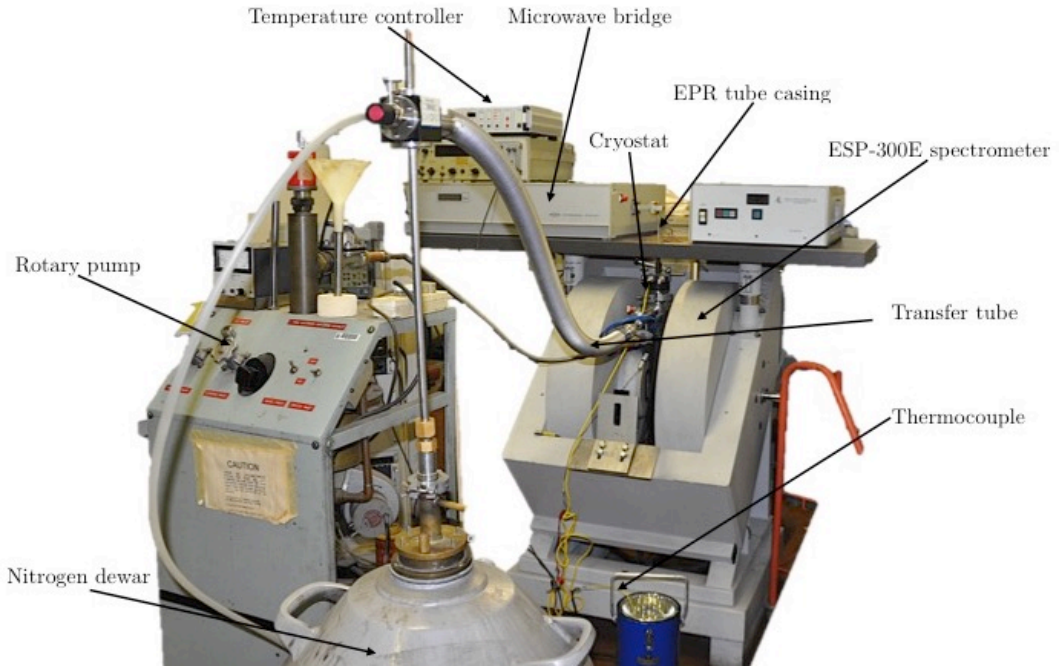

FIGURE 5.11: Low temperature EPR set up.

An EPR spectrum for each irradiated sample was acquired within one week of irradiation. The irradiated spot of each sample was removed with a surgical blade, it's area was measured, and it was placed into a quartz crystal Norell EPR tube. For un-irradiated samples, a spot of similar size was removed and placed into another EPR tube. The tube was then housed in a casing which was lowered into the cryostat.

In order to perform low temperature EPR spectroscopy, liquid nitrogen was used to cool the resonator and sample to 80 K. A Flexline ER 4118CF gas flow cryostat ensured that the sample was immersed in the liquid nitrogen. The liquid nitrogen, contained in a dewar, was pumped into the cryostat via a transfer tube; both were kept under vacuum. The temperature of the cryostat was controlled and measured with an Oxford ITC503 temperature controller. In order to ensure that the sample was also cooled to 80 K, the cryostat was cooled for an additional 15 minutes after it had reached 80 K.

Once the sample had reached 80 K, the spectrometer was calibrated and tuned to the resonator which set the resonant frequency. The magnetic field was scanned with a 50 G

sweep width in order to obtain an EPR spectrum. In total, 20 scans were run for each sample to better the S/N. The final EPR spectrum was saved and the sample and resonator was heated to room temperature before changing the sample.

5.6 Computational Models

The actual plastic structure is extremely complex and computationally taxing to model, since it is expected that that they have a high degree of disorder. Therefore, two approximate models, referred to as the toy model and the crystalline models, respectively, were investigated in order to obtain quantitative EPR predictions. No attempt was made to model disorder in the system. Instead, in both approximate models, structures were "damaged" by removing hydrogen atoms, as this is the most probable bond breakage to occur in plastic scintillators by ionising radiation [66]. EPR parameters were calculated for the undamaged (pristine) and damaged systems. The details of these calculations are described in Section 5.6.2. The four models are briefly discussed.

Toy Models: Two types of toy models were studied: a styrene monomer and three vinyl toluene isomers; their chemical structures are discussed in Section 3.4 and are displayed in Figure 3.5.

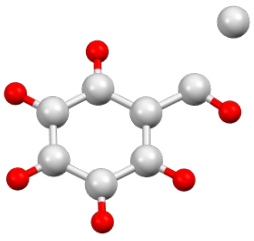

FIGURE 5.12: A computationally generated representation of damaged toy model styrene monomer, with two hydrogen atoms removed. Hydrogen and carbon atoms are represented by the red and grey spheres, respectively.

A computer generated[4] representation of the damaged styrene monomer, with two single hydrogen atoms removed, is shown in Figure 5.12. The hydrogen and carbon atoms are represented by the red and grey spheres, respectively. Each model was placed into a rectangular unit cell which was periodically repeated. These unit cells were large enough to prevent direct bonding between monomers, yet small enough so as not to completely isolate them. Furthermore, a computational trade-off was made since too large a unit cell would have run the risk of exhausting computational resources and time, but too small a unit cell could decrease the accuracy for the isolated system.

MUKLAF: This is a small, crystalline stereoisomer[5] model of PS. The chemical composition is similar to that of 2,4,6-triphenylheptane [114]. Figure 5.13a depicts a computer generated representation of the pristine MUKLAF molecule. Figure 5.13b is the complete MUKLAF model containing 92 carbon atoms and 88 hydrogen atoms.

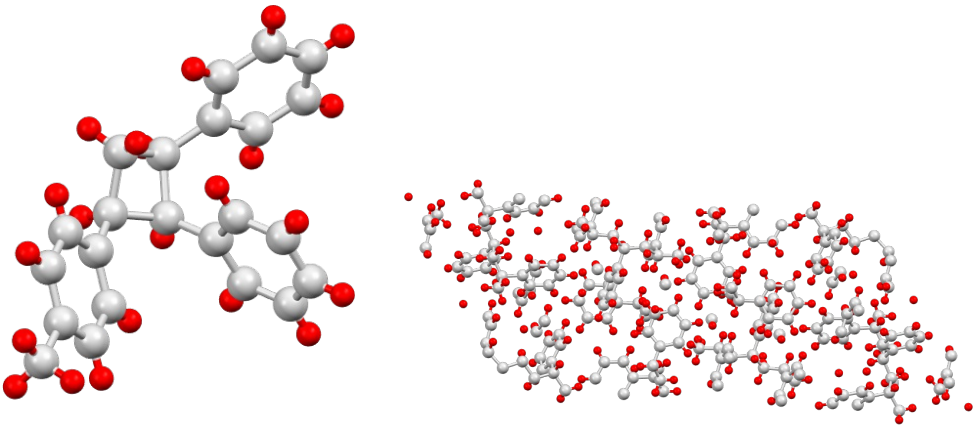

(a) (b)

FIGURE 5.13: A computer generated representation of (a) the MUKLAF molecule, and (b) the complete MUKLAF unit cell containing 92 carbon atoms and 88 hydrogen atoms.

PolySty: This is stereoisometic, crystalline molecular complex, displayed in Figure 5.14a, and is also a model of PS. It consists of a limited number of monomers (referred to as an oligomer) and has a similar chemical composition to 2,4,6,8-tetraphenylnonane [115]. The oligomer is repeated multiple times within the unit cell, and the complete model contains 132 carbon atoms and 144 hydrogen atoms. This is shown in Figure 5.14b.

[4]The Mercury crystal structure visualisation program was used to visualise, manipulate and rotate the molecular structures.

[5]An isomer of a molecule consisting of the same atoms and atomic configuration, but different spatial orientations.

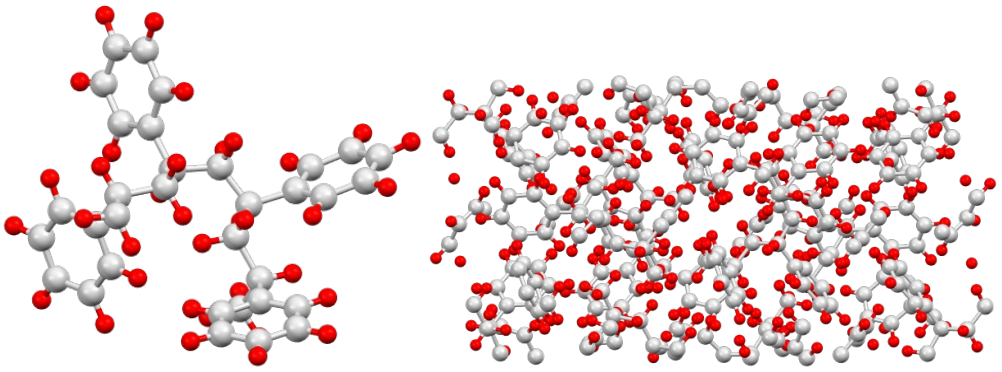

(a) (b)

FIGURE 5.14: A computer generated representation of (a) the PolySty molecule, and (b) the complete PolySty model containing 132 carbon atoms and 144 hydrogen atoms.

In order to simulate the effects of an increase in dose due to ionising radiation, EPR parameters were calculated before and after the structures are damaged. Changes in the EPR parameters provided quantitative insights into structural features that may have arisen in anomalous EPR signatures after sample irradiation. It should be noted that, in the two larger crystalline models, a degree of local disorder is exhibited due to the different orientations of the styrene molecules. Damaged systems consisted of structures where one, two, or three hydrogen atoms are removed from the structure. Finally, before calculating the EPR parameters, structures (pristine and damaged) are allowed to relax in order to find their atomic configurations which are stable and are at equilibrium.

5.6.1 Structural Relaxation

The Vienna ab initio simulation package (VASP) [116] is a DFT atomic scale modelling tool which uses a projector augmented wave (PAW) method to calculate the electronic structure of the models. VASP was used to relax the structures using the PBE (GGA) exchange-correlation approximation [117] with a $\vec{k}$-point mesh of 1000 per reciprocal atom. To ensure that the structure was relaxed, the error for all forces were converged to within 1 meV/Å and the converged cut-off energy, E_{cut}, was set to 320 eV. This is slightly lower than the recommended value of 520 eV[6] but a a compromise between high numerical accuracy and

[6]This standard value is recommended by the Materials Project. It is based on extensive tests with VASP, and is 1.3 times larger than the highest E_{cut} recommended among all pseudopotentials. Additional information can be found at https://materialsproject.org/docs/calculations.

computational time. A higher cut-off did not change the relaxed structures in any meaningful manner. The relaxation calculations predicted the magnetisation of the structures. However, since VASP does not include a GIPAW extension, the calculated relaxed structures and magnetic moments were fed into another simulation package (see Section 5.6.2).

The chemical potential predictions (see Section 4.6.4) obtained from the VASP calculations were used to gain an understanding of possible electron transfer between systems for damaged toy model compounds. This information was needed when plotting the EPR signals for the pristine and damaged structures. Section 6.3 details the plotting of these signals.

5.6.2 QE-GIPAW Calculations

Quantum Espresso (QE) [118] is an *ab initio*[7] simulation packaged used to calculate electronic structure of materials within DFT using pseudopotentials and planewaves. An extension of QE is the QE-GIPAW package which was used to calculate the EPR parameters for the structures which included the EPR electronic **g**-tensor and hyperfine **A**-tensor. The Troullier-Martins soft pseudopotential [119] was used to accommodate the GIPAW calculations and the E_{cut} was set to 50 Rydberg (Ry). A single $\vec{k}$-point (Γ-point) grid was used for the calculations in order to decrease computational time. Results obtained using a larger number of $\vec{k}$-points showed inconsequential changes in the EPR parameters.

EPR parameters were calculated for relaxed pristine and damaged structures and presented in tensor form with components in units of ppm.

[7] A Latin phrase which translates to "starting from the beginning".

Chapter 6

Results and Observations

6.1 Discolouration and Brittleness

An orange-yellow discolouration was observed after irradiation of each sample at the spot where it was irradiated. Samples irradiated for longer periods of time exhibited darker discolourations. Once samples were removed from the nuclear microprobe, which was kept under vacuum, the exposure to the atmosphere resulted in this discolouration fading with time. In particular, fading occurred within several minutes for all samples irradiated to a dose of 0.8 MGy target and, within several days, they closely resembled the un-irradiated ones. Before this occurred, the irradiated spots for all samples were removed from the sample with a surgical blade. Fading occurred slower for samples irradiated to higher doses. All samples above the 0.8 MGy target dose maintained a degree of discolouration throughout the investigation.

Care was exercised during the handling of samples irradiated to doses larger than the 8.0 MGy target dose. These samples, particularly at their edges, became brittle and in the case of the Protvino samples had fractured into smaller pieces. Consequentially, the irradiated spots of these samples were less challenging to remove.

6.2 Experimental EPR Results and Observations

6.2.1 Spectral Shift

The six plots in Figure 6.1 show the EPR spectra obtained from the un-irradiated and irradiated spots of each plastic scintillator sample. EPR measurements were taken within two weeks of sample irradiation to ensure permanent damage at sample temperatures of 80 K.

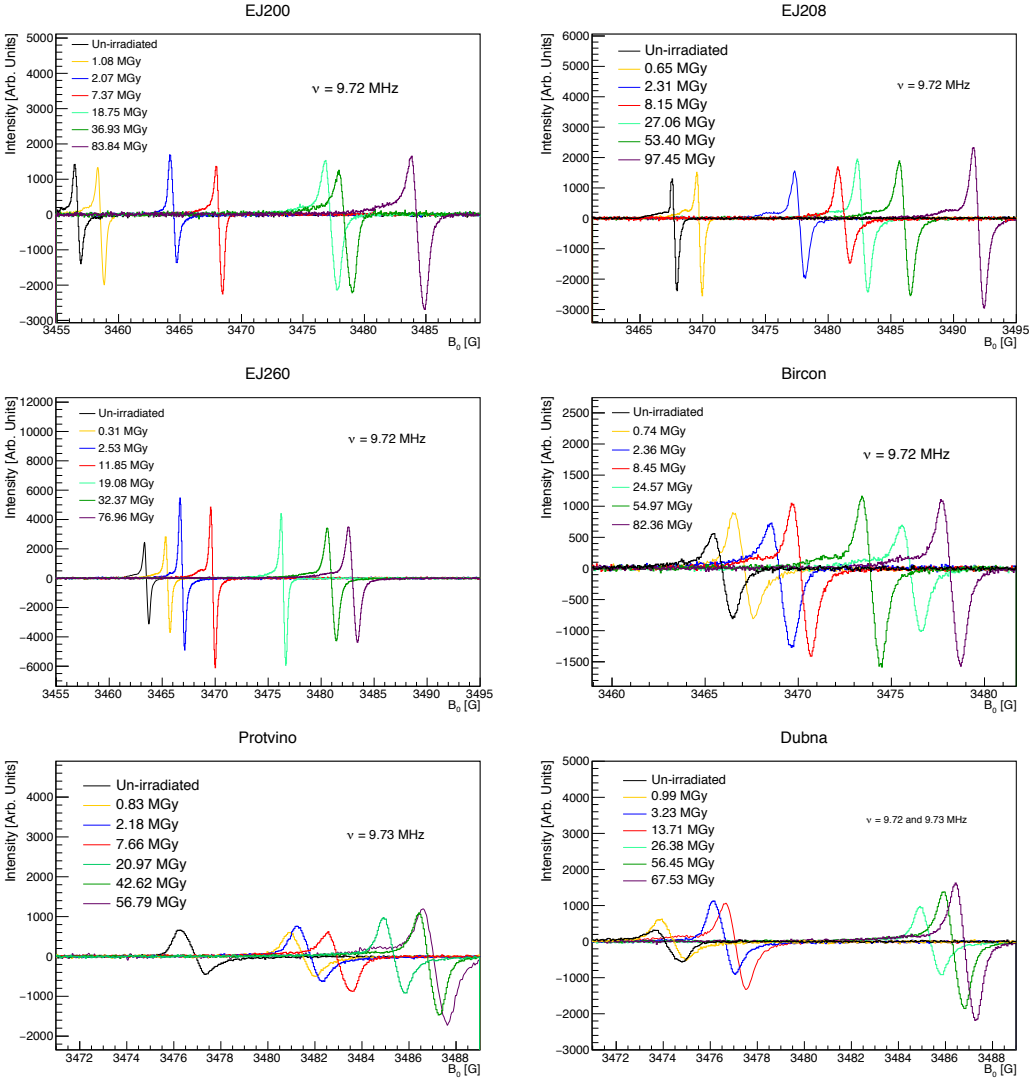

FIGURE 6.1: Effect of dose on EPR spectra for each plastic scintillator type taken at 80 K within 2 weeks of irradiation.

Each EPR spectrum in the six plots above consists of a single peak of approximately 5 G. The increased dose results in a general shifting of the EPR spectra along x-axis to larger magnetic fields with respect to the un-irradiated spectrum. In the case of the Bicron sample irradiated to 24.57 MGy, its shift away from the irradiated spectrum is larger than the sample which received a dose of 54.97 MGy. It is possible that this larger shift is attributed to human error when placing the EPR tube into the spectrometer. If the tube is not held in the casing correctly, it has the tendency of sliding down into the cavity to a lower position and, after tuning, obtaining an observed larger magnetic field at the same resonant frequency. In an attempt to eliminate this error, the tubes were glued to the EPR tube casing at the same position before each measurement. However, the possibility exists that the tube still moved in the casing.

Each spectrum appears within the sweep width range of the spectrometer which was set to 50 G. The PVT spectra generally span this range whereas the PS spectra only appear within a range of approximately 20 G. Furthermore, the six figures indicate that the shift to larger magnetic fields is not uniform. It is also observed that the peak intensities and ΔB_{PP} vary as dose increases. These features, along with the relative g-factor changes are discussed below.

6.2.2 Relative Decrease in g-factor

Figure 6.2 displays the relative change in the g-factors with respect to the un-irradiated sample's g-factor (g_0) as a function of dose at 80 K. These values were obtained by satisfying the resonance condition and solving for g, that is, the magnetic field value at the peak height of the integrated EPR spectrum was added to Equation 4.10 along with the resonant frequency at which the magnetic field was swept. Fits to the integrated EPR spectra can be found in Appendix A.1.

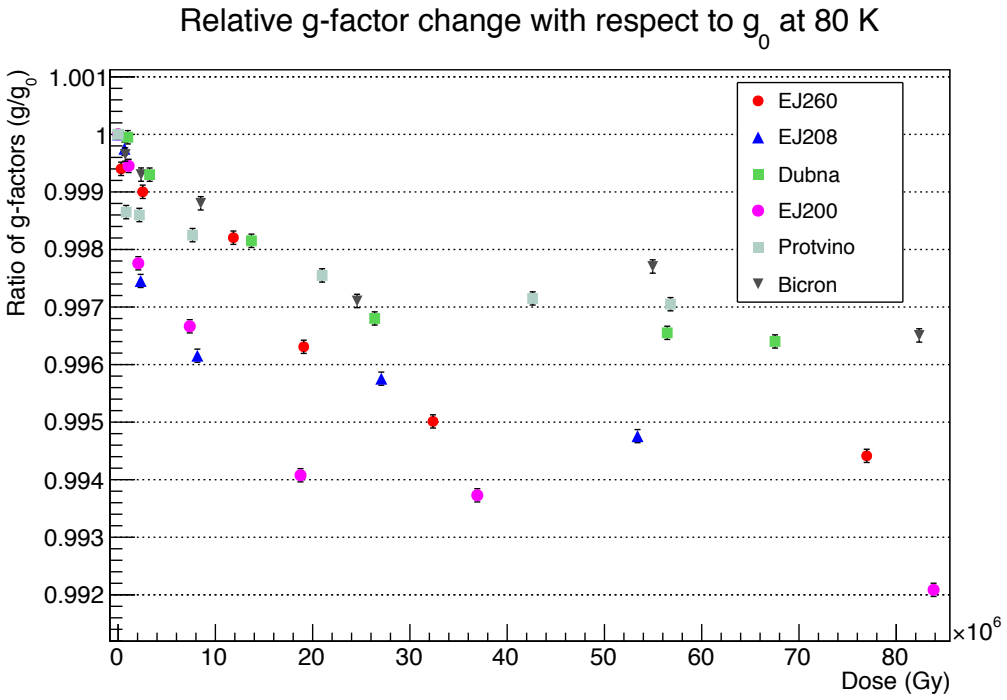

FIGURE 6.2: Effect of dose on the relative change in the g-factors at 80 K.

A general decrease in the g-factor is observed in all samples as dose increases and its relative decrease is no more than 0.8% for all irradiated samples. The trends in relative shifts for the Eljen samples are similar, with the largest relative shifts observed in EJ200. PS based samples also display have shifts. Bicron exhibits the overall smallest relative decrease in g-factor.

It should be noted that all resonant frequencies, ν, for PVT samples occurred at 9.72 MHz and, barring the Dubna sample irradiated to 13.71 MGy with $\nu = 9.72$ MHz, PS samples had resonant frequencies at 9.73 MHz. These results are tabulated in Tables A.1 and A.2

6.2.3 Peak-to-peak Variation

The variation in the EPR spectra peak-to-peak (ΔB_{PP}) is shown in Figure 6.3 versus an increase in dose. These values were calculated by obtaining the difference between the magnetic field values at the EPR spectrum's maximum and minimum. It is observed that there is a general increase in ΔB_{PP} for the PVT based scintillator types but a decrease in ΔB_{PP} PS based scintillator types as dose increases. EJ200, EJ208, and EJ260 show a similar

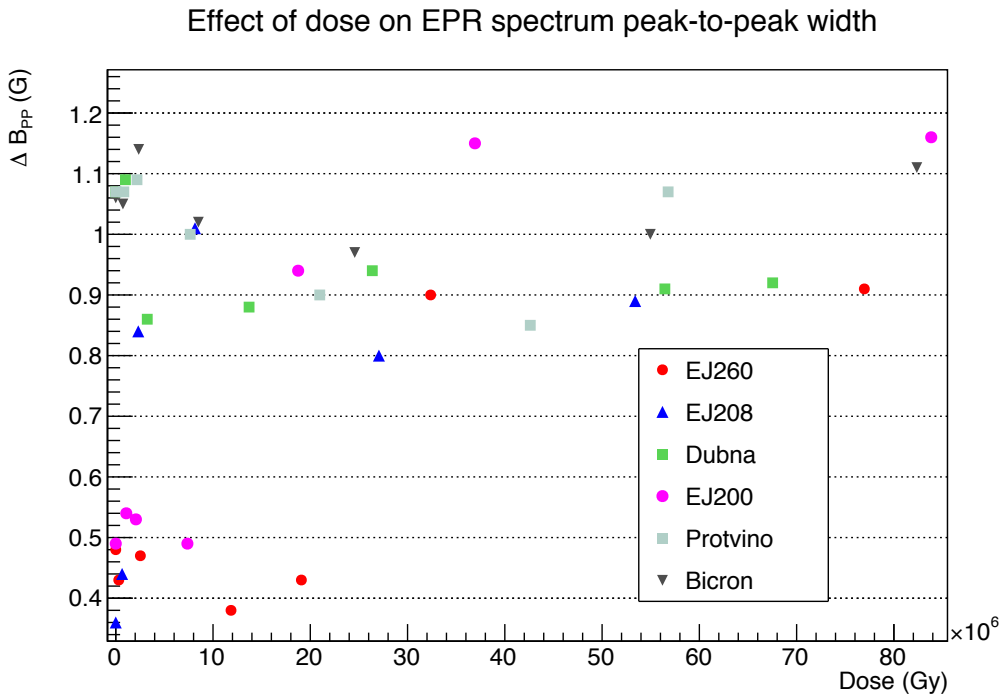

FIGURE 6.3: Effect of dose on the peak-to-peak width at 80 K.

general increase in ΔB_{PP} from approximately 0.4 G to approximately 1.2 G. A similar trend is seen in the Bircon sample but its increase is less considerable, ranging from 1.06 G to 1.11 G. The slight decrease in ΔB_{PP} for both Dubna and Protvino start at 1.07 G and end at 0.9 G and 1.06 G, respectively.

6.2.4 Relative Intensity Increase

Figure 6.4 shows the effect the increase in dose has on the relative intensities per unit volume of the irradiated spot. The arbitrary intensities of each sample (I) were divided by their respective un-irradiated sample's intensity (I_0) and normalised to the volume of the irradiated spot (in cm^3). In general, for each scintillator type, this normalised intensity increases as the dose absorbed by the sample increases.

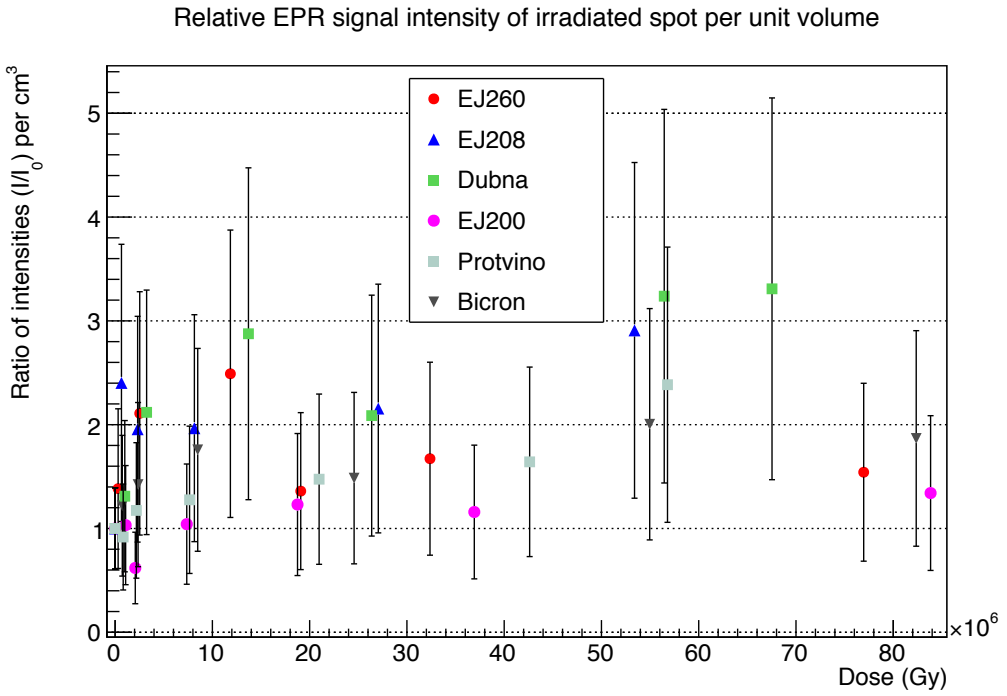

FIGURE 6.4: Effect of dose on the relative intensities normalised to the volume of the irradiated spot.

In general, all samples display a slight decrease in normalised intensity occurring at the second or third highest dose. The largest relative increase is observed in the highest dose of Dubna sample which has a normalised intensity approximately 3 times larger than the un-irradiated spectrum's. The lowest increase is observed in EJ200 with a normalised intensity for its largest dose only around 1.3 times larger than the un-irradiated spectrum's.

6.2.5 Shoulder Formation

These observations pertain to the un-irradiated and irradiated integrated EPR spectra found in Appendix A.1. The most common shape observed from the integrated EPR spectra is that of a Crystal Ball function that consists of a Gaussian and an exponential tail usually to one side of the Gaussian. The exponential tail is observed to fall to either side of the Gaussian. This feature is attributed to the phase of the spectrometer at which the EPR spectrum was obtained. For simplification of analysis, it was assumed that this phase change had no effect on the physical interpretation whatsoever.

In many cases, the exponential tail exhibited structural features that could not be captured by the Crystal Ball function. Various functions were attempted as fits; however, the triple Gaussian function, which consists of three Gaussians, provided the best fits. It's central Gaussian captured the dominant peak, the second Gaussian could be adjusted to capture peak structure within the tail, and the third peak's width could be set large enough to capture the tail itself. Fit parameters obtained for the second Gaussian peak allowed to the calculation of a second g-factor, g_{a}, from the the peak mean. An a-value was also calculated which is the difference in magnetic field values of the first and second Gaussian peak means (measured in G). These two values were utilised in order to identify the possible radicals which formed during sample preparation and after samples were irradiated. The g_{a}-factors and a-values can be found in Tables A.1 and A.2.

6.3 Computational Results and Observations

6.3.1 Chemical Potential Results

These observations pertain to Tables B.1 and B.2 for a single isomer of the Vinyl toluene toy model. The absolute values of chemical potential, μ, and first DFT excitation energy at the band edges of the majority and minority[1] channels are displayed for pristine and damaged systems. In the plastic, electrons can move to and from a monomer. The rest of the system is considered to be a particle reservoir, and a local change in the chemical potential can result in a change in the number of electrons in a local region. The values of μ for these monomers can increase or decrease, relative to the chemical potential of the undamaged monomer, with the removal of a hydrogen atom. Higher values of the chemical potential of the damaged molecules suggest possible transfer of electrons from the undamaged monomers of the plastic. Whereas lower values suggest transfer to the damaged monomer. Similar results are expected for the PS toy model and the extended MUKLAF and PolySty systems. Thus, in the real plastic, electron transfer is possible to and from damaged and undamaged regions, and this has been included in the EPR spectra simulation studies. A discussion pertaining to the details of the calculations is presented in Appendix B.3.

[1] These two states can differ in the density of states formalism. Conventionally, the spin up states are referred to the majority spin and the spin down states are referred to as minority spin.

6.3.2 Simulated EPR Spectra

The **g**- and **A**-tensors calculated using the GIPAW method for both pristine and damaged systems were simulated with EasySpin[2] [120]. EasySpin is an extension of MATLAB,[3] capable of simulating and fitting EPR spectra. In particular, the `pepper` function was utilised to calculate the field-swept, CW EPR spectra for the models. An example of the code is found in Code B.1.

The generated spectrum for each model, pristine or damaged, was fit using a piecewise, polynomial spline interpolation functionality with 100 data points. In the case of the damaged models, the resulting spectra were averaged over for each hydrogen atom removal. It was assumed that the likelihood of the removal was the same regardless of the position from which the hydrogen atom was removed on the molecule. An example of the average signal is shown in Figure B.2.

The following assumption was made when generating the spectra for damaged models:

- With each hydrogen atom removed, the number of electrons would increase or decrease in each damaged model.

This assumption was motivated by the chemical potential results obtained in Section 6.3.1 and further motivated by the experimental observations in Section 6.2.4. The number of electrons used in each simulation was dictated by the magnitude of the magnetic moment calculated during structural relaxation (see Section 5.6.1).

[2]EasySpin version 5.1.0 was used.
[3]MATLAB R2011b version 7.13 was used.

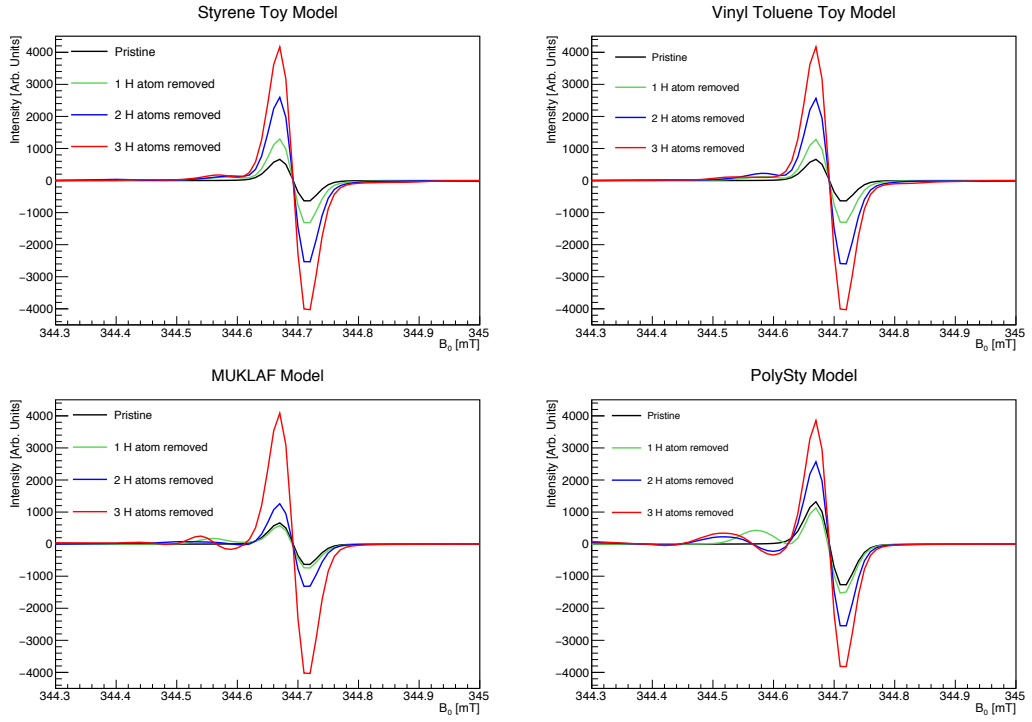

FIGURE 6.5: Simulated EPR spectra for all models. Pristine models are represented by solid black lines whereas the damaged models are represented by the solid green, blue, and red lines for the 1, 2, and 3 hydrogen atom removal.

Based on the assumption made, each averaged EPR spectrum simulated for the damaged models, shown in Figure 6.5, consisted of a single lined spectrum, and damaged models also displayed a shoulder formation observed at lower magnetic fields[4]. With each hydrogen atom removal, the signal intensity increased. No spectral shift or variation in ΔB_{PP} is observed. In all cases, the central peak registered a fixed g-factor of 2.002324 and $\Delta B_{\mathrm{PP}} = 0.5$ G.

The simulated EPR spectra for toy models are almost indistinguishable. This indicates that the structural differences between the monomers, whether pristine or damaged, have little effect on the resulting EPR spectrum. The shoulder formation is more prominent in the larger models and it spans a larger magnetic field range as more hydrogen atoms are removed.

Focus was then placed on the EPR spectrum of the radical responsible for this shoulder; its features were most predominant in the double hydrogen atom removal in the PolySty model[5]. The EPR spectrum for this radical yielded a three peaked spectrum with an intensity ratio

[4]The magnetic field of the simulated spectra are displayed in units of mT and not G as that is the standard utilised by EasySpin.

[5]Other damaged models produced similar spectra.

1:2:1, as shown in Figure 6.6a. This spectrum was obtained when the three principle values of the **A**-tensor were set to 0 and a line spacing of approximately 8 G was observed. The linewidth broadening of the ΔB_{PP} set to the standard Gaussian broadening of 0.05 mT and Lorentzian broadening of 0.01 mT.

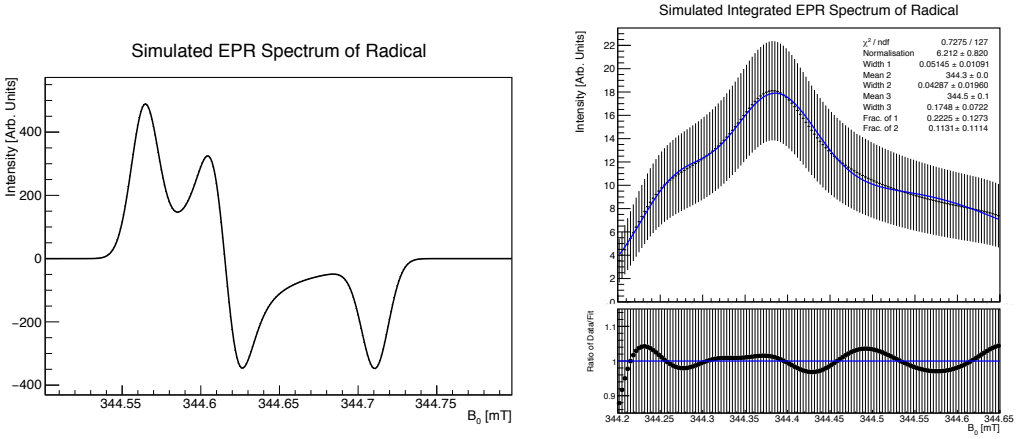

(a) (b)

FIGURE 6.6: EasySpin simulation of (a) the EPR spectrum of radical with **A**-tensor principle values set to zero, and (b) the integrated EPR spectrum with fit.

A triple Gaussian fit was made on the integrated EPR spectrum, shown in Figure 6.6b. From the fit, approximate g-factors for the peaks were calculated to be 2.0048, 2.0041, and 2.0033 for the first, second, and third peak, respectively.

The hyperfine parameters were then included into the simulations and yielded an EPR spectrum, displayed in Figure 6.7. The spectrum was obtained using a random powder spectrum orientation and the ΔB_{PP} was set to 0.02 mT to emphasise the hyperfine peaks. The resultant spectrum contained five peaks of approximately 5 G to 9 G spacing with intensity ratios 1:5:7:4:1. The principle values of the **g**-tensor were $\mathrm{g}_{xx} = 2.00221$, $\mathrm{g}_{yy} = 2.00276$, and $\mathrm{g}_{zz} = 2.00306$. The hyperfine principle values used for the simulation were $A_{xx} = 0.98$, $A_{yy} = 0.99$, and $A_{zz} = 1.97$ from the first hydrogen atom removed, and $A_{xx} = 0.518$, $A_{yy} = 1.23$, and $A_{zz} = 1.75$ from the second one removed. Simulations of the single and triple hydrogen atom removal yielded similar spectra, and hyperfine values resulted in some peaks overlapping. In general, a five peak spectrum, similar to that observed in Figure 6.7, was observed in all damaged models. In the two smaller, damaged models, the intensities of the peaks and spacings between them differed depending on where the hydrogen atoms were

removed. The EPR simulations of the two larger models, regardless of where hydrogen atoms were removed or the number of removed hydrogen atoms, yield almost identical signatures.

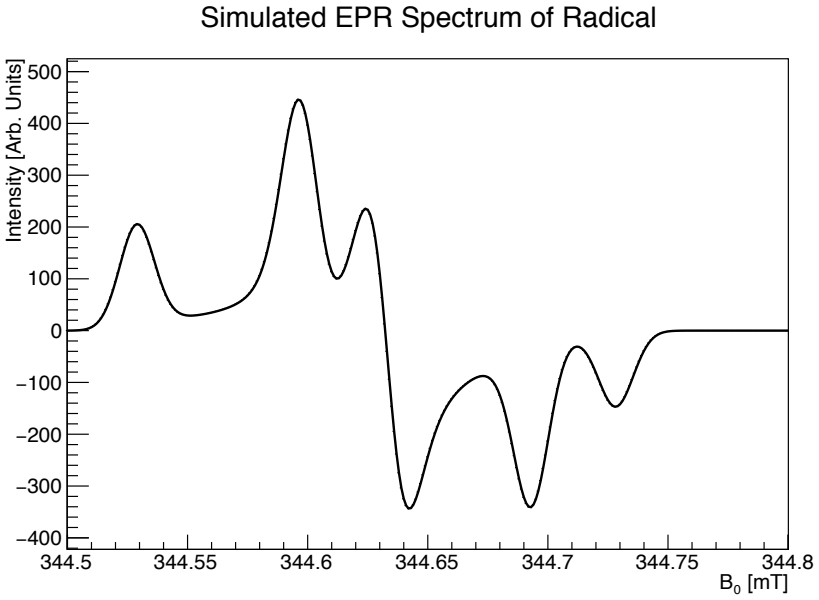

FIGURE 6.7: Simulated EPR spectrum of radical from a damaged PolySty model with two hydrogen atoms removed which include hyperfine parameters.

Chapter 7

Discussion

7.1 Experimental Results Discussion

7.1.1 Discolouration Following Irradiation

The discolouration in irradiated plastic scintillators is generally associated to the formation of colour centres. Colour centres are briefly discussed in Section 3.6.2. Two types of colour centres are said to exists, namely, the permanent and the annealable [121] and are the likely cause of the discolouration. The most common radicals formed during irradiation are associated with the annealable colour centres were cyclohexadienyl- and benzyl-like radicals. Once the samples are exposed to air, these short-lived radicals react with oxygen, and they, along with their colour centres no longer exist. This annealing emerges as a lightening of the irradiated spot was observed for all samples irradiated to 0.8 MGy.

The oxygen-exposed radicals that form are peroxy intermediate radicals and, if exposure is continued, hydroperoxides [122], as shown in Figure 3.9. These long-lived radicals and their associated permanent colour centres emerge as a persistent discolouration of irradiated

spot. All samples irradiated to a target dose of 2.5 MGy and above displayed a permanent discolouration.

7.1.2 Spectral Shape

Previous investigations have hypothesised that the triplet state observed in irradiated plastics is due to a hyperfine coupling arising from an electron coupling to a phenyl group containing two equivalent protons [123]. These radicals are hypothesised to form from the breaking of a $C-H$ bond with a π-orbital structure. Their detected unpaired electrons are usually delocalised in this orbital [124]. The resulting EPR spectrum consists of three peaks each with a width between 17 G to 45 G [89]. However, several of the EPR spectra observed contain more than three peaks [96]. The differences in shape (such as number of peaks, peak intensities, and peak resolution) are mainly attributed to the sensitivity and resolution of the EPR spectrometer [92], and how long after irradiation the EPR spectrum is taken. This implies that many radiation-induced radicals responsible for additional peaks are short-lived. In order to observe this multi-peaked EPR spectrum, it is suggested that samples be irradiated within the cavity of the EPR spectrometer while measurements are taken.

Clearly, the EPR spectra observed in this investigation do not contain multiple peaks. The spectral shape in this investigation, and in previous work [125], has been observed in hydrogen atom bombarded and γ-irradiated PS [68, 92]. Notably, these samples were stored for several weeks after irradiation in an oxygen environment. It should also be noted that EPR spectrometer parameters may change the shape of the observed spectrum considerably. In particular, at low power saturation, the shoulders in each spectrum obtained from irradiated (from both γ-irradiation and hydrogen bombardment) PS become more distinct [123]. Furthermore, it is hypothesised that poor resolution of the EPR spectrometer could account for the lack of clearly observable hyperfine peaks in any of the spectra.

Thus, based on the shape observed in this investigation, no conclusions can be drawn regarding the short-lived radicals that form during irradiation. Instead, an attempt is made to understand the complex, secondary peak formation that could result from stable radicals which collectively contribute to the broad shoulder. The poor resolution of these peaks is attributed to both the resolution of the spectrometer used and the random orientation of each molecule in the sample. The **g**-tensor anisotropy could account of the long tail-like feature on each integrated EPR spectrum.

Regardless of dose, the secondary peak appears at a different g-factor, g_a, compared to the central peak in most of the spectra. This implies the molecular orbital on the unpaired electron contains a π-orbital which reflects the asymmetry of its surrounding environment [68] in the radical formed. The most probable stable radicals which could account for this peak are the peroxy-type radicals [126]. Their g-factors are generally larger [94] than those of the main peak's and are in the range observed in this investigation. The absolute difference between the two g-factor values ($|g - g_a|$) is on average of the order of 10^{-4}. This difference further motivates a larger degree of orbital angular momentum [68] of the trapped unpaired electron within a peroxy-type radical. Since this second peak is observed in most of the un-irradiated spectra, one possible interpretation is that the sample preparation could cause bonds to break resulting in EPR signals that mimic those of irradiated samples.

7.1.3 Normalised Intensity Increase

In standard EPR spectroscopy techniques, the "paramagnetic spin concentration" of a sample is calculated by finding the area under the doubly integrated EPR spectrum and dividing by the volume of the sample [127]. Attempts to use this technique yielded questionable paramagnetic spin concentration values with an order of magnitude 10^{10} lower than those seen in literature. Therefore, a more cautious approach was taken by investigating a normalised intensity. This parameter gives an indication of the number of detected spins per unit volume. An increase in intensity in the EPR signal has been observed in irradiated polymers which is likely to be proportional to the dose absorbed [93, 95]. Indeed, increasing dose has been shown to be proportional to the number of radicals produced in irradiated plastics [68] and, ultimately, the number of unpaired electrons.

The largest relative increase in the normalised intensities in Figure 6.4 is the Dubna sample closely followed by the EJ208 sample. This implies that there is little difference between the two polymer bases. Based on the assumption that this is related to the number of formed radicals in the system, increasing dose in both PVT and PS samples increases the number of free radicals detected.

7.1.4 Decrease in g-factor

An EPR spectral shift has been observed in UV-irradiated solid PS citing a lower g-factor [96] for the central peak with an increase in dose. Furthermore, an interpretation of the spectral shift is that formed radicals in irradiated plastics give rise to local magnetic fields [89]. The unpaired electrons experience an effective magnetic field as they are shielded by these local magnetic fields. With an increase in damaged incurred by the plastics, the magnitude of the effect these local magnetic fields increases. This interpretation is in agreement with effect of chemical shifts discussed in Section 4.2.3. In this investigation, it is hypothesised that change in the magnetic environment of the plastics due to the radiation damage inherently effects the SO coupling which is known to cause variations in the value of the g-factor. A change in the local magnetic environment of the unpaired electrons also alters their SO coupling as orbital angular momentum becomes quenched [124, 128] and a decrease [129] in g-factor is observed. The quenching of orbital angular momentum suggests that there is a lower bound for the value of the g-factor for a given sample as dose increases. This possibly explains the asymptotic nature of the g-factor as a function of dose in Figure 6.2. Based on this hypothesis, the orbital angular momentum of unpaired electrons in EJ200 are quenched the most, and those of the Bicron sample quenched the least with more absorbed dose. However, these two samples are similar in their chemical composition (see Section 5.2) suggesting that this has no effect on the rate of decrease as a function of dose. The relative g-factor shifts shown in Figure 6.2 have been presented in previous work [130].

However, similar studies have shown no deviation in the g-factor as dose is increased [92, 131]. This implies that the deviation is either too small to be detected, or that it results from factors not encountered in other studies. No attempt at an explanation has been given as to why a deviation, or lack thereof, exists in damaged samples of similar chemical composition. Similar conclusions have been presented in studies on disordered carbon-based systems where a large decrease in g-factor had been observed in one doped compound and not the other [132]. Therefore, no concrete conclusion can be made as to why this shift exists in some studies and not others.

7.1.5 Peak-to-peak Variation

When compared to carbon based compounds, un-irradiated polymers displayed a relatively broader EPR spectrum. This has been attributed to the unpaired electron possibly coupling

to nitrogen from exposure to air [133]. This comes as a result of unresolved hyperfine interactions between the unpaired electron and nucleus of the nitrogen [134] observed in the EPR spectrum.

The general decrease in ΔB_{PP} for PS samples and general increase in ΔB_{PP} for PVT samples may indicate that the structural differences between the two polymer bases influence the variation of this parameter with an increase in dose. In a study conducted on various irradiated polymers, a decrease in ΔB_{PP} was observed for all polymer types as dose is increased [135]. This decrease was hypothesised to be as a result of an increase in unpaired electrons detected from a large number of C = C systems found in a polyenthyl radical. The increase in C = C bond formation is consistent with dehydrogenation (see Section 3.6.2).

On the other hand, the increase in ΔB_{PP} is possibly due the detection of different radicals formed at various doses. Two different radicals have been observed [136, 137] in irradiated polymers at different doses. The first radical occurs at low doses (in the kGy region) as a result of main chain scission (see Section 3.6.1). It's spin concentration decreases as dose increases. The second radical occurs at a much higher dose and it's spin concentrations increase with increasing dose. A possible explanation for the broadening of line spectra could be that unpaired electrons couple to a large number of protons found in the second radical.

Of course, dehydrogenation and main chain scission are not mutually exclusive and are common features observed in both irradiated PVT and PS based polymers [65]. Results presented in Figure 6.3 do seem to indicate that the PVT based samples (EJ200, EJ208, EJ280, and Bicron) are more susceptible to main chain scission, and the PS based samples (Dubna and Protvino) are more susceptible to dehydrogenation when irradiated with protons. Finally, it is possible that these two competing features may cause no change in ΔB_{PP}. This has been noted by comparing the spectra of un-irradiated thin film polymers to irradiated ones polymers [133].

7.1.6 Summary

Each feature of the EPR spectrum analysed from the un-irradiated and irradiated samples present a number of possible stable radials that are detected. The discolouration and g-factors of these spectra indicate that possible stable peroxy-like radicals are formed in the plastic. Through, dehydrogenation, it is possible that these radicals further form ketones and quintones. The normalised intensity analysis indicates that increasing dose results in an

increase in the number of these radicals and, subsequently, unpaired electrons. The broad features of these spectra indicate a possibility of nitrogen reacting to the radicals in the samples which couple to the unpaired electrons. Finally, the ΔB_{PP} analysis indicates the presence of an polyenthyl radical in PS and, studying this analysis in PVT, that radicals are dose dependent.

It is, therefore, hypothesised that the number of possible radicals detected, along with their interaction with the unpaired electrons, leads to the complex EPR spectra observed.

7.2 Computational EPR Discussion

In an attempt to replicate the general experimental spectra of irradiated plastics, the computationally simulated spectra shown in Figure 6.5 display similar features. These include an increase in intensity with an increase in damage, and the formation of a shoulder structure at lower magnetic fields. The inclusion of additional unpaired electrons during simulations is justified by the chemical potential calculations. It indicates that, as in the real plastics, the magnetic signatures of additional unpaired electrons result in the single lined EPR spectra which includes a shoulder. This EPR spectra has been observed in irradiated plastics exposed to oxygen and allowed to recover (see Section 7.1.2). One interpretation of the EPR spectra in Figure 6.5 is that the single peak forms as a result of unpaired electrons in a local environment similar to that of un-irradiated plastics, and that the shoulder arises from radicals experiencing a local environment in a damaged region. No deviation in either the position of the spectra (g-factors) or the ΔB_{PP} with an increase in the number of hydrogen atoms removed is consistent with previous studies discussed in Sections 7.1.4 and 7.1.5, respectively. One stark difference between the experimental and computational spectra is that the radical forming the shoulder is not a peroxy-type radical since the damaged models contain no oxygen. The identity of these radicals lies in their spectral features.

The three peak EPR spectrum shown in Figure 6.6a has been experimentally observed [89] and the intensity ratios of 1:2:1 and g-factors can be interpreted as an unpaired electron coupling to two equivalent protons. The line spacing of the peaks also suggests that the protons could reside within a $-CH_2-$ fragment [68]. The addition of the hyperfine principle values resulted in a five peak spectrum. A similar spectrum has been observed experimentally [68] and has been attributed to a number of of alkyl radicals and fragments of these radicals. It is possible that the larger damaged MUKLAF and PolSty models contain more than one radical after

the removal of the hydrogen atoms since their simulated EPR spectra were observed to be almost identical. Thus, the magnetic signatures arising from the number of possible radicals and radical fragments may result in the observed spectra. These radicals could include those mentioned at the end of Section 3.6.1.

A computational investigation of a γ-irradiated model [138] similar to the Styrene and Vinyl toy models yielded a four peak spectrum at random orientations. These peaks were identified as coming from a contribution of various stable alkyl radicals, which suggests that the damage in smaller models may indeed depend on which site the hydrogen atom is removed. This is further motivated by the observed variations in the EPR peak intensities and spacings from models where hydrogen atoms were removed from various sites. In all four models, the similarities in the simulated five peak EPR spectra of the radicals suggests that the magnetic environments of these different alkyl radicals are similar.

7.3 Future Work

Further work could include an investigation into radical formation in both PS and PVT scintillators that are irradiated in the EPR spectrometer. This experimental set up would require a γ-ray source producing γ-rays incident on the plastics which are, in turn, situated in the EPR spectrometer. In order to observe possible hyperfine peaks resulting from this set up, an EPR spectrometer with a better resolution than the spectrometer employed in the current investigation is required. Further work pertaining to the computational studies could include an investigation on damaged models that include oxygen. These models could yield insights into peroxy-type radicals through their simulated EPR spectra.

Chapter 8

Conclusion

In light of the replacement of plastic scintillators situated in the TileCal and minimum bias trigger regions as part of the Phase II upgrade in 2018, the following conclusion can be drawn from the results and discussion in Chapters 6 and 7, respectively. Using electron paramagnetic resonance (EPR) spectroscopy, this work investigates radical formation in irradiated plastic scintillators as a function of dose. In addition to this, a computational DFT approach investigated the EPR signatures of computational pristine and damaged styrene and vinyl toluene models, and larger polystyrene-like models.

The experimental irradiated samples of approximately 250 μm thickness were subjected to increasing doses of 6 MeV proton induced radiation damage. These were compared to un-irradiation samples of the same thickness using EPR spectroscopy. The target doses were set to 0.8 MGy, 2.5 MGy, 8.0 MGy, 25.0 MGy, 50.0 MGy, and 80.0 MGy. The iThemba LABS, Gauteng tandem accelerator provided the 6 MeV protons. Damage to the computational models was induced by the removal of hydrogen atoms. To replicate increasing damage, one, two, and then three hydrogen atoms were removed from the molecules and the damaged structures were allowed to computationally relax.

In the experimental investigation, the extent of the damage incurred by each scintillator was proportional to the dose it absorbed. A discolouration of the plastics intensified with larger

absorbed doses; however, a slight fading was noted in all the 0.8 MGy samples. Samples were analysed using EPR spectroscopy two weeks after their irradiation to ensure the investigation studied permanent damage of the plastics. The discolouration observed in all plastics is likely to be caused by permanent and annealable colour centres associated with the different radicals. The short-lived cyclohexadienyl- and benzyl-like radicals associated to annealable colour centres exists only before being exposed to oxygen. After the irradiated plastics were exposed to oxygen, the lightening, or recovery, of the plastic suggests that only the stable, long-lived radicals, along with their permanent colour centres persisted in the plastic. These oxygen-exposed radicals were identified by their g-factors using the EPR analysis to be an unpaired electron trapped in a number of stable peroxy-type radicals.

A further analysis of the experimental EPR parameters provided further insights into the possible structural changes within the plastics. The general increase in normalised intensity observed in both PS and PVT based plastics suggests that there is an increase in the number of radicals and unpaired electrons as dose increases. The general decrease in the relative g-factors as a function of dose suggest that unpaired electrons experience an increased effective magnetic field as a function of dose, and this investigation suggests that this is inherently linked to an asymptotic decrease in the g-factor as a result of quenching of orbital angular momentum.

The ΔB_{PP} slight decrease indicates that, in the PS irradiated sample, the number of unpaired electrons increase. These electrons arise from a system of C = C bonds found in a polyenthyl radical. This suggests that the predominant form of damage in PS is as a result of dehydrogenation. The increase in ΔB_{PP} observed in PVT samples suggests the presence of two radicals that form as a result of main chain scission. Main chain scission is as a result of hydrogen gas formation. Thus, the analysis of the ΔB_{PP} suggests that the PS and PVT samples are susceptible to different mechanisms of damage.

It should be noted that no concrete evidence is provided by the analysis of the experimental EPR parameters to suggest that one particular sample, or base of plastic, out performs another when subjected to proton induced radiation damage. The comparative EPR analysis conducted on various irradiated plastics proved inconclusive in identifying the plastic scintillator least susceptible to proton-induced radiation damage. Furthermore, the analysis could not aid in suggesting a type of plastic scintillator most suited for the replacement of those plastic scintillators situated in the TileCal and minimum bias trigger regions.

The computational EPR analysis of the chemical potential results suggest that electron transfer between pristine and damage structures is possible. Based on these results and the assumption that the number of electrons increases or decreases with each hydrogen atom removed, the computational EPR spectral mimicked that of those observed experimental. The EPR spectral shape of the pristine models yielded a single smooth EPR peak. The sharp peak resulted from an unpaired electron which experience a local environment similar to that of an un-damaged real plastic. However, in the case of the damaged models, the EPR signals showed the formation of a shoulder which results from the addition on an of unpaired electron. This electron is likely to experience a local environment similar to that of an unpaired electron in a damaged region.

An investigation into the radical responsible for the shoulder, without hyperfine interactions, yielded a three peak spectra of intensity ratio 1:2:1. This signature is likely to be as a result of coupling from an electron to two equivalent protons residing in a $-CH_2-$ fragment. Addition of the hyperfine interactions indicated signatures from multiple alkyl-type radicals. This interpretation was consistent for the larger MUKLAF and PolySty models. The observations seen because damage to the smaller Styrene and Vinyl toluene models indicated the presence of various alkyl radicals depending on the site from which the hydrogen atom was removed.

Future work would include an investigation into radical formation where samples are irradiated in the EPR spectrometer, and a computational EPR investigation could study damaged samples that include oxygen.

Bibliography

[1] Lakowicz, J. R., *Principles of Fluorescence Spectroscopy.* Springer, 3rd ed., March, 2006.

[2] Vasil'chenko, V. G. *et al.*, "New results on radiation damage studies of plastic scintillators," *Nucl. Instr. and Meth. in Phys. Res. A* **369** no. 1, (1996) 55–61.

[3] Aad, G. *et al.*, "Observation of a new particle in the search for the Standard Model Higgs boson with the ATLAS detector at the LHC," *Phys. Lett. B* **716** no. 1, (2012) 1 – 29.

[4] Chatrchyan, S. *et al.*, "Observation of a new boson at a mass of 125 GeV with the CMS experiment at the LHC," *Phys. Lett. B* **716** no. 1, (2012) 30 – 61.

[5] Peskin, M. E. and Schroeder, D. V., *An Introduction to Quantum Field Theory.* Westview Press, 1st ed., 1995.

[6] Aad, G. *et al.*, "Measurements of fiducial and differential cross sections for Higgs boson production in the diphoton decay channel at $\sqrt{s} = 8$ TeV with ATLAS," *J. High Energy Phys.* **2014** no. 9, (2014) 112.

[7] Aad, G. *et al.*, "Search for the associated production of the Higgs boson with a top quark pair in multilepton final states with the ATLAS detector," *Phys. Lett. B* **749** (2015) 519 – 541.

[8] Khachatryan, V. *et al.*, "Search for a Higgs boson in the mass range from 145 to 1000 GeV decaying to a pair of W or Z bosons," *J. High Energy Phys.* **2015** no. 10, (2015) 144.

[9] von Buddenbrock, S. *et al.*, "Phenomenological signatures of additional scalar bosons at the LHC," *Eur. Phys. J. C* **76** no. 10, (2016) 580.

[10] The ATLAS Collaboration, *Search for new phenomena in events with missing transverse momentum and a Higgs boson decaying to two photons in p p collisions at* $\sqrt{s}$ *= 13 TeV with the ATLAS detector.* No. ATLAS-CONF-2016-011. Geneva.

[11] Shiltsev, V. D., "High-energy particle colliders: past 20 years, next 20 years, and beyond," *Phys. Usp* **55** no. 10, (2012) 965.

[12] The ATLAS Collaboration, *ATLAS Tile Calorimeter: Technical Design Report.* No. ATLAS-TDR-3 in Technical Design Report ATLAS. CERN, Geneva, 1996.

[13] Kwee, R. E., *Minimum Bias Trigger in ATLAS.* No. ATL-DAQ-PROC-2010-055. Geneva, Dec, 2010.

[14] Evans, D. and Crook, M. A., "Irradiation of plastics: Damage and gas evolution," *MRS Bull.* **22** (Apr, 1997) 36–40.

[15] Zorn, C., "A pedestrian's guide to radiation damage in plastic scintillators," *Radiat. Phys. Chem.* **41** no. 1, (1993) 37 – 43.

[16] Jivan, H. *et al.*, "Radiation hardness of plastic scintillators for the Tile Calorimeter of the ATLAS detector," *J. Phys. Conf. Ser.* **623** (Jun, 2015) 12–16.

[17] The ATLAS Collaboration, "The ATLAS Experiment at the CERN Large Hadron Collider," *J. Instrum.* **3** no. 08, (2008) S08003.

[18] The ATLAS Collaboration, *ATLAS detector and physics performance: Technical Design Report, 1.* No. ATLAS-TDR-14 in Technical Design Report ATLAS. CERN, Geneva, 1999.

[19] The ATLAS Collaboration, *ATLAS Inner Detector: Technical Design Report, 1.* No. ATLAS-TDR-4 in Technical Design Report ATLAS. CERN, Geneva, 1997.

[20] Solovyanov, O., "Performance of the ATLAS Tile Hadronic Calorimeter at LHC in Run 1 and planned upgrades," *J. Instrum.* **9** no. 10, (2014) C10006.

[21] Henriques, A., "The ATLAS tile calorimeter," in *2015 4th International Conference on Advancements in Nuclear Instrumentation Measurement Methods and their Applications (ANIMMA)*, pp. 1–7. IEEE, April, 2015.

[22] Collins, P. D. B. and Martin, A. D., "Hadron reaction mechanisms," *Rep. Prog. Phys.* **45** no. 4, (1982) 335.

[23] The ATLAS Collaboration, *Expected performance of the ATLAS experiment: detector, trigger and physics.* No. CERN-OPEN-2008-020. CERN, Geneva, 2009.

[24] Leyton, M. and Siegrist, J., *Minimum Bias Measurements with the ATLAS Detector at the CERN Large Hadron Collider.* PhD thesis, UC, Berkeley, Berkeley, 2009.

[25] Kwee, R. E., *Development and Deployment of an Inner Detector Minimum Bias Trigger and Analysis of Minimum Bias Data of the ATLAS Experiment at the Large Hadron Collider*. PhD thesis, Humboldt-Universität zu Berlin, Berlin, 2012.

[26] Zeitnitz, C. and Gabriel, T. A., "The GEANT-CALOR interface and benchmark calculations of ZEUS test calorimeters," *Nucl. Instr. Meth. Phys. Res. A* **349** no. 1, (1994) 106 – 111.

[27] Ferrari, A. and Sala, P. R. and Fassó, A. and Ranft, J., *FLUKA: A multi-particle transport code (program version 2005)*. No. CERN-2005-010. CERN, Geneva, 2005.

[28] Amorim, A. and Henriques, A. and Maio, A., *Study of the effect of the radiation on a TILECAL hadron calorimeter intended to be used in the ATLAS Experimental on the Barrel region*. No. ATL-CAL-93-021. Geneva, Jun, 1993.

[29] Sidoti, A., "Minimum Bias Trigger Scintillators in ATLAS Run II," *J. Instrum.* **9** no. 10, (2014) C10020.

[30] Schram, E., *Organic Scintillator Detectors*. Elsevier, Brussels, 1st ed., 1963.

[31] Olive, K. A., "Review of Particle Physics," *Chinese Phys. C* **38** no. 9, (Aug, 2014) 090001.

[32] Markley, F. and Woods, D. and Pla-Dalmau, A. and Foster, G., "Development of radiation hard scintillators," *Radiat. Phys. Chem.* **41** no. 1, (1993) 135–152.

[33] Leo, W. R., *Techniques for Nuclear and Particle Physics Experiments*. Springer, Heidelberg, Germany, 2nd ed., 1994.

[34] Attix, F. H., *Introduction to Radiological Physics and Radiation Dosimetry*. Wiley-VCH Verlag GmbH, Weinheim, Germany, 1st ed., Nov, 1986.

[35] Tavernier, S., "Interactions of Particles in Matter," in *Experimental Techniques in Nuclear and Particle Physics*, ch. 2, pp. 23–53. Springer, Berlin, Heidelberg, 2009.

[36] McKenna, A. J. and Trevethan, T. and Latham, C. D. and Young, P. J. and Heggie, H. I., "Threshold displacement energy and damage function in graphite from molecular dynamics," *Carbon* **99** (2016) 71 – 78.

[37] Kinchin, G. H. and Pease, R. S., "The displacement of atoms in solids by radiation," *Rep. Prog. Phys.* **18** no. 1, (1955) 1.

[38] Bethe, H., "Zur Theorie des Durchgangs schneller Korpuskularstrahlen durch Materie," *Ann. Phys.* **397** no. 3, (1930) 325–400.

[39] Bragg, W. H. and Kleeman, R., "XXXIX. On the α particles of radium, and their loss of range in passing through various atoms and molecules," *Philos. Mag.* **10** no. 57, (1905) 318–340.

[40] Fink, D., "Mechanism of Particle-Polymer Interaction," in *Fundamentals of Ion-Irradiated Polymers*, ch. 4, pp. 131–134. Springer, Berlin, Heidelberg, 2004.

[41] Both, G. and Krotz, R. and Lohmer, K. and Neuwirth, W., "Density dependence of stopping cross sections measured in liquid ethane," *Phys. Rev. A* **28** (Dec, 1983) 3212–3216.

[42] Ziegler, J. F. and Ziegler, M.D. and Biersack, J.P., "SRIM – The stopping and range of ions in matter (2010)," *Nucl. Instr. and Meth. in Phys. Res. B* **268** no. 11-12, (Jun, 2010) 1818–1823.

[43] Porter, L. E. and Naylor, H. and Duder, J. C., "Stopping power of polystyrene for 2.2 to 5.9 MeV protons," *Nucl. Instr. Meth.* **155** no. 1-2, (Sep, 1978) 25–28.

[44] Bednyakov, A. A. and Bulgakov, Y. V. and Nikolaev, V. S. and Chernov, V. L., "Energy losses and their straggling of H+ and He+ ions of several hundred keV energy after passing through metal and polystyrene films," *JETP* **51** no. 5, (1980) 954.

[45] Bednyakov, A. A., and Bulgakov, Y. V. and Nikolaev, V. S. and Chernov, V. L., "Energy straggling of hydrogen and helium ions in Al, C, and polystyrene at energies of tens and hundreds keV per nucleon," *Phys. Status Solidi A* **68** no. 1, (1981) 187–192.

[46] Wallace, W. E. and Rothman, J. B. and Composto, R. J., "The stopping power of 1 to 3 MeV hydrogen and helium in polystyrene," *Nucl. Instr. and Meth. in Phys. Res. B* **84** no. 1, (1994) 1–4.

[47] Ziegler, J. F. and Biersack, J. P., and Littmark, U., *The Stopping and Ranges of Ions in Matter*. Pergamon, 1st ed., 1985.

[48] Bichsel, H., "Straggling in thin silicon detectors," *Rev. Mod. Phys.* **60** no. 3, (1988) 663.

[49] Brooks, F. D., "Organic scintillators," *Prog. Nucl. Phys.* **5** (1956) 252.

[50] Knoll, G. F., *Radiation Detection and Measurement*. Wiley, New York, 4th ed., 2010.

[51] Sauer, M. and Hofkens, J. and Enderlein, J., *Handbook of Fluorescence Spectroscopy and Imaging*. Wiley-VCH Verlag GmbH & Co. KGaA, Weinheim, Germany, 1st ed., Jan, 2011.

[52] Carrington, A. and McLachlan, A. D., *Introduction to Magnetic Resonance: with Applications to Chemistry and Chemical Physics*. Harper and Row, 1st ed., 1967.

[53] Lower, S. K. and El-Sayed, M. A., "The Triplet State and Molecular Electronic Processes in Organic Molecules," *Chem. Rev.* **66** no. 2, (1966) 199–241.

[54] Smith, D. W., "The Antibonding Effect," *J. Chem. Educ.* **77** no. 6, (Jun, 2000) 780.

[55] Hegde, S. G. and Liu, F. and Chang, G. and Sitaraman, S. K., "Optical loss changes in siloxane polymer waveguides during thermal curing," *J. Appl. Polym. Sci.* **106** no. 4, (Nov, 2007) 2320–2327.

[56] Moser, S. W. and Harder, W. F. and Hurlbut, C. R. and Kusner, M. R., "Principles and practice of plastic scintillator design," *Radiat. Phys. Chem.* **41** no. 1-2, (1993) 31–36.

[57] Helms, V., *Principles of Computational Cell Biology*. Wiley-Blackwell, Weinheim, Germany, 1st ed., 2008.

[58] Groom, D. E. and Aguillar-Benitez, M. and Amsler, C., "Review of particle physics Particle data group," *Eur. Phys. J. C* **15** no. 1-4, (2000) 1–878.

[59] Kapłon, Ł. *et al.*, "Plastic scintillators for positron emission tomography obtained by the bulk polymerization method," *BAMS* **10** no. 1, (2015) 27–31.

[60] Swank, R. K. and Buck, W. L., "The Scintillation Process in Plastic Solid Solutions," *Phys. Rev.* **91** no. 4, (Aug, 1953) 927–933.

[61] Mapelli, A., *Scintillation Particle Detectors Based on Plastic Optical Fibres and Microfluidics*. PhD thesis, École Polytechnique Fédérale de Lausanne, 2011.

[62] van Dykeand, K. and Woodfork, K., "Instrumentation for the Measurement of Luminescence," in *Luminescence Biotechnology: Instruments and Applications*, ch. 2, pp. 31–40. CRC Press LLC, New York, 2002.

[63] Chapiro, A., "Radiation chemistry of polymers," *Radiat. Res.* **4** (1964) 179–191.

[64] Torrisi, L., "Radiation damage in PVT (Polyvinyltoluene) induced by energetic ions," *Radiat. Eff. Defects Solids* **145** no. 4, (1998) 271–284.

[65] Dole, M. and Parkinson, W. and Keyser, R., "Polystyrene and Related Polymers," in *The Radiation Chemistry of Macromolecules*, ch. 5, pp. 57–96. Elsevier, 1973.

[66] Torrisi, L., "Radiation damage in polyvinyltoluene (PVT)," *Radiat. Phys. Chem.* **63** no. 1, (Jan, 2002) 89–92.

[67] Dole, M., "Polymers That Primarily Degrade on Irradiation," in *The Radiation Chemistry of Macromolecules*, ch. 6, pp. 97–117. Elsevier, 1973.

[68] Claybourn, M. and Gray, H. and Murphy, D. M. and Purnell, I. J. and Rowlands, C. C., "Electron magnetic resonance study of gamma-irradiated poly (lactide-co-glycolide) microspheres," *J. Control. Release* **91** (2003) 431–438.

[69] Alger, M., "Polymer science dictionary," *Polym. Int.* **24** (1991) 127.

[70] Charlesby, A., "Swelling properties of polystyrene crosslinked by high energy radiation," *J. Polym. Sci.* **11** no. 6, (1953) 521–529.

[71] Chapiro, A., "Chemical modifications in irradiated polymers," *Nucl. Instr. and Meth. in Phys. Res. B* **32** no. 1, (1988) 111 – 114.

[72] Coffey, T. and Urquhart, S. G. and Ade, H., "Characterization of the effects of soft X-ray irradiation on polymers," *J. Electron. Spectrosc. Relat. Phenom.* **122** no. 1, (2002) 65 – 78.

[73] Lawton, E. J. and Balwit, J. S. and Powell, R. S., "Paramagnetic Resonance Studies of Irradiated High Density Polyethylene. II. Effect of Irradiation Dose on the Radical Species Trapped at Room Temperature," *J. Chem. Phys.* **33** no. 2, (1960) 405–412.

[74] Zhu, R., "Radiation damage in scintillating crystals," *Nucl. Instr. and Meth. in Phys. Res. A* **413** no. 2, (1998) 297–311.

[75] Hamada, M. M. and Rela, P. R. and da Costa, E. and de Mesquita, C., "Radiation damage studies on the optical and mechanical properties of plastic scintillators," *Nucl. Instr. Meth. Phys. Res. A* **422** no. 1–3, (1999) 148 – 154.

[76] Zhao L. *et al.*, "Properties of plastic scintillators after irradiation ," *Nucl. Instr. and Meth. in Phys. Res. A* **552** no. 3, (2005) 449 – 455.

[77] Bross, A. D. and Pla-Dalmau, A., "Radiation-induced hidden-absorption effects in polystyrene-based plastic scintillators," in *Radiation Effects on Polymers*, ch. 38, pp. 578–590.

[78] Gunder, O. A. and Voronkina, N. I. and Barashkov, N. N. and Milinchuk, V. K. and Jdanov, G. S., "Factors determining radiation stability of plastic scintillators," *Radiat. Phys. Chem.* **46** no. 1, (1995) 115 – 117.

[79] Franks, L. A., "Oxygen bleaching of gamma-radiation-induced optical absorption bands in polystyrene," *J. Polym. Sci. Part B* **2** no. 6, (1964) 581–584.

[80] Sears, W. C. and Parkinson, W. W., "Post-irradiation oxidation in rubber and plastics," *J. Polym. Sci.* **21** no. 98, (1956) 325–326.

[81] Wick, K. and Paul, D. and Schröder, P. and Stieber, V. and Bicken, B., "Recovery and dose rate dependence of radiation damage in scintillators, wavelength shifters and light guides," *Nucl. Instr. Meth. Phys. Res. B* **61** no. 4, (1991) 472 – 486.

[82] Bohr, N., "On the constitution of atoms and molecules," in *Niels Bohr, 1913-2013: Poincaré Seminar 2013*, pp. 13–33. Springer International Publishing, 2016.

[83] Weil, J. and Bolton, J., *Electron Paramagnetic Resonance: Elementary Theory and Practical Applications*. John Wiley & Sons, Inc., Hoboken, New Jersey, 2nd ed., 2007.

[84] Blundell, S. and Thouless, D., "Magnetism in Condensed Matter," *Am. J. Phys.* **71** no. 1, (2003) 94–95.

[85] Slichter, C. P., *Principles of Magnetic Resonance*. Springer Berlin Heidelberg, 1st ed., 1990.

[86] Odom, B. and Hanneke, D. and D'Urso, B. and Gabrielse, G., "New measurement of the electron magnetic moment using a one-electron quantum cyclotron," *Phys. Rev. Lett.* **97** (Jul, 2006) 030801.

[87] Bloch, F., "Nuclear induction," *Phys. Rev.* **70** (Oct, 1946) 460–474.

[88] Junk, M. J. N., *Assessing the Functional Structure of Molecular Transporters by EPR Spectroscopy*. Springer Berlin Heidelberg, 1st ed., 2012.

[89] Schneider, E. E., "Paramagnetic resonance in X-irradiated plastics and in plastic solutions of free radicals," *Discuss. Faraday Soc.* **19** (1955) 158–165.

[90] Bullock, A. T. and Cameron, G. G. and Smith, P. M., "Electron spin resonance studies of spin-labeled polymers. IV. Slow-motional effects in solid polystyrene," *J. Polym. Sci., Polym. Phys. Ed.* **11** no. 7, (1973) 1263–1269.

[91] Bushell, J. A. and Claybourn, M. and Williams H. E. and Murphy, D. M., "An EPR and ENDOR study of γ- and β-radiation sterilization in poly (lactide-co-glycolide) polymers and microspheres," *J. Control. Release* **110** no. 1, (2005) 49 – 57.

[92] Ingalls, R. B. and Wall, Leo A., "Electron Spin Resonance Spectra of Free Radical Intermediates Formed by Reaction of Polystyrene with Atoms of Hydrogen and Deuterium," *J. Chem. Phys.* **35** no. 1, (1961) 370–371.

[93] Whiffen, D. H., "The application of electron spin resonance to polymer studies," *Macromol. Chem. Phys.* **34** no. 1, (1959) 170–178.

[94] Fischer, H., "Magnetic Properties of Free Radicals," in *Landolt-Börnstein Group II Molecules and Radicals*, p. 154. Springer Berlin Heidelberg, 1965.

[95] Lin, C. and Ming, L. and Lee, C., "EPR kinetics in irradiated syndiotactic polystyrene at elevated temperatures," *Polym.* **49** no. 18, (2008) 3987 – 3992.

[96] Cozzens, R. F. and Moniz, W. B. and Fox, R. B., "Electron Spin Resonance Study of the Photolysis of Polystyrene and Poly(α-Methylstyrene)," *J. Chem. Phys.* **48** no. 2, (1968) 581–585.

[97] Martin, R. M., *Electronic Structure: Basic Theory and Practical Methods*. Cambridge University Press, 1st ed., 2004.

[98] Born, M. and Oppenheimer, J. R., "Zur quantentheorie der molekeln," *Ann. Phys.* **389** no. 20, (1927) 457–484.

[99] Kohn, W. and Sham, L. J., "Self-consistent equations including exchange and correlation effects," *Phys. Rev.* **140** (Nov, 1965) A1133–A1138.

[100] Charpentier, T., "The PAW/GIPAW approach for computing NMR parameters: A new dimension added to NMR study of solids," *Solid State Nucl. Magn. Reson.* **40** no. 1, (2011) 1 – 20.

[101] Yates, J. R. and Pickard, C. J., "Computations of Magnetic Resonance Parameters for Crystalline Systems: Principles," in *eMagRes*. John Wiley and Sons, Ltd, 2007.

[102] Monkhorst, H. J. and Pack, J. D., "Special points for Brillouin-zone integrations," *Phys. Rev. B* **13** (Jun, 1976) 5188–5192.

[103] Gregor, T. and Mauri, F. and Car, R., "A comparison of methods for the calculation of NMR chemical shifts," *J. Chem. Phys.* **111** no. 5, (1999) 1815–1822.

[104] Blöchl, P. E., "Projector augmented-wave method," *Phys. Rev. B* **50** (Dec, 1994) 17953–17979.

[105] Pickard, C. J. and Mauri, F., "All-electron magnetic response with pseudopotentials: Nmr chemical shifts," *Phys. Rev. B* **63** (May, 2001) 245101.

[106] Yates, J. R. and Pickard, C. J. and Mauri, F., "Calculation of NMR chemical shifts for extended systems using ultrasoft pseudopotentials," *Phys. Rev. B* **76** no. 2, (2007) 1–11.

[107] Kaupp, M. and Bühl, M. and Malkin, V. G., *Calculation of NMR and EPR Parameters: Theory and Applications*. Wiley-VCH Verlag GmbH, 1st ed., 2004.

[108] Van de Walle, C. G. and Blöchl, P. E., "First-principles calculations of hyperfine parameters," *Phys. Rev. B* **47** (Feb, 1993) 4244–4255.

[109] Pickard, C. J. and Mauri, F., "First-Principles Theory of the EPR g-Tensor in Solids: Defects in Quartz," *Phys. Rev. Lett.* **88** (Feb, 2002) 086403.

[110] Levy, M., "Universal variational functionals of electron densities, first-order density matrices, and natural spin-orbitals and solution of the v-representability problem," *Natl. Acad. Sci.* **76** no. 12, (1979) 6062–6065.

[111] Perdew, J. P. and Parr, R. G. and Levy, M. and Balduz, J. L., "Density-Functional Theory for Fractional Particle Number: Derivative Discontinuities of the Energy," *Phys. Rev. Lett.* **49** (Dec, 1982) 1691–1694.

[112] Liao, S. *et al.*, "A comparative study of the radiation hardness of plastic scintillators for the upgrade of the Tile Calorimeter of the ATLAS detector," *J. Phys. Conf. Ser.* **645** no. 1, (2015) 012021.

[113] Hagen, W. R., *Biomolecular EPR Spectroscopy*. CRC Press, 1st ed., 2008.

[114] Fourme, R. and Andre, D. and Bosio, L. and Jasse, B., "Crystal and molecular structure of syndiotactic 2,4,6-triphenylheptane, a polystyrene model molecule," *J. Mol. Struct.* **71** (1981) 245 – 252.

[115] Andre, D. and Bosio, L. and Jasse, B., "Crystal and molecular structures of syndiotactic 2,4,6-8-tetraphenylnonane, a polystyrene model molecule," *J. Mol. Struct.* **140** no. 3–4, (1986) 339 – 345.

[116] Kresse, G. and Joubert, D. P., "From ultrasoft pseudopotentials to the projector augmented-wave method," *Phys. Rev. B* **59** (Jan, 1999) 1758–1775.

[117] Perdew, J. P. and Burke, K. and Ernzerhof, M., "Generalized Gradient Approximation Made Simple," *Phys. Rev. Lett.* **77** (Oct, 1996) 3865–3868.

[118] Giannozzi, P. *et al.*, "QUANTUM ESPRESSO: a modular and open-source software project for quantum simulations of materials," *J. Phys. Condens. Matter* **21** no. 39, (2009) 395502.

[119] Troullier, N. and Martins, J. L., "Efficient pseudopotentials for plane-wave calculations," *Phys. Rev. B* **43** (Jan, 1991) 1993–2006.

[120] Stoll, S. and Schweiger, A., "EasySpin, a comprehensive software package for spectral simulation and analysis in EPR," *J. Magn. Reson.* **178** no. 1, (2006) 42 – 55.

[121] Clough, R. L. and Malone, G. M. and Gillen, K. T. and Wallace, J. S. and Sinclair, M. B., "Discoloration and subsequent recovery of optical polymers exposed to ionizing radiation," *Polym. Degrad. Stab.* **49** no. 2, (1995) 305 – 313.

[122] Wallace, J. S. and Sinclair, M. B. and Gillen, K. T. and Clough, R. L., "Color center annealing in gamma - irradiated polystyrene, under vacuum and air atmospheres," *Radiat. Phys. Chem.* **41** no. 1, (1993) 85 – 100.

[123] Florin, R. E. and Wall, L. A. and Brown, D. W., "Free radicals in gamma-irradiated polystyrenes," *Trans. Faraday Soc.* **56** (1960) 1304–1310.

[124] Morton, J. R., "Electron Spin Resonance Spectra of Oriented Radicals," *Chem. Rev.* **64** no. 4, (Aug, 1964) 453–471.

[125] Pelwan, C. D. *et al.*, "Characterization of plastic scintillators using magnetic resonance techniques for the upgrade of the Tile Calorimeter in the ATLAS detector," *J. Phys. Conf. Ser.* **645** no. 1, (2015) 012023.

[126] Sevilla, M. D. and Becker, D. and Yan, M., "Structure and reactivity of peroxyl and sulphoxyl radicals from measurement of oxygen-17 hyperfine couplings: relationship with taft substituent parameters," *J. Chem. Soc. Faraday Trans.* **86** (1990) 3279–3286.

[127] Barklie, R. C., "Characterisation of defects in amorphous carbon by electron paramagnetic resonance," *Diamond Relat. Mater.* **12** no. 8, (Aug, 2003) 1427–1434.

[128] McConnell, H. M. and Robertson, R. E., "Spectroscopic Splitting Factors in Aromatic Radicals," *J. Phys. Chem. A* **61** no. 7, (1957) 1018–1018.

[129] Stone, A. J., "g factors of aromatic free radicals," *Mol. Phys.* **6** no. 5, (1963) 509–515.

[130] Pelwan, C. D. *et al.*, in *The Proceedings of The 60th Annual Conference of The South African Institute of Physics (SAIP2015)*, No. 60, pp. 222–225. The South African Institute of Physics (SAIP), 2015.

[131] Libby, D. and Ormerod, M. G. and Charlesby, A., "Electron spin resonance spectra of some polymers irradiated at 77 K," *Polym.* **1** no. 1, (Jan, 1960) 212–218.

[132] Mardis, K. L. and Webb, J. N. and Holloway, T. and Niklas, J. and Poluektov, O. G., "Electronic Structure of Fullerene Acceptors in Organic Bulk-Heterojunctions: A Combined EPR and DFT Study," *J. Phys. Chem. Lett.* **6** no. 23, (2015) 4730–4735.

[133] George, M. A. and Ramakrishna, B. L. and Glausinger, W. S., "Electron paramagnetic resonance investigation of free radicals in polyimide films," *J. Phys. Chem.* **94** no. 12, (1990) 5159–5164.

[134] Lewis, I. C. and Singer, L. S., "Electron spin resonance study of the reaction of aromatic hydrocarbons with oxygen," *J. Phys. Chem.* **85** no. 4, (1981) 354–360.

[135] Ohnishi, S. and Ikeda, Y. and Sugimoto, S. and Nitta, I., "On the ESR singlet spectra frequently observed in irradiated polymers at a large dose," *J. Polym. Sci. A Polym. Chem.* **47** no. 149, (1960) 503–507.

[136] Peng, J. S. and Ming, L. and Lin, Y. and Lee, S., "EPR study of radical annihilation kinetics of gamma-ray-irradiated acrylic (PMMA) at elevated temperatures," *Polym.* **52** no. 26, (2011) 6090 – 6096.

[137] Lin, Y. and Lee, S. and Lin, B. C. and Cheng, C. P., "EPR studies of high dose gamma-irradiated poly(methyl methacrylate)," *Mater. Chem. Phys.* **78** no. 3, (2003) 847 – 851.

[138] Tasdemir, H. and Sayin, U. and Türkkan, E. and Ozmen, A., "EPR investigation of gamma irradiated single crystal guaifenesin: A combined experimental and computational study," *Radiat. Phys. Chem.* **121** (2016) 61 – 68.

[139] Perdew, J. P. and Burke, K. and Ernzerhof, M., "Generalized Gradient Approximation Made Simple," *Phys. Rev. Lett.* **77** (Oct, 1996) 3865–3868.

[140] Alwall, J. *et al.*, "Madgraph/madevent v4: the new web generation," *J. High Energy Phys.* **2007** no. 9, (2007) 28.

[141] Sjöstrand, T. and Mrenna, S. and Skands, P., "A brief introduction to PYTHIA 8.1," *Comput. Phys. Commun.* **178** no. 11, (2008) 852 – 867.

[142] ATLAS Collaboration, *Measurements of the photon identification efficiency with the ATLAS detector using 4.9 fb^{-1} of pp collision data collected in 2011.* No. ATLAS-CONF-2012-123. Geneva, Aug, 2016.

[143] ATLAS Collaboration, *Expected performance of missing transverse momentum reconstruction for the ATLAS detector at $\sqrt{s} = 13$ TeV.* No. ATL-PHYS-PUB-2015-023. Jul, 2015.

[144] Aad, G. *et al.*, "Performance of missing transverse momentum reconstruction in proton-proton collisions at $\sqrt{s} = 7$ TeV with ATLAS," *Eur. Phys. J. C* **72** no. 1, (2012) 1844.

Appendix A

Analysis of Experimental Parameters

A.1 Integrated EPR Spectra Fits

Each EPR spectrum in Figure 6.1 was integrated and fit with a triple Gaussian distribution which is the addition of three Gaussian distributions. This distribution takes the form

$$\begin{aligned} G(x, N, \mu_1, \sigma_1, \mu_2, \sigma_2, \mu_3, \sigma_3) =& N \{ f_1 e^{-(x-\mu_1)^2/2\sigma_1^2} + f_2 e^{-(x-\mu_2)^2/2\sigma_2^2} \\ &+ (1 - f_1 - f_2) e^{-(x-\mu_3)^2/2\sigma_3^2} \}, \end{aligned} \tag{A.1}$$

where μ_1, μ_2, μ_3 and σ_1, σ_2, σ_3 represent the three means and standard deviations of the Gaussians, respectively, N is the normalisation factor, and f_1 and f_2 are two fractions.

This fit was not chosen for any physical reason, but rather for its shape and range of parameters which could be changed in order to fit the varying forms of the EPR spectra. Each fit was manually adjusted to achieve the lowest χ^2 value[1].

The key parameters obtained from these fits, which were used in the investigation, where the means μ_1 and μ_2. These needed in order to calculate the g-factors and differences between peaks. The fits for each sample and dose are presented below along with the values of the parameters in Equation A.1.

[1] A statistical hypothesis test constructed from the sum of the difference between observed and expected values all squared divided by the observed values. This test is often referred to as the goodness-of-fit test.

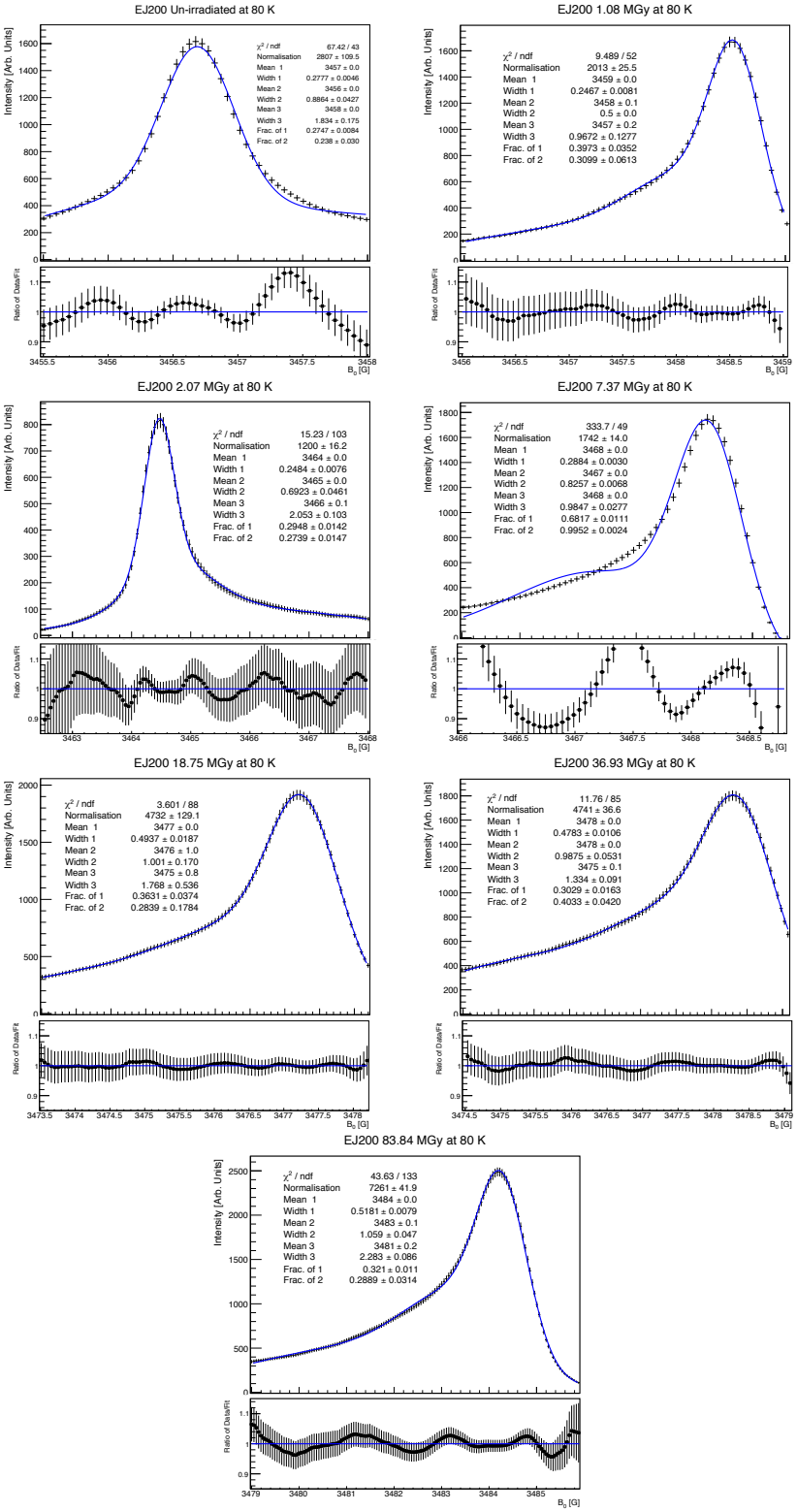

FIGURE A.1: Triple Gaussian fits for all EJ200 samples at 80 K. Misfits to spectra can be attributed to the low number of data points around the central peak. However, increasing bin size resulted in skewed fit.

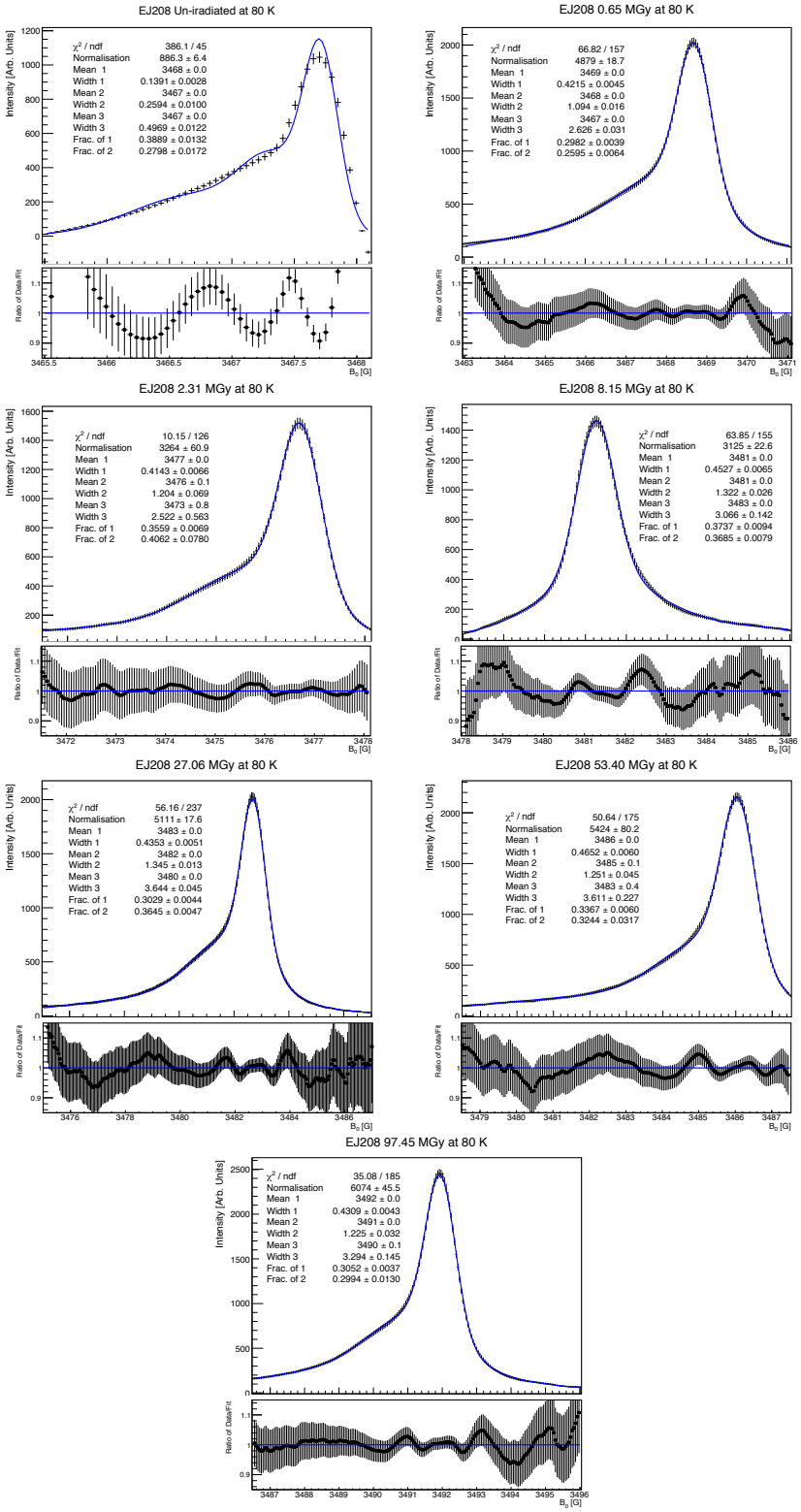

FIGURE A.2: Triple Gaussian fits for all EJ208 samples at 80 K.

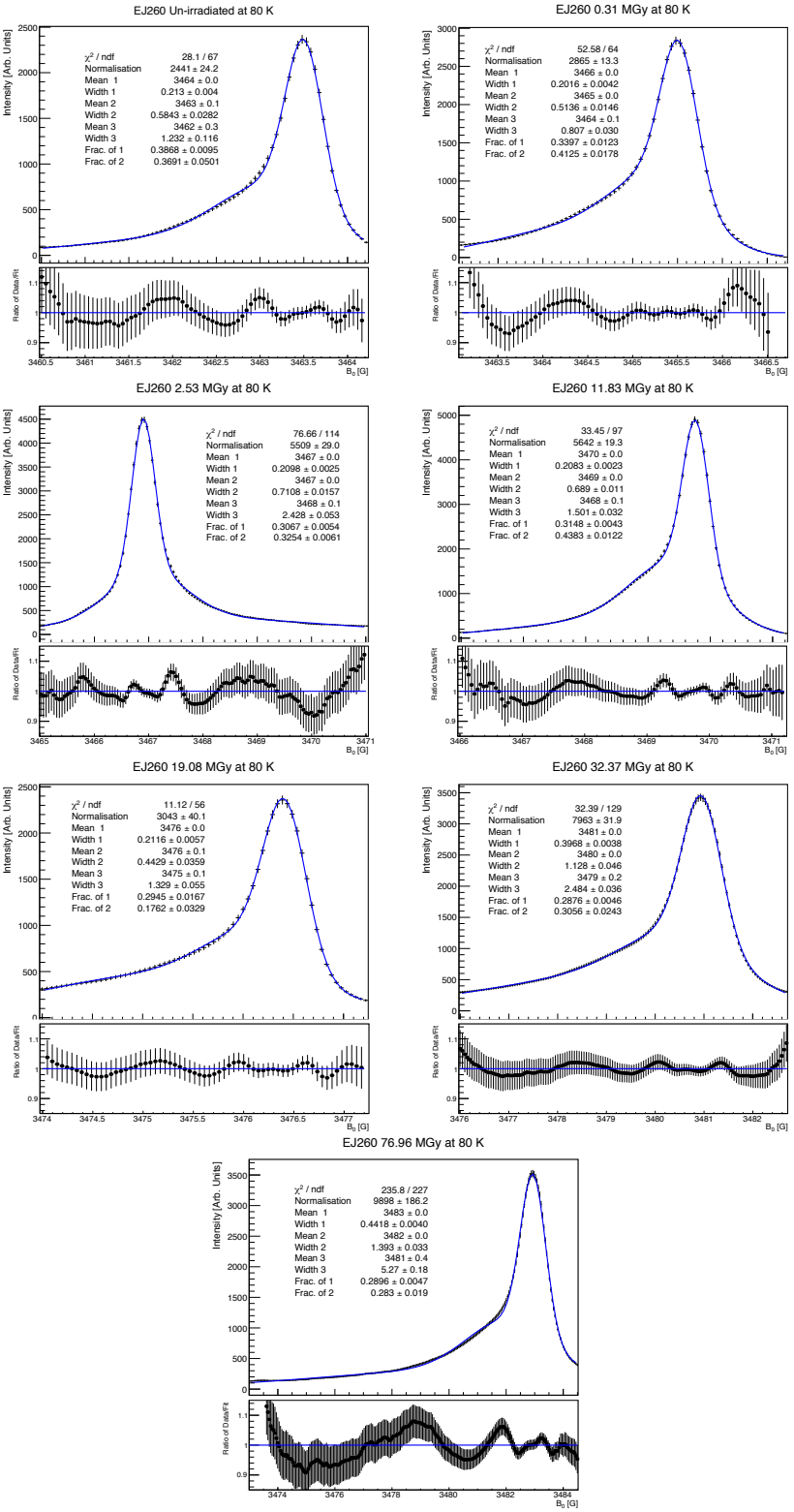

FIGURE A.3: Triple Gaussian fits for all EJ260 samples at 80 K.

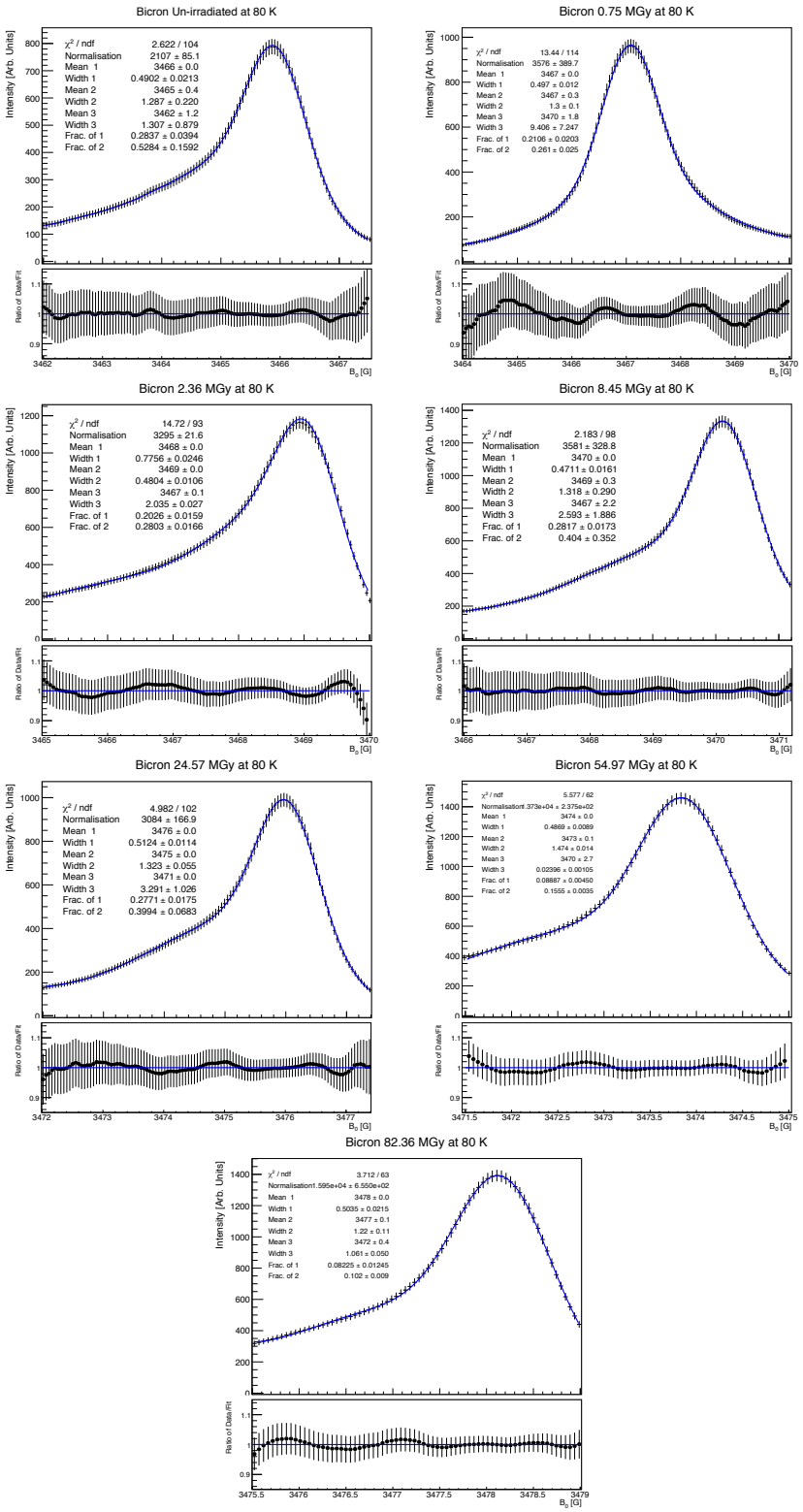

FIGURE A.4: Triple Gaussian fits for all Bicron samples at 80 K.

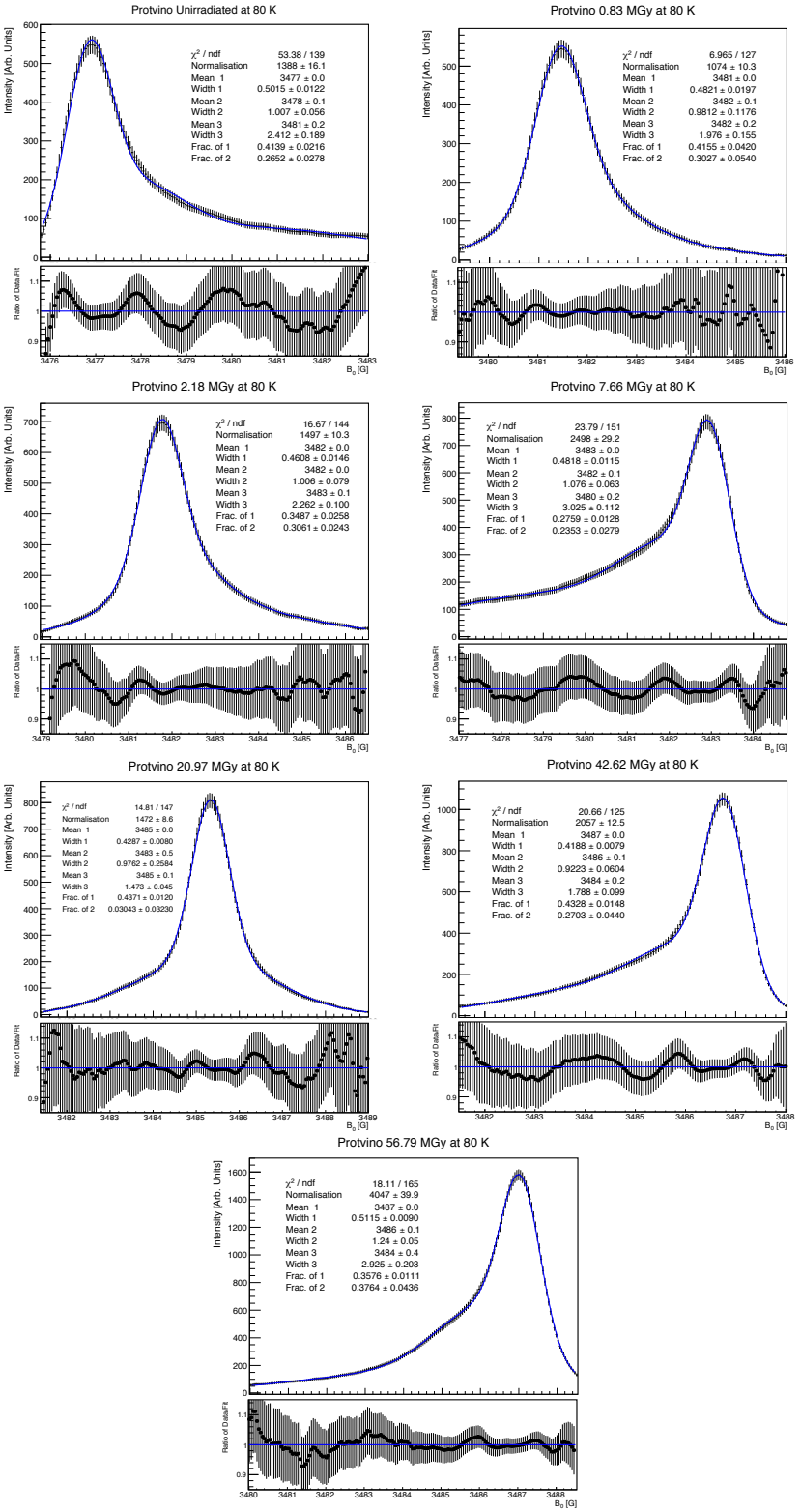

FIGURE A.5: Triple Gaussian fits for all Protvino samples at 80 K.

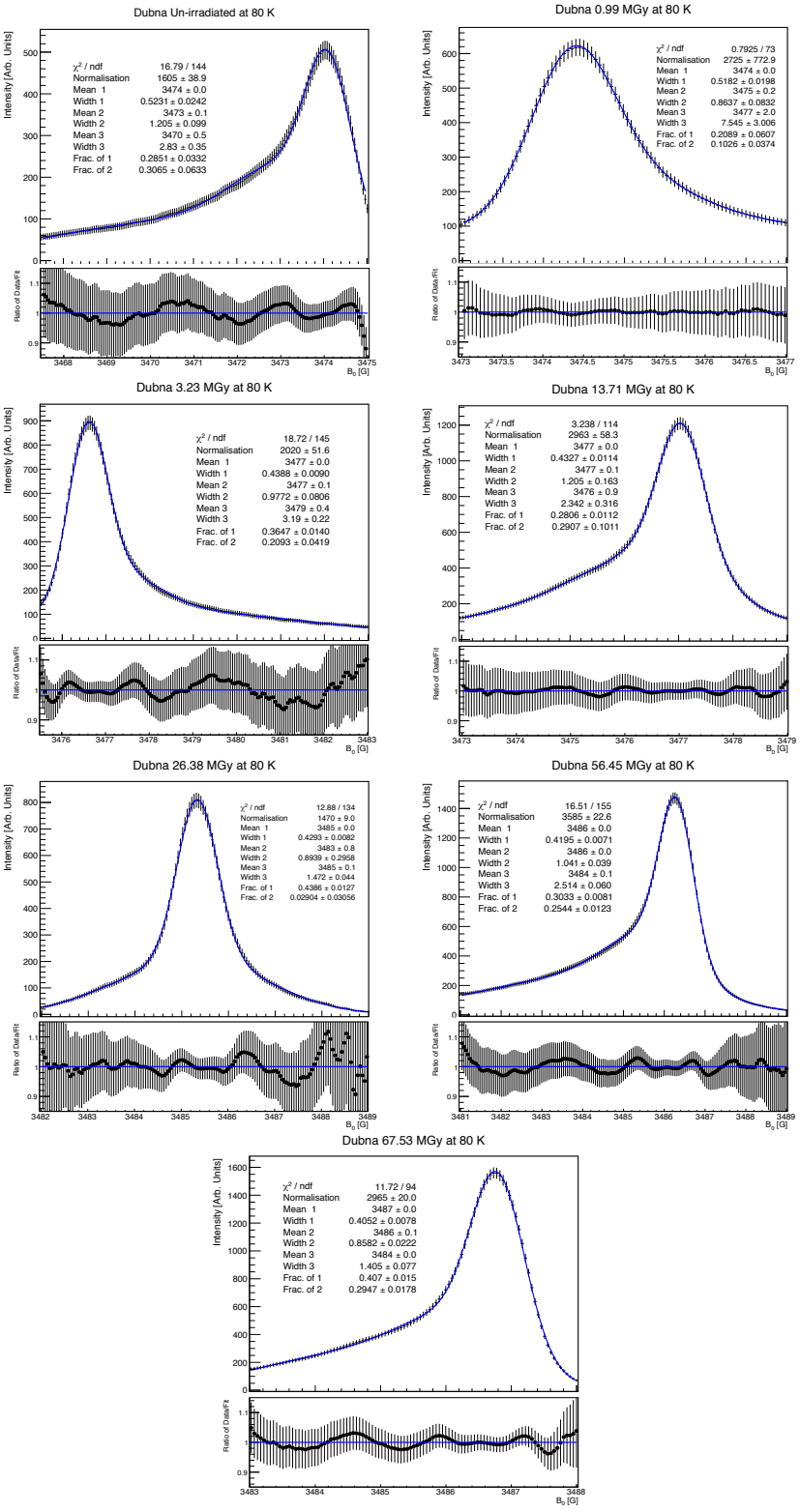

FIGURE A.6: Triple Gaussian fits for all Dubna samples at 80 K.

A.2 Integrated Current Analysis

In order to irradiate each sample to its target dose, an estimate time of irradiation was set. In most cases, the sample was irradiated for a short period of time to gauge the beam current measured from the feed connected to the carousel. Then, using this value, the time of irradiation was calculated by solving for t in Equation 5.1. Assuming the beam current remained constant, the sample was irradiated for the calculated time. The beam current distributions for each irradiated sample is shown in Section A.3.

Any fluctuations in the beam current resulted in a re-evaluation of the absorbed dose and, in some cases, longer irradiation time. Samples irradiated for a second time were kept in the carousel, under vacuum. These beam current distributions is shown in red (see Figures A.8). Factors contributing to beam fluctuation include the following: beam intensities and shapes incorrectly calibrated, parts of beam striking slits before reaching the sample, and (in the case of the 53.40 MGy EJ208 sample) loss of beam current due to a discharge in the tandem - this was due to components of the accelerator not being kept under vacuum.

Two errors resulting from beam fluctuations were calculated and used to calculate the errors associated in each absorbed dose calculation. The first of these was the statistical standard deviation from the initial estimation of beam current measurement. Since the integrated current was needed, the second error arose from finding the area under the curve using the trapezoidal rule. These two errors, along with instrumental and systematic errors were required to calculate the errors in the absorbed dose for each sample.

A.3 Key Parameter Values

Tables A.1 and A.2 represent the key parameter values for all un-irradiated and irradiated samples.

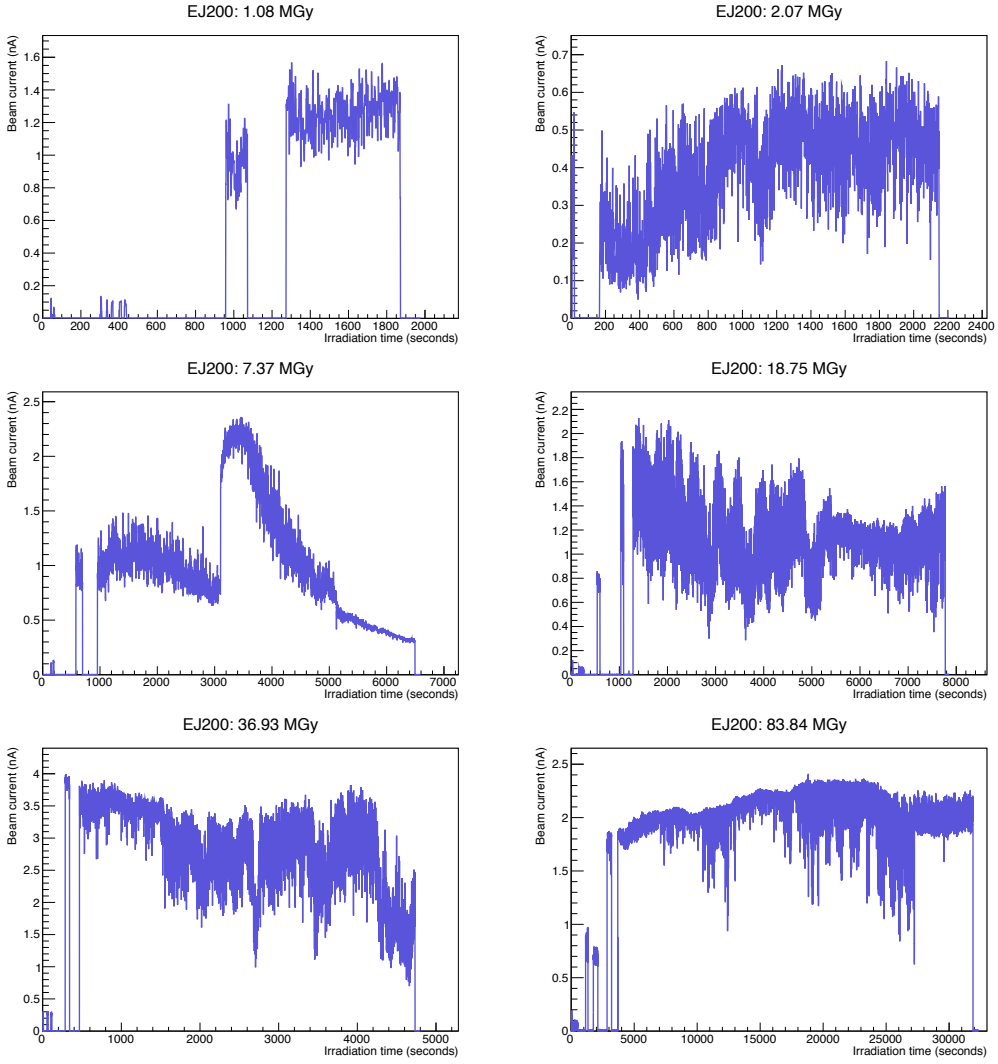

FIGURE A.7: Beam current for irradiated EJ200 samples.

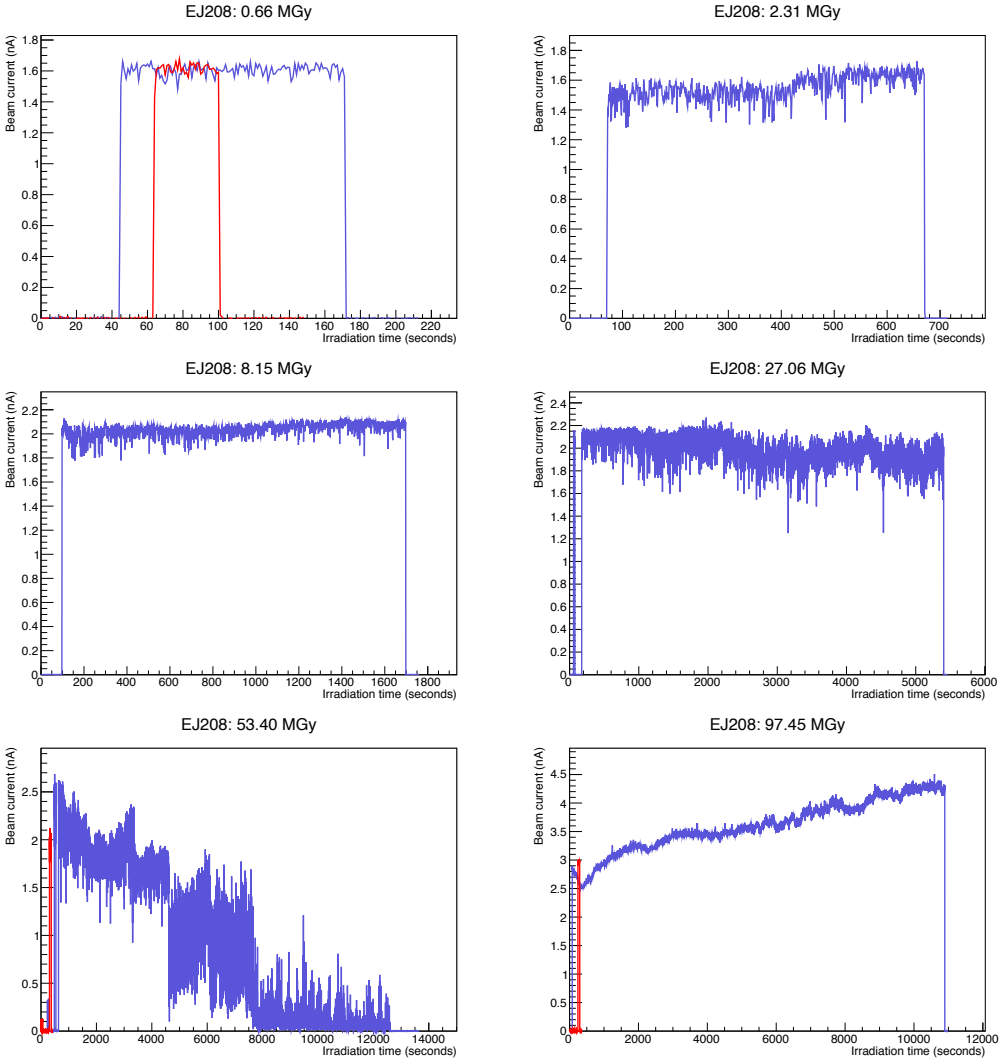

FIGURE A.8: Beam current for irradiated EJ208 samples.

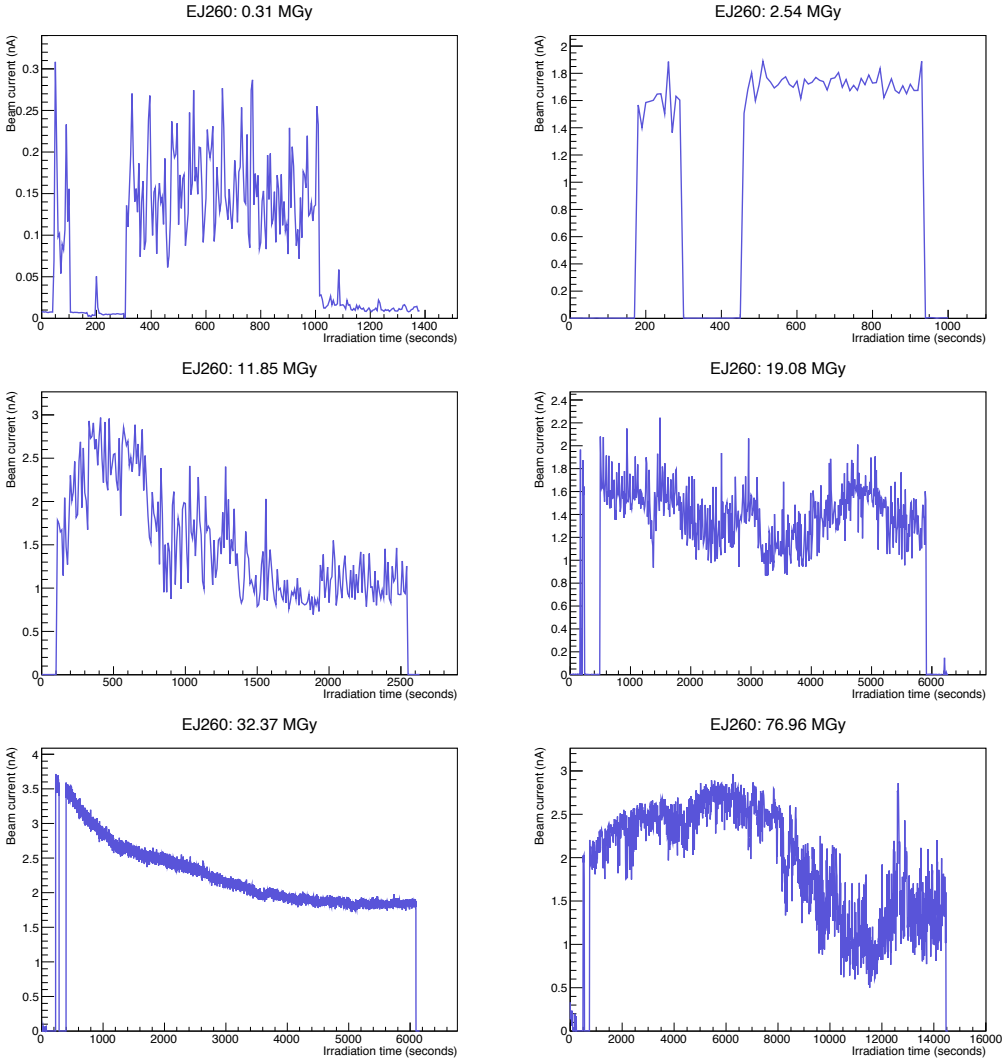

FIGURE A.9: Beam current for irradiated EJ260 samples.

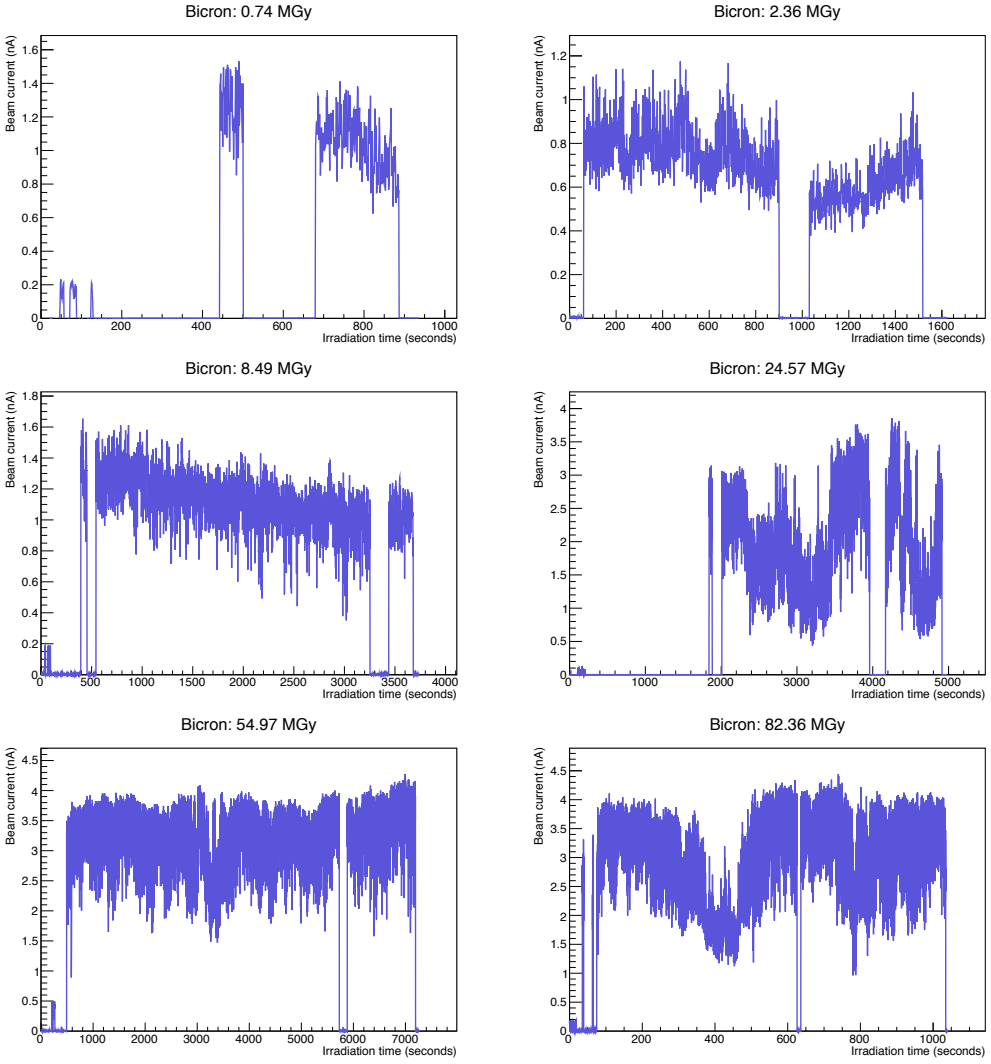

FIGURE A.10: Beam current for irradiated Bicron samples.

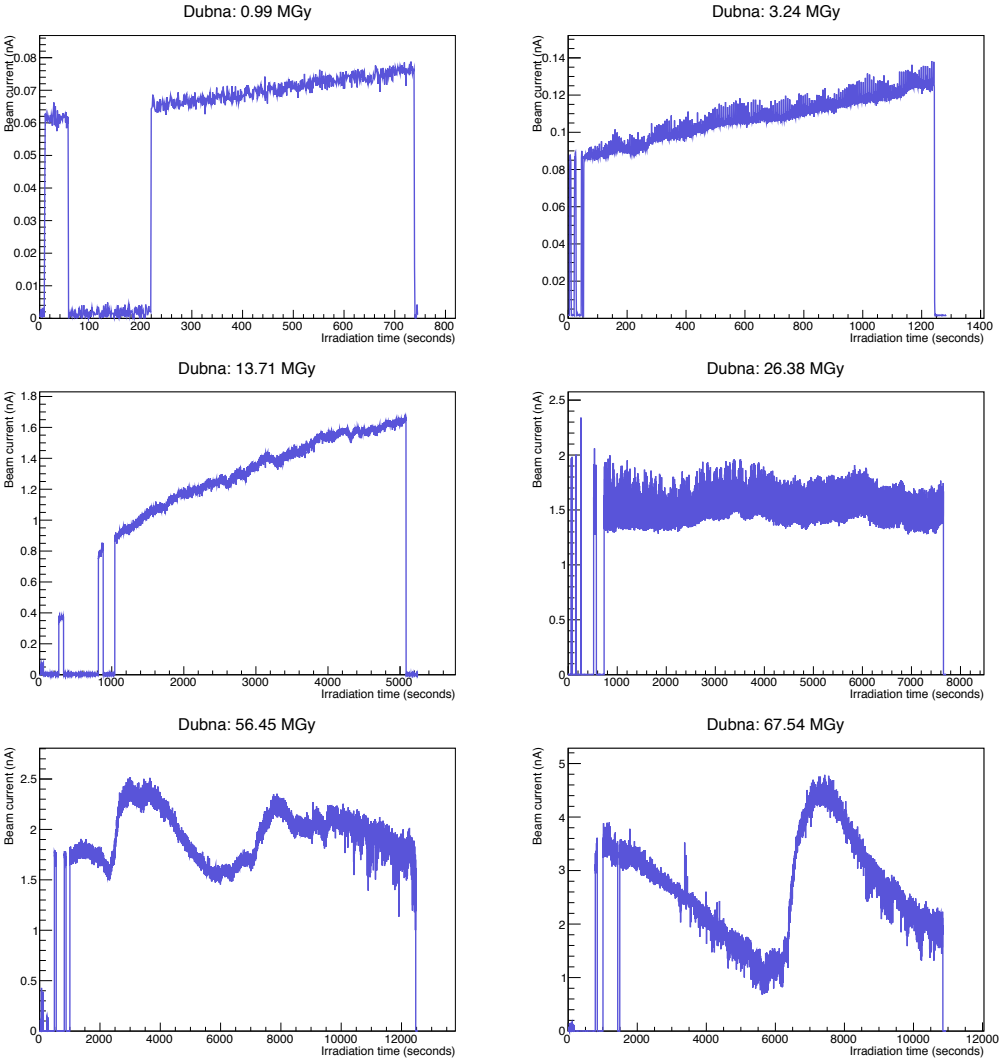

FIGURE A.11: Beam current for irradiated Dubna samples.

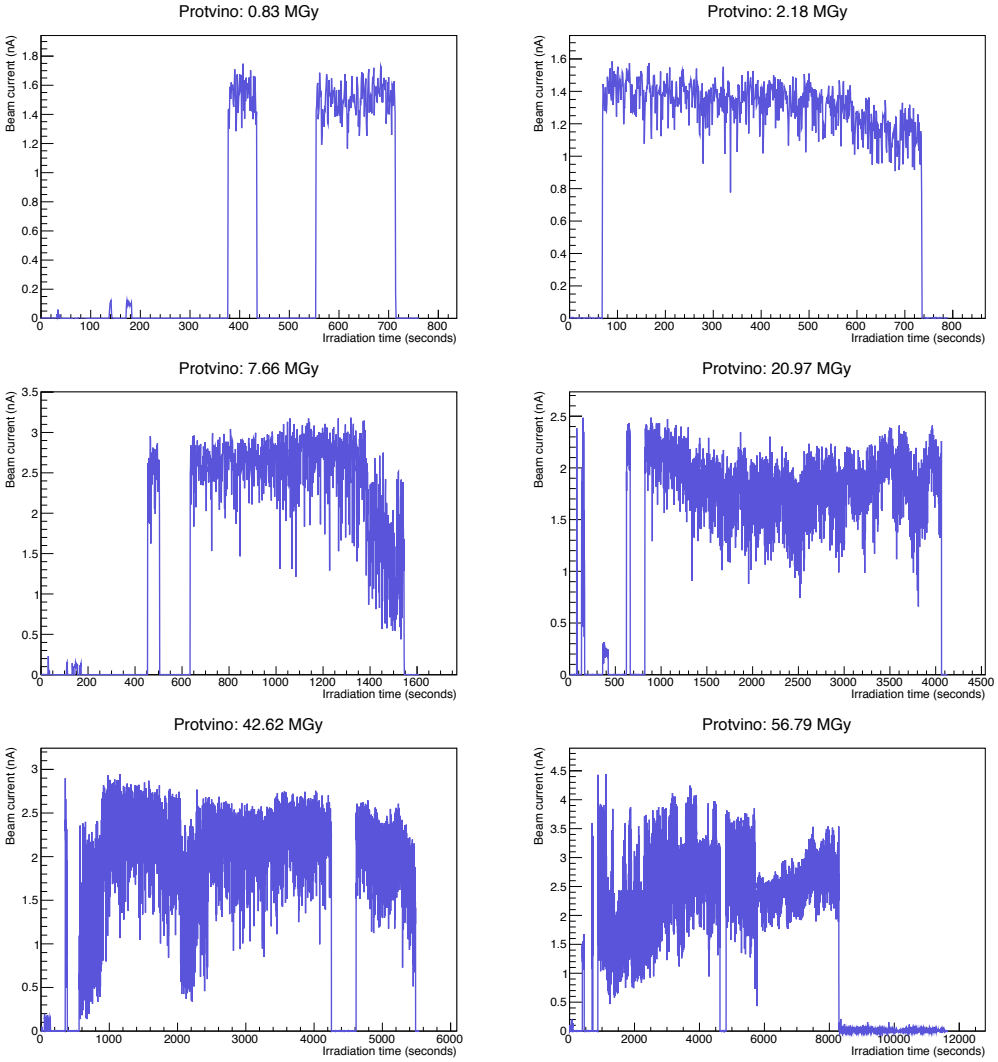

FIGURE A.12: Beam current for irradiated Protvino samples.

Sample	Abs. Dose (Gy)	Thickness (cm) ± 0.0005	B_0^* (G)	ν (MHz) ± 0.005	g-factor ± 1.6×10^{-4}	a-value (G)	g_a-factor** ± 1.7×10^{-4}	ΔB_{PP} (G) ± 0.007	Norm. Intens. (a.u./cm^3) ×10^6
EJ200	0.0	0.027	3456.69 ± 0.004	9.72	2.0091	0.49 ± 0.01	2.0094	0.49	1.85 ± 0.73
	1.08 ± 0.03	0.027	3458.54 ± 0.004	9.72	2.0080	0.49 ± 0.07	2.0083	0.54	1.91 ± 0.75
	2.07 ± 0.04	0.022	3464.47 ± 0.006	9.72	2.0046	-0.22 ± 0.03	2.0044	0.53	1.14 ± 0.45
	7.37 ± 0.17	0.028	3468.13 ± 0.003	9.72	2.0024	0.74 ± 0.01	2.0029	0.49	1.92 ± 0.76
	18.75 ± 1.63	0.026	3477.28 ± 0.010	9.72	1.997	0.79 ± 1.02	1.9976	0.94	2.27 ± 0.89
	36.93 ± 2.24	0.026	3478.40 ± 0.012	9.72	1.9965	0.80 ± 0.04	1.9970	1.15	2.14 ± 0.84
	83.84 ± 3.17	0.031	3484.28 ± 0.006	9.72	1.9932	1.01 ± 0.06	1.9937	1.16	2.48 ± 0.97
EJ208	0.0	0.031	3467.71 ± 0.005	9.72	2.0026	0.38 ± 0.02	2.0029	0.36	1.04 ± 0.41
	0.66 ± 0.01	0.025	3468.72 ± 0.005	9.72	2.0021	0.72 ± 0.01	2.0025	0.44	2.50 ± 0.98
	2.31 ± 0.45	0.023	3476.70 ± 0.005	9.72	1.9975	0.83 ± 0.06	1.9979	0.84	2.04 ± 0.80
	8.15 ± 0.89	0.022	3481.27 ± 0.005	9.72	1.9949	-0.02 ± 0.08	1.9949	1.01	2.05 ± 0.80
	27.05 ± 0.56	0.028	3482.70 ± 0.004	9.72	1.9941	0.87 ± 0.02	1.9946	0.80	2.24 ± 0.88
	53.40 ± 4.31	0.022	3486.06 ± 0.005	9.72	1.9921	0.88 ± 0.05	1.9926	0.89	3.03 ± 1.19
	97.45 ± 3.38	0.025	3491.95 ± 0.004	9.72	1.9899	0.81 ± 0.02	1.9892	0.88	3.03 ± 1.19
EJ260	0.0	0.030	3463.51 ± 0.002	9.72	2.0015	0.41 ± 0.09	2.0053	0.48	2.43 ± 0.96
	0.31 ± 0.05	0.026	3465.52 ± 0.002	9.72	2.0039	0.26 ± 0.02	2.0041	0.43	3.37 ± 1.32
	2.53 ± 0.14	0.027	3466.90 ± 0.002	9.72	2.0031	-0.08 ± 0.01	2.0031	0.47	5.13 ± 2.02
	11.85 ± 1.11	0.025	3469.77 ± 0.002	9.72	2.0015	0.35 ± 0.01	2.0017	0.38	6.06 ± 2.38
	19.08 ± 1.46	0.022	3476.42 ± 0.004	9.72	1.9977	0.39 ± 0.06	1.9979	0.43	3.31 ± 1.30
	32.37 ± 0.37	0.026	3480.95 ± 0.004	9.72	1.9951	0.45 ± 0.01	1.9953	0.90	4.07 ± 1.59
	76.96 ± 4.32	0.029	3482.95 ± 0.003	9.72	1.9939	0.97 ± 0.04	1.9945	0.91	3.75 ± 1.47

* Integrated EPR spectra maximum.
** This value pertains to the second peak formed on the shoulder of the integrated EPR spectrum.

TABLE A.1: Key parameter values for EJ200, EJ208, and EJ260.

Sample	Abs. Dose (Gy)	Thickness (cm) ± 0.0005	B_0^* (G)	ν (MHz) ± 0.005	g-factor ± 1.6×10^{-4}	a-value (G)	g_a-factor** ± 1.7×10^{-4}	ΔB_{PP} (G) ± 0.007	Norm. Intens. (a.u./cm^3) $\times10^6$
Bicron	0.0	0.026	3465.93 ± 0.012	9.72	2.0037	0.68 ± 0.42	2.0041	1.06	0.94 ± 0.37
	0.74 ± 0.05	0.026	3467.08 ± 0.007	9.72	2.0030	-0.12 ± 0.30	2.0030	1.05	1.14 ± 0.45
	2.36 ± 0.16	0.027	3468.29 ± 0.041	9.72	2.0023	-0.79 ± 0.04	2.0019	1.14	1.33 ± 0.52
	8.49 ± 0.49	0.025	3470.15 ± 0.011	9.72	2.0013	0.67 ± 0.27	2.0017	1.02	1.64 ± 0.65
	24.57 ± 1.74	0.022	3476.03 ± 0.008	9.72	1.9979	0.92 ± 0.04	1.9984	0.97	1.39 ± 0.55
	54.97 ± 3.43	0.024	3473.89 ± 0.007	9.72	1.9991	1.02 ± 0.05	1.9997	1.00	1.88 ± 0.74
	82.36 ± 5.69	0.023	3478.18 ± 0.016	9.72	1.9967	1.13 ± 0.15	1.9973	1.11	1.75 ± 0.69
Dubna	0.0	0.030	3474.11 ± 0.014	9.73	2.0010	1.03 ± 0.02	2.0016	1.07	0.52 ± 0.20
	0.99 ± 0.02	0.028	3474.35 ± 0.015	9.73	2.0009	-0.76 ± 0.16	2.0005	1.09	0.68 ± 0.27
	3.24 ± 0.07	0.025	3476.59 ± 0.008	9.73	1.9996	-0.62 ± 0.08	1.9993	0.86	1.10 ± 0.43
	13.71 ± 0.86	0.025	3477.06 ± 0.006	9.72	1.9973	0.47 ± 0.12	1.9976	0.88	1.49 ± 0.59
	26.38 ± 1.37	0.023	3485.34 ± 0.007	9.73	1.9946	2.26 ± 0.85	1.9959	0.94	1.08 ± 0.43
	56.45 ± 1.70	0.027	3486.29 ± 0.006	9.73	1.9941	0.67 ± 0.05	1.9944	0.91	1.68 ± 0.66
	67.54 ± 1.54	0.028	3486.80 ± 0.006	9.73	1.9938	0.63 ± 0.06	1.9941	0.92	1.72 ± 0.68
Protvino	0.0	0.024	3476.86 ± 0.010	9.73	1.9995	-1.09 ± 0.01	1.9989	1.07	0.70 ± 0.28
	0.83 ± 0.38	0.026	3481.43 ± 0.015	9.73	1.9968	-0.31 ± 0.10	1.9967	1.07	0.65 ± 0.25
	2.18 ± 0.88	0.026	3481.75 ± 0.017	9.73	1.9967	-0.28 ± 0.05	1.9965	1.09	0.83 ± 0.32
	7.66 ± 0.44	0.027	3482.96 ± 0.009	9.73	1.9960	1.06 ± 0.09	1.9966	1.00	0.90 ± 0.35
	20.97 ± 1.02	0.024	3485.34 ± 0.007	9.73	1.9946	1.30 ± 0.51	1.9953	0.90	1.04 ± 0.41
	42.62 ± 9.54	0.028	3486.79 ± 0.007	9.73	1.9938	0.88 ± 0.07	1.9943	0.85	1.16 ± 0.45
	56.79 ± 8.69	0.029	3487.05 ± 0.006	9.73	1.9936	0.98 ± 0.07	1.9942	1.06	1.68 ± 0.66

* Integrated EPR spectra maximum.
** This value pertains to the second peak formed on the shoulder of the integrated EPR spectrum.

TABLE A.2: Key parameter values for Bicron, Dubna, and Protvino.

Appendix B

Computational Parameters

B.1 EasySpin EPR Simulation Code

An example of the code used to simulate the EPR spectrum for the PolySty model with a single hydrogen atom removed is shown in Code B.1. The `pepper` function was used to simulate a CW solid-state spectrum.

Line 7 allowed for the addition of spin 1/2 particles to the system, and their principle values for the **g**- and **A**-tensor were added into the arrays in lines 8 and 10, respectively. The **g**-tensor principle values were calculated using Equation 4.17. The linewidth broadening was set to the default value using the `Sys.lw` function. The Zero-field interaction could not be computed using the GIPAW method, therefore, all components in the `Sys.ee` array were set to 0 in line 12. The sample orientation was set to that of a "powder spectrum" in line 20.

```
1  % Slow-motion spectrum of PolySty
2  %==========================================================================
3  clear, clf
4
5  % Plastic parameters, A system of 2 electrons (2 spin half) and 2 nuclei (2 *(1H, 12C
       ) ).
6  %--------------------------------------------------------------------------
7  Sys.S = [1/2 1/2];
8  Sys.g = [2.0021728677   2.0028808385    2.0030981; 2.00231920704        2.00231924168
         2.0023192243];
9  Sys.Nucs = '1H, 12C';
```

```
Sys.A = [0 0 0 0 0 0; 0 0 0 0 0 0]; % 2 electrons and 2 nuclei
Sys.lw = [0.05 0.01]; % [GaussianFWHM, LorentzianFWHM] in mT
Sys.ee = [0 0 0];

% Experimental parameters
%-----------------------------------------------------
Exp.mwFreq = 9.66;          %resonance frequency in MHz
Exp.Range = [343 346];      % Range of B-field sweep in mT
Exp.nPoints = 1024;
Exp.Temperature = 77.0; % temperature in kelvin
Exp.CrystalOrientation = []; % Powder spectrum

% Slow simulation and plotting
%-----------------------------------------------------
pepper(Sys,Exp);
```

Code B.1: EasySpin code for simulating the EPR spectrum for the PolySty model with a single H atom removed.

B.2 EPR Spectrum Averaging

The carbon atoms in each model were arbitrarily labelled with numbers. That is, the Styrene toy model had a total of 8 carbon atoms, the Vinyl toluene toy models had a total of 10 carbon atoms, the MUKLAF model had a total of 92 carbon atoms, and the PolySty model had a total of 132 carbon atoms. In each instance, the removal of a hydrogen atom was tracked by referring to the position (site) of the carbon atom on the model. This is illustrated in Figure B.1 depicting the damaged Styrene model where three hydrogen atoms are removed.

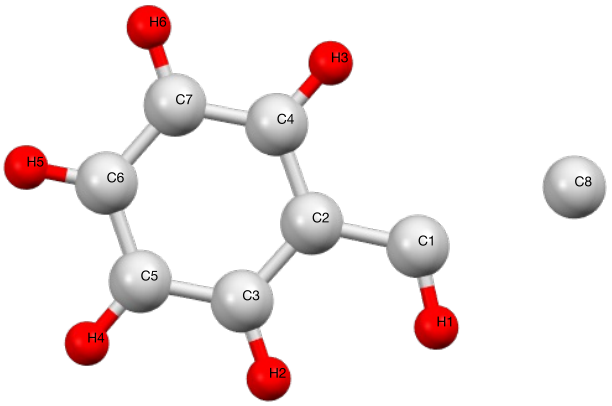

FIGURE B.1: A computer generated model of the labelled, damaged Styrene model.

Figure B.2 displays the average spectrum obtained using EasySpin for Vinyl toluene toy model with one hydrogen atom removed from various sites on the monomer. The fitting functionality is based on a spline polynomial interpolation method where the value of a curve is estimated between given data points. In total, 100 data points were used for the magnetic field range between 3440 G and 3460 G.

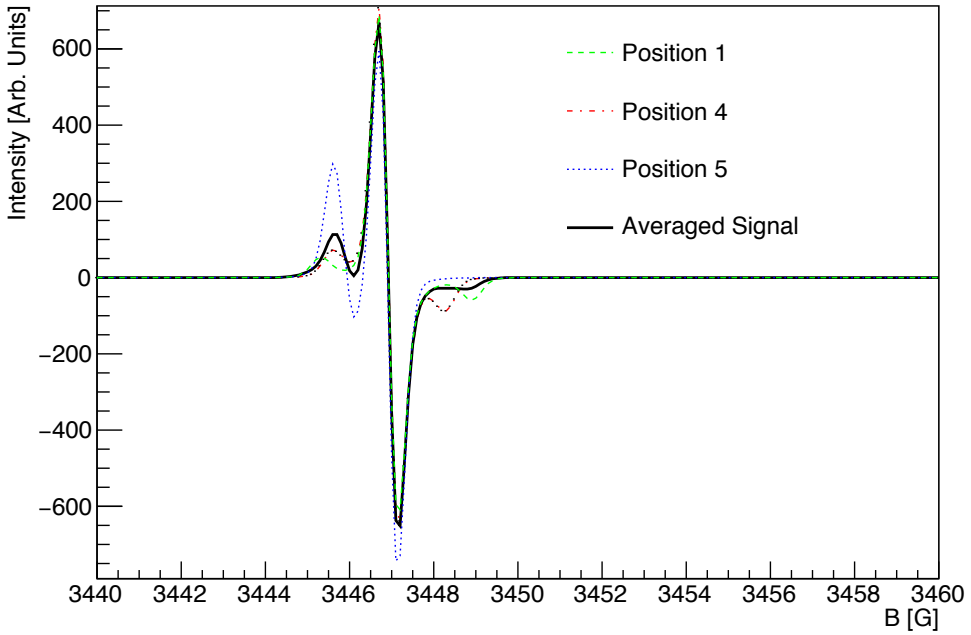

FIGURE B.2: Averaging of EPR spectrum for vinyl toluene model for a single hydrogen atom removed for various sites on the monomer.

B.3 Chemical Potential Results for Toy Model

The following tables display the absolute chemical potential (μ) and first DFT excitation values calculated for the majority and minority spin channels at the band edges. These values pertain particularly to a single Vinyl toluene model isomer. Tables B.1 and B.2 refer to the model where one and two hydrogen atoms were removed from the model, respectively. The case for the three hydrogen atom removal yields similar results. The "P" in the first column refers to the position (site) of the carbon atom where the hydrogen atom was removed. This is followed by an arbitrarily assigned number. Theses values are compared to those of the pristine values found in the first row of Table B.1.

The pseudopotentials and the absolute energies of the periodic boundary are not directly accessible in the DFT calculations. For finite system calculations, the asymptotic value of Kohn-Sham potential can be determined. By setting this value to zero, an absolute energy scale of the Kohn-Sham eigenenergies for a given exchange-correlation (XC) approximation can be established. In an extended (and a finite) system calculation, an approximate asymptotic value of the Kohn-Sham potential can be determined by using a large supercell

to approximate a surface of an infinite system and a sufficient distance from the surface to approximate an infinite distance from the surface.

The calculations presented in this section utilised a rectangular supercell with a length of 22 Å perpendicular to the monomer of the toy model to approximate the value of the asymptotic Kohn-Sham potential. The size of the supercell was sufficient to reproduce a flat region of the average potential between adjacent cells which was the criterion used to find an estimate of the asymptotic Kohn-Sham potential. In all calculations the models, pristine and damaged, were allowed to relax with all forces less than 0.01 eV/Å.

An accurate value of the asymptotic Kohn-Sham potential can only realised if the exchange-correlation potential has a reasonable asymptotic behaviour. The PBE [139] XC approximation used in this study does not have the correct asymptotic behaviour and the calculations are therefore of a quantitative nature.

H Atom Removal Position	Majority Spin Channel		Minority Spin Channel	
	μ	First DFT Excitation	μ	First DFT Excitation
Pristine	5.731350613	-2.163137613	5.731365613	-2.163161613
P1	5.724265796	-2.349297796	5.730738796	-3.287017796
P2	5.693136077	-2.289139077	5.816882077	-3.250990077
P3	5.755768040	-2.191957040	5.723135040	-3.281224040
P4	5.676272334	-2.274055334	5.850315334	-3.234396334
P5	4.660611952	-2.123890952	5.957405952	-3.553795952
P6	4.660635785	-2.134112785	5.955678785	-3.554259785
P7	4.659659778	-2.113428778	5.965345778	-3.550262778
P8	4.264953891	-1.414295891	6.180995891	-3.231643891
P9	5.705187970	-2.209081970	5.741396970	-3.184946970
P10	5.718511584	-2.330352584	5.676437584	-3.233590584

Table B.1: Chemical potential and the absolute value of first DFT excitation for both majority and minority spin channels for the single hydrogen atom removal in the Vinyl toluene model.

H Atom Removal Position	Majority Spin Channel		Minority Spin Channel	
	μ	First DFT Excitation	μ	First DFT Excitation
P1 and P2	5.583055909	-2.930537909	5.583079909	-2.930483909
P1 and P3	5.539595907	-2.171706907	5.539611907	-2.171701907
P1 and P4	5.296416139	-2.266576139	5.630483139	-3.360265139
P1 and P5	4.541534601	-2.151697601	5.659170601	-3.475705601
P1 and P6	4.548662953	-2.159836953	5.663707953	-3.482786953
P1 and P7	4.581041969	-2.209577969	5.699055969	-3.515999969
P1 and P8	4.442024027	-1.465137027	6.243828027	-3.286812027
P1 and P9	5.796083335	-2.455880335	5.781059335	-3.464748335
P1 and P10	5.618933192	-2.443129192	5.788888192	-3.493222192
P2 and P3	5.991795506	-3.319956506	5.991819506	-3.320072506
P2 and P4	5.463388989	-2.650764989	5.463422989	-2.650704989
P2 and P5	4.667531527	-2.209803527	6.057033527	-3.437244527
P2 and P6	4.623785076	-2.164144076	6.019036076	-3.395711076
P2 and P7	4.667415174	-2.197171174	6.064917174	-3.434036174
P2 and P8	4.453546245	-1.530539245	6.228350245	-3.475414245
P2 and P9	5.534915647	-2.294470647	5.790614647	-3.400823647
P2 and P10	5.634978049	-2.580442049	5.903824049	-3.627729049
P3 and P4	5.578582897	-3.003574897	5.578639897	-3.003622897
P3 and P5	4.472004143	-1.853665143	5.667689143	-3.398061143
P3 and P6	4.463156625	-1.856771625	5.652891625	-3.389161625
P3 and P7	4.469853514	-1.844617514	5.669379514	-3.393706514
P3 and P8	4.153281946	-1.417121946	6.174720946	-3.052280946
P3 and P9	5.417060622	-1.967735622	5.465285622	-3.047897622
P3 and P10	5.602057223	-2.241497223	5.549859223	-3.316911223
P4 and P5	4.608240721	-2.030316721	5.868163721	-3.392431721
P4 and P6	4.610469614	-2.053752614	5.859958614	-3.396660614
P4 and P7	4.642714849	-2.051132849	5.910036849	-3.421306849
P4 and P8	4.241303095	-1.281254095	6.035579095	-3.247700095
P4 and P9	5.317415746	-2.092940746	5.629083746	-3.257580746
P4 and P10	5.574247472	-2.252841472	5.605083472	-3.195948472
P5 and P6	4.603064137	-2.073834137	5.838760137	-3.227873137
P5 and P7	4.645736069	-2.251997069	5.813160069	-3.277880069
P5 and P8	4.657775657	-2.855602657	4.657807657	-2.855602657
P5 and P9	4.424706881	-1.948268881	5.650198881	-3.297644881
P5 and P10	4.510721317	-2.131710317	5.668421317	-3.347373317
P6 and P7	4.594534920	-2.099610920	5.811938920	-3.221910920
P6 and P8	4.666388480	-2.862085480	4.666415480	-2.862081480
P6 and P9	4.417956667	-1.952809667	5.630634667	-3.290125667
P6 and P10	4.563352873	-2.200427873	5.721516873	-3.401440873
P7 and P8	4.662768148	-2.855421148	4.662797148	-2.855419148
P7 and P9	4.419624805	-1.967043805	5.626703805	-3.282468805
P7 and P10	4.511574696	-2.133871696	5.669454696	-3.346841696
P8 and P9	5.744031311	-1.949627311	5.744037311	-1.949623311
P8 and P10	5.739585484	-1.939336484	5.739586484	-1.939324484
P9 and P10	5.728275461	-1.934095461	5.728284461	-1.934094461

TABLE B.2: Chemical potential and the absolute value of first DFT excitation for both majority and minority spin channels for the two hydrogen atom removal in the Vinyl toluene model.

Appendix C

Performance of $E_{\mathrm{T}}^{\mathrm{miss}}$ in the Search for a Higgs boson with a Di-photon Decay at $\sqrt{s} = 13$ TeV

This appendix summarises the performance of the missing transverse energy, $E_{\mathrm{T}}^{\mathrm{miss}}$, in the study searching for a Higgs boson reconstructed as two photons at large $E_{\mathrm{T}}^{\mathrm{miss}}$ at $\sqrt{s} = 13$ TeV for the ATLAS detector [10]. Monte Carlo (MC) simulations are used to evaluate the performance of $E_{\mathrm{T}}^{\mathrm{miss}}$ using a track-based method. This definition is reconstructed from the energy deposits resulting from pp collisions at $\sqrt{s} = 13$ TeV within the ATLAS detector.

The motivation for this study has already been presented is Section 1.1. The EPR investigation aimed to study the structural damage incurred by the plastics in the low energy (MeV) region. Any missing energy detected by ATLAS can give an indication of the damage to the plastics (and is seen as a mismeasurement by the plastics). However, any effects of damage is minimized during the calibration of the detector before data taking. In order to understand the detector performance at large energies, a study of missing energy is necessary above calibration levels.

This appendix is divided into six sections. The theoretical model is introduced in Section C.1. Aspects regarding the data and simulated samples are briefly discussed in Section C.2.

The reconstruction of objects and their identification are discussed in Section C.3, with a particular focus placed on $E_{\mathrm{T}}^{\mathrm{miss}}$ and its reconstruction. The categorisation and event selection is discussed in Section C.4. The results pertaining to the $E_{\mathrm{T}}^{\mathrm{miss}}$ reconstruction and a brief discussion regarding the overall study are presented in Section C.5. Finally conclusions are drawn in Section C.6.

C.1 The Madala Hypothesis

A theoretical heavy scalar model, referred to as the Madala hypothesis, introduces the so-called Madala boson, H, which is mainly produced via gluon-gluon fusion. The Madala hypothesis allows for the study of the Higgs, h, and large $E_{\mathrm{T}}^{\mathrm{miss}}$ through the decay of the Madala boson to h and two dark matter candidates χ. The production and decay of H are represented in Figures C.1a and C.1b, respectively. These interactions are described by an effective Beyond Standard Model (BSM) theory [9].

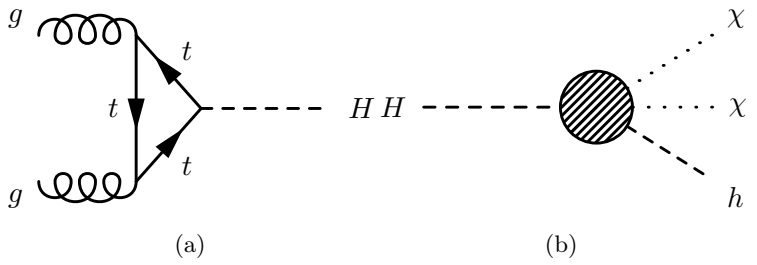

FIGURE C.1: The production mechanism of H via gluon-gluon fusion (a), and the decay of H to two dark matter candidates, χ, and a Higgs boson, h. Obtained from [10].

A large branching ratio (BR) for Figure C.1b was assumed since χ originates via another heavy scalar S [9]. The mass of H and χ (denoted m_H and m_χ, respectively) along with the large BRs were free parameters in the model.

C.2 Data and Sample Simulation

Data samples from 2015 data sets describing pp collisions with 25 ns bunch crossings at $\sqrt{s} = 13$ TeV were used. Events were collected under stable beam conditions and operational

sub-detectors. The di-photon was trigger required two reconstructed photons: the leading photon was required to have a transverse energy of 35 GeV. The sub-leading photon was required to have a transverse energy of at least 25 GeV. These events were selected at an integrated luminosity of 3.2 fb^{-1}. The gluon-gluon fusion MC simulations were performed with MADGRAPH [140] at leading order, and the parton shower and hadronisation were simulated using PYTHIA8.186 [141]. A mass scan was done for the decaying process for m_H in intervals of 10 GeV from 260 GeV to 350 GeV, and an additional mass of 275 GeV was added to the scan. Two m_χ masses were chosen for the study, namely 50 GeV and 60 GeV.

C.3 Reconstruction and Identification of Objects

C.3.1 Jet Selection

The selection of jets required that they be reconstructed from topological clusters in both the EM and hadronic calorimeters using the anti-k_t algorithm. A clustering radius of $R = 0.4$ was used and jets were required to have a p_{T} larger than 25 GeV in a region $|\eta|$ larger than 4.4.

C.3.2 Photon Selection

Photon identification makes use of different evolutions of EM showers whose energy is deposited into the EM calorimeter with no track formation. In order for photons to be considered, they required a p_{T} larger than 25 GeV, to satisfy the "loose" identification [142] in a region of $|\eta|$ greater than 2.37, and satisfy the "tight" classification.

C.3.3 Lepton Selection

Electrons are reconstructed from energy deposits in the EM calorimeter associated with Inner Detector (ID) tracks. They are required to be in a region of $|\eta|$ smaller than 2.47, and have a p_{T} smaller than 10 GeV. Muons are reconstructed from the muon spectrometer segments to ID tracks in a region $|\eta|$ smaller than 2.7 and must have a p_{T} greater than 10 GeV.

C.3.4 Overlap removal

Objects too close too each other are removed. That is, leptons with a $\Delta R = 0.4$ between photons or jets are removed.

C.3.5 $E_{\mathrm{T}}^{\mathrm{miss}}$ Reconstruction

Missing transverse energy, $E_{\mathrm{T}}^{\mathrm{miss}}$, is defined as an imbalance in the sum of visible momenta transverse to the beam axis. It is reconstructed from objects that are calibrated to estimate the imbalance in transverse momentum for a given event; this is calculated for each event and is the sum of a number of components [143].

$$E_{x(y)}^{\mathrm{miss}} = E_{x(y)}^{\mathrm{miss},e} + E_{x(y)}^{\mathrm{miss},\gamma} + E_{x(y)}^{\mathrm{miss},\tau} + E_{x(y)}^{\mathrm{miss,jets}} + E_{x(y)}^{\mathrm{miss},\mu} + E_{x(y)}^{\mathrm{miss,soft}} \tag{C.1}$$

The terms in Equation C.1 referring to the jets, charged leptons, and photons are calculated from the negative sum of their momenta. The "hard" terms referring to the electrons (e), photons (γ), tau-leptons which decay hadronically (τ), jets, and muons (μ) are deposited in the calorimeter and are associated to the reconstructed objects. The last term in Equation C.1 is the so-called "soft" term and is not associated with the previous terms. Instead, it reconstructed from transverse momenta deposits in the detector. In this study, the track-based method is utilised, which results in a Track Soft Term (TST) [144]. Other algorithms do exists which are calorimeter-based; the choice of algorithm alters the performance and uncertainties of the $E_{\mathrm{T}}^{\mathrm{miss}}$ [143]. The $E_{\mathrm{T}}^{\mathrm{miss}}$ is calculated as follows:

$$E_{\mathrm{T}}^{\mathrm{miss}} = \sqrt{\left(E_{x}^{\mathrm{miss}}\right)^2 + \left(E_{y}^{\mathrm{miss}}\right)^2} \tag{C.2}$$

from the x and y components, and furthermore, the azimuthal angle ϕ^{miss} is calculated by taking the arctan ratio of the E_{y}^{miss} over E_{x}^{miss}. Finally, to quantify an event, the scalar sum over the total transverse energy of the event is calculated.

C.3.5.1 Track Soft Term

The track soft terms are calculated from energy deposits in the ID which are reconstructed as tracks. These tracks form as a result of pp collisions which result in a multitude of diffractive energetic particles. The tracks are reconstructed into vertices associated with the hard scatter

vertex, and are matched to the primary vertex. The TST algorithm is relatively sensitive to pile-up and does not include soft interactions from neutral particles for $|\eta|$ greater than 2.5.

C.4 Event Selection and Categorisation

Two photon candidates are selected within the Higgs mass window 105 GeV $< m_{\gamma\gamma} <$ 160 GeV. Categorisations were according to the $E_{\mathrm{T}}^{\mathrm{miss}}$, $p_{\mathrm{T}}^{\mathrm{hard}}$ (the transverse components of the vector sum of photons and jets), and $p_{\mathrm{T}}^{\gamma\gamma}$ phase spaces. The categories are optimised using the MC samples and are summarised in Table C.1

Category	$\mathrm{E}_{\mathrm{T}}^{\mathrm{miss}}$ (GeV)	$p_{\mathrm{T}}^{\mathrm{hard}}$ (GeV)	$p_{\mathrm{T}}^{\gamma\gamma}$ (GeV)
High $\mathrm{E}_{\mathrm{T}}^{\mathrm{miss}}$, high $p_{\mathrm{T}}^{\gamma\gamma}$	> 100	-	> 100
High $\mathrm{E}_{\mathrm{T}}^{\mathrm{miss}}$, low $p_{\mathrm{T}}^{\gamma\gamma}$	> 100	-	≥ 100
Intermediate $\mathrm{E}_{\mathrm{T}}^{\mathrm{miss}}$	> 50 and ≥ 100	> 40	-
Rest	-	-	> 15

Table C.1: The four optimised categories utilised in the study. Obtained from [10].

C.5 Results

A number of control plots are presented pertaining to the components of the $E_{\mathrm{T}}^{\mathrm{miss}}$ reconstruction. Five categories are considered: the Inclusive category, the High $E_{\mathrm{T}}^{\mathrm{miss}}$ category with a high p_{T} cut, the High $E_{\mathrm{T}}^{\mathrm{miss}}$ category with a low p_{T} cut, the Intermediate $E_{\mathrm{T}}^{\mathrm{miss}}$ category, and the Rest category (see Table C.1). The plots shown are for the different variables in TST.

C.5.1 $E_{\mathrm{T}}^{\mathrm{miss}}$ Muon TST Distribution

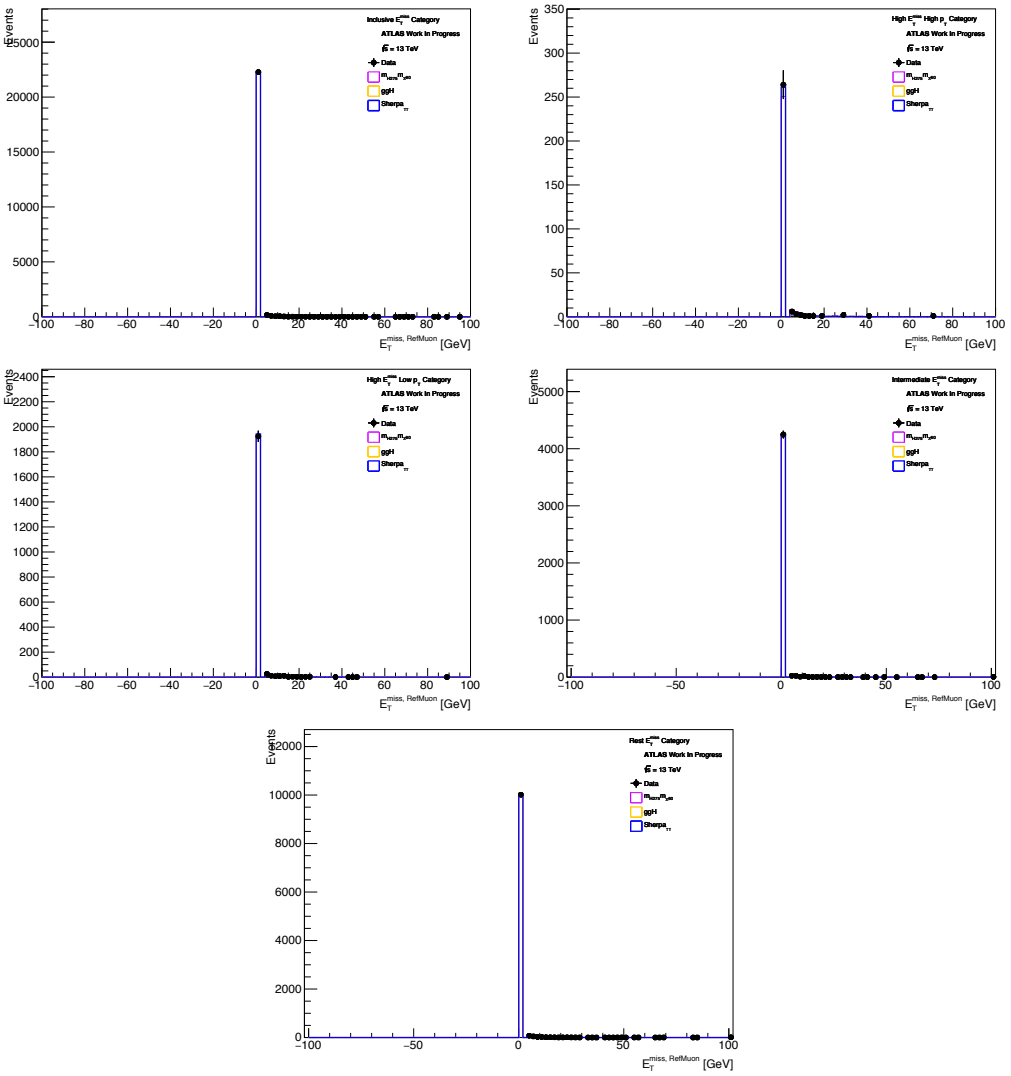

FIGURE C.2: Control plots for the TST terms for the total $E_{\mathrm{T}}^{\mathrm{miss}}$ muon distribution.

C.5.2 $E_{\mathrm{T}}^{\mathrm{miss}}$ RefTau TST Distribution

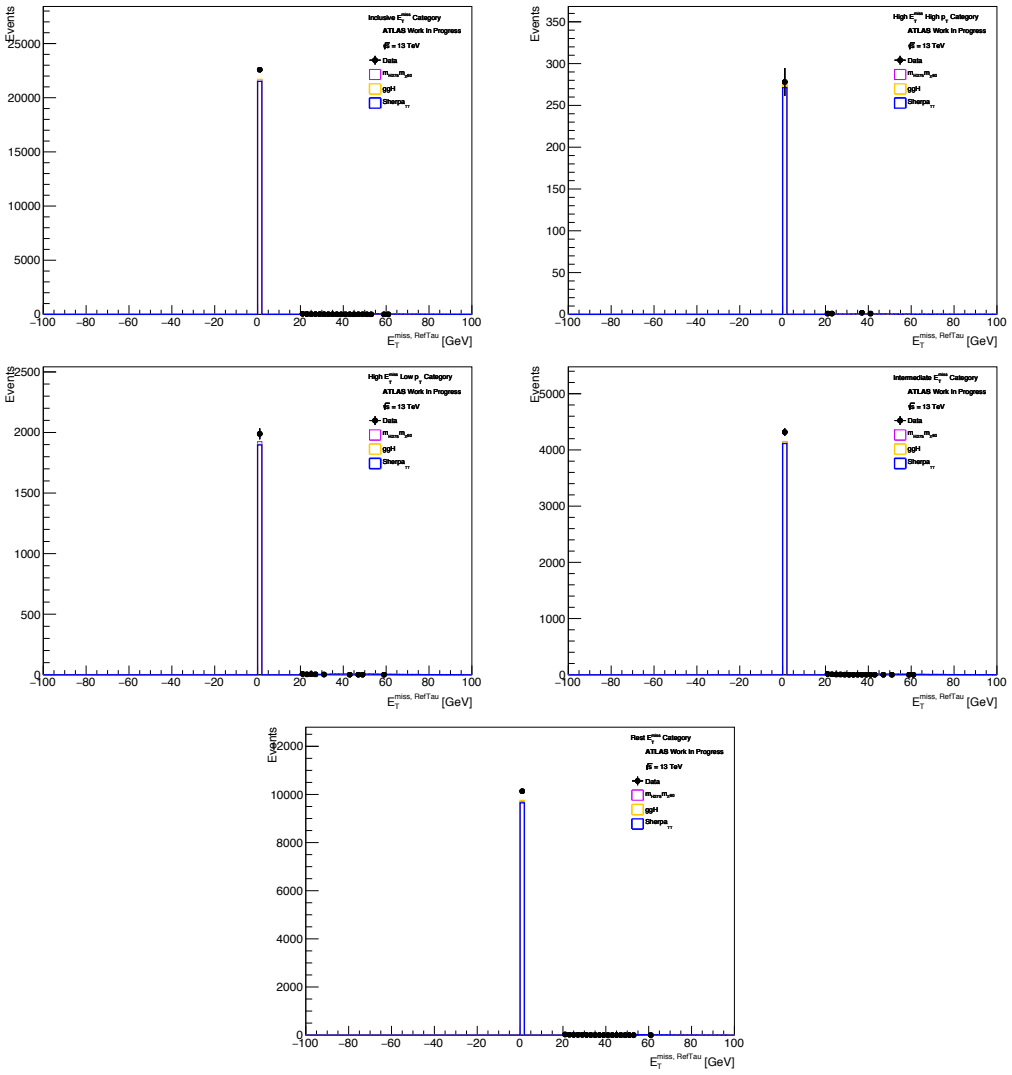

FIGURE C.3: Control plots for the TST terms of the $E_{\mathrm{T}}^{\mathrm{miss}}$ RefTau distribution.

Figures C.2 and C.3 show the distribution plots for the RefMuon and RefTau terms. The data were normalised and compared to MC. Delta-like distributions can be seen for these terms.

C.5.3 $E_{\mathrm{T}}^{\mathrm{miss}}$ RefEle TST Distribution

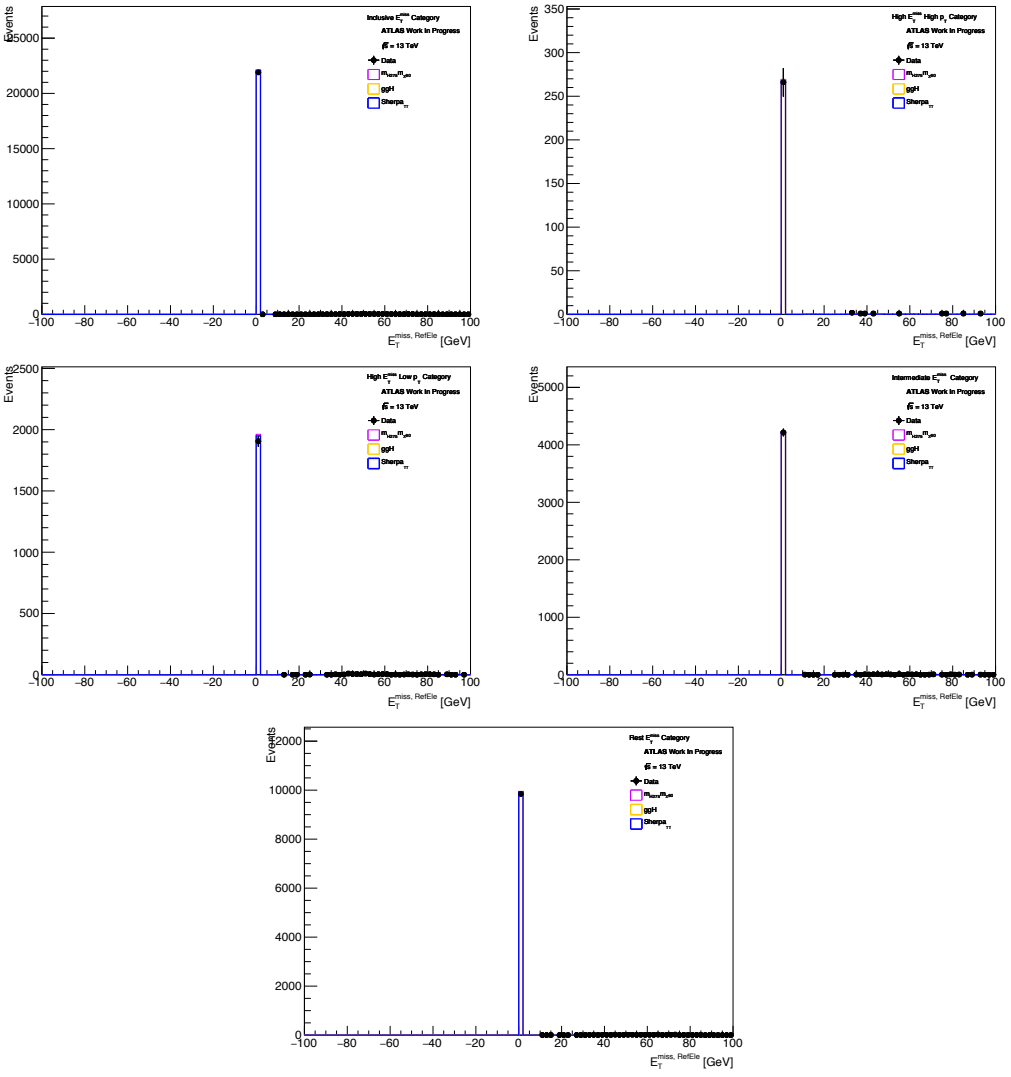

FIGURE C.4: Control plots for the TST terms of the $E_{\mathrm{T}}^{\mathrm{miss}}$ RefEle distribution.

Figure C.4 show the distribution plots for the RefEle terms. The data were normalised and compared to MC. Delta-like distributions can be seen for these terms.

C.5.4 $E_{\mathrm{T}}^{\mathrm{miss}}$ RefGamma TST Distribution

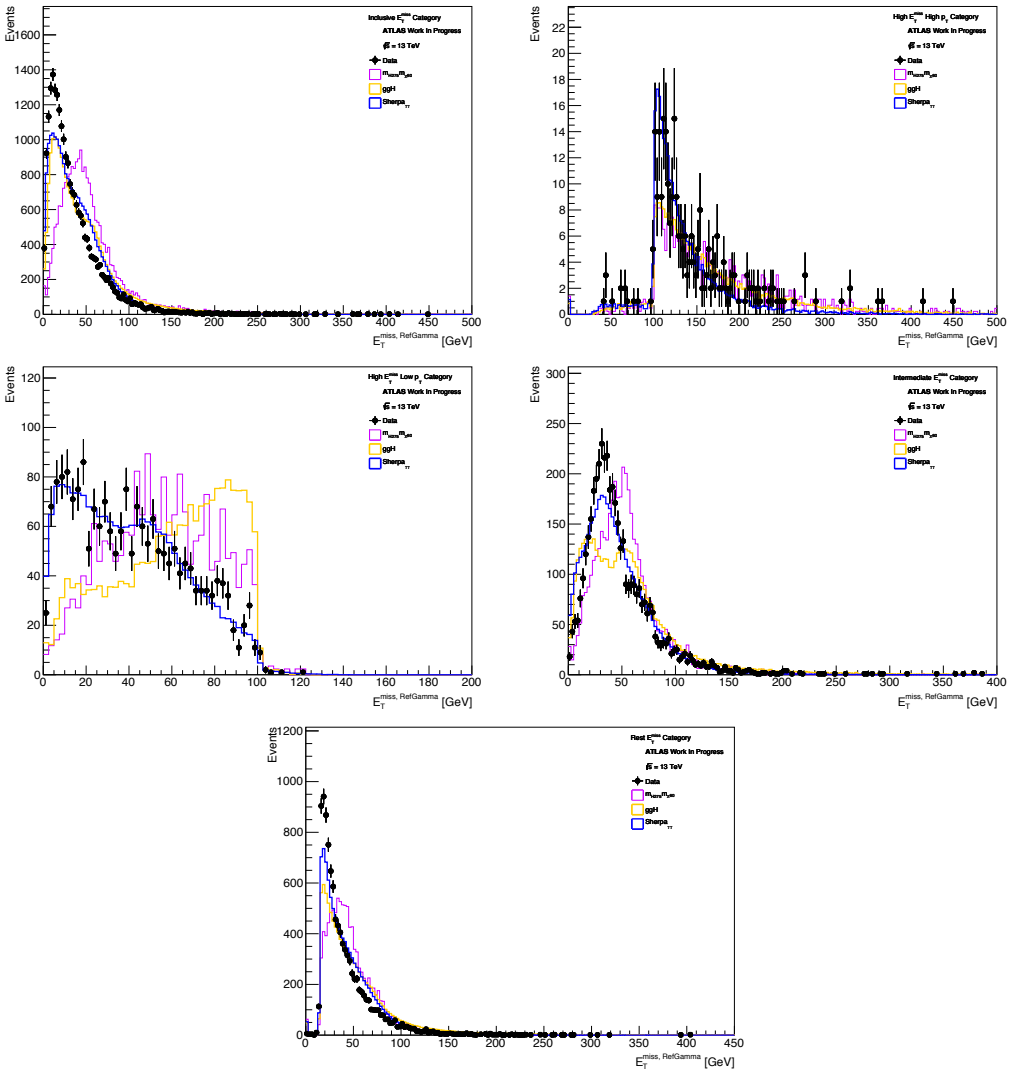

FIGURE C.5: Control plots for the TST terms for the total component of $E_{\mathrm{T}}^{\mathrm{miss}}$ RefGamma distribution.

The total distributions are shown for the RefGamma terms above and show a skewed distribution. There is little correlation between data and MC.

C.5.5 $E_{\mathrm{T}}^{\mathrm{miss}}$ RefJet TST Distribution

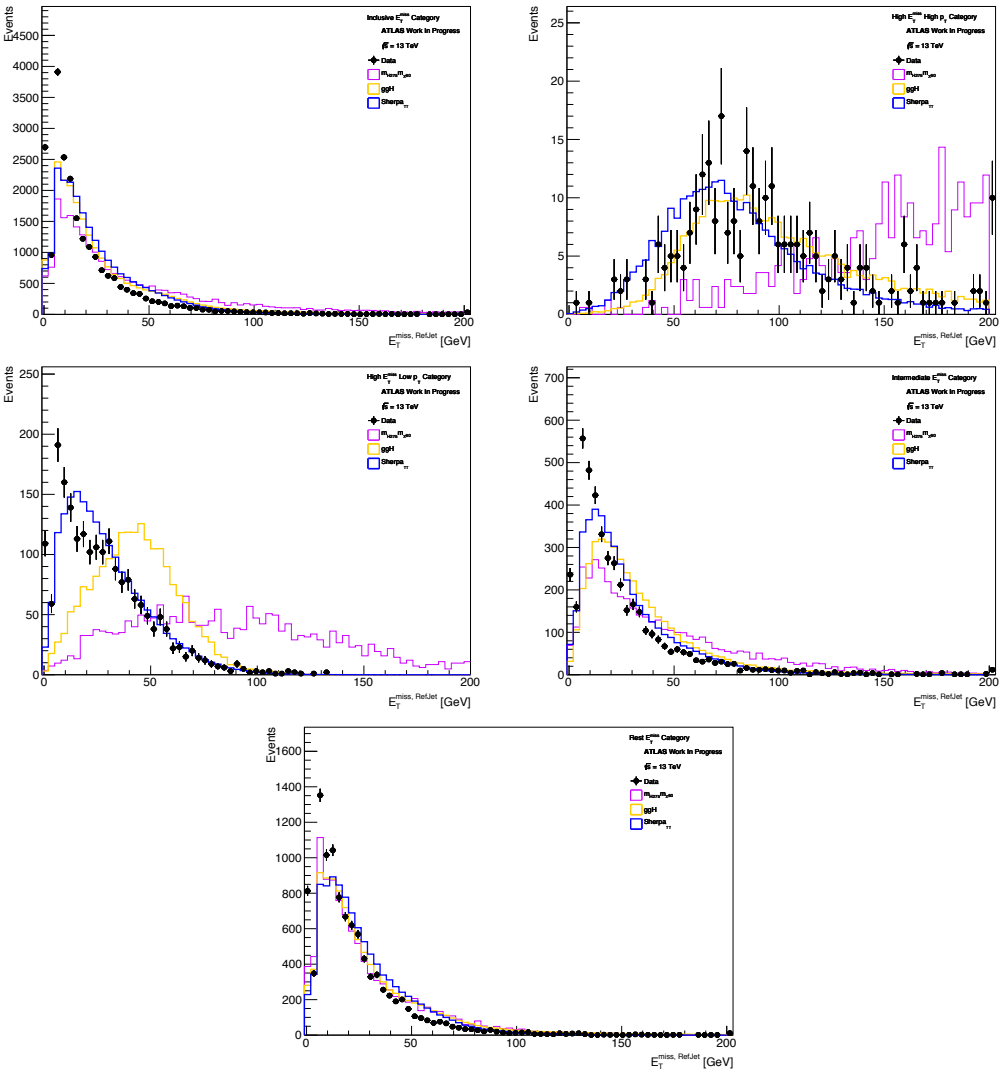

FIGURE C.6: Control plots for the TST terms for the total component of $E_{\mathrm{T}}^{\mathrm{miss}}$ RefJet distribution.

The figures shown above are distributions for the RefJet terms where the shape of data in compared the the different MC samples. Skewed distributions can be seen where data and MC do not comply completely.

C.5.6 $E_{\mathrm{T}}^{\mathrm{miss}}$ Total TST Distribution

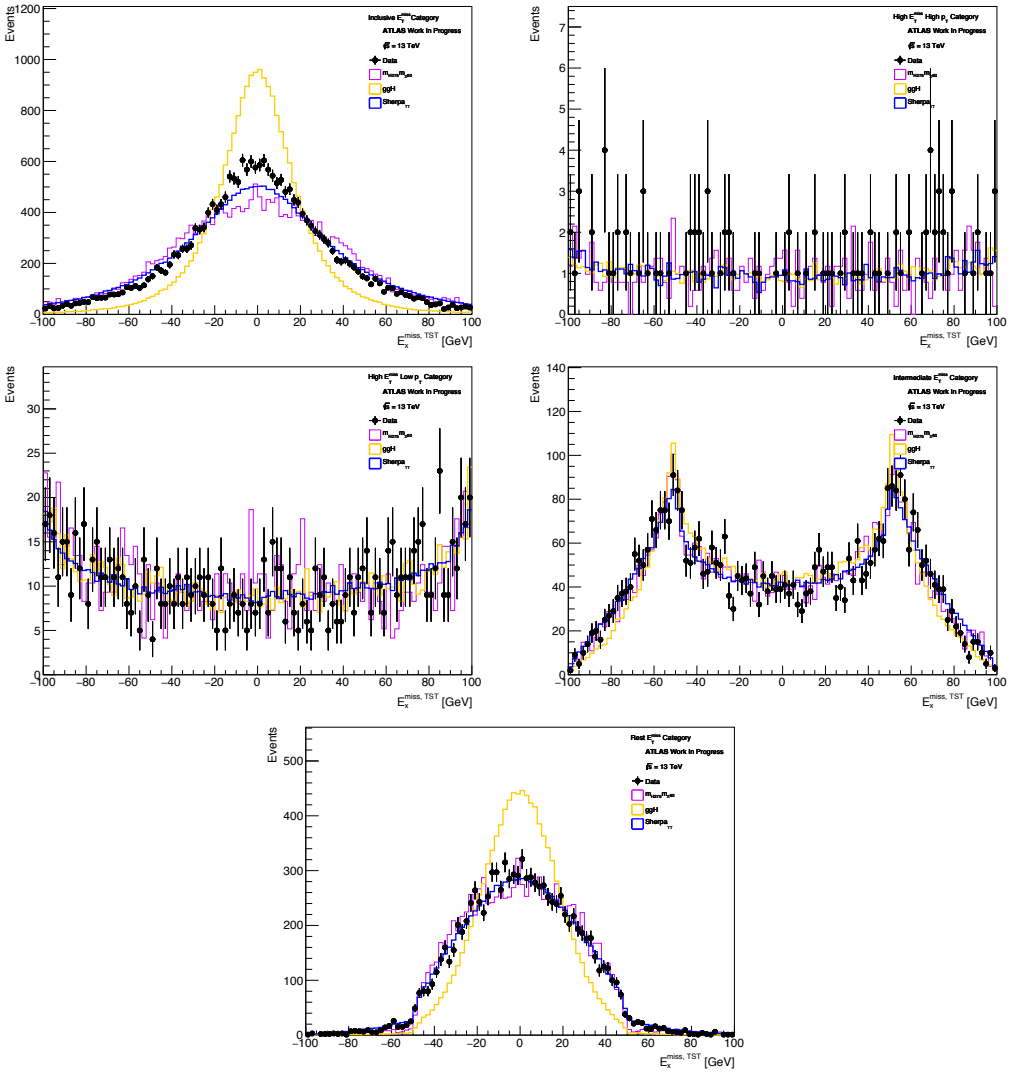

FIGURE C.7: Control plots for the TST terms for x-component of $E_{\mathrm{T}}^{\mathrm{miss}}$ Total distribution.

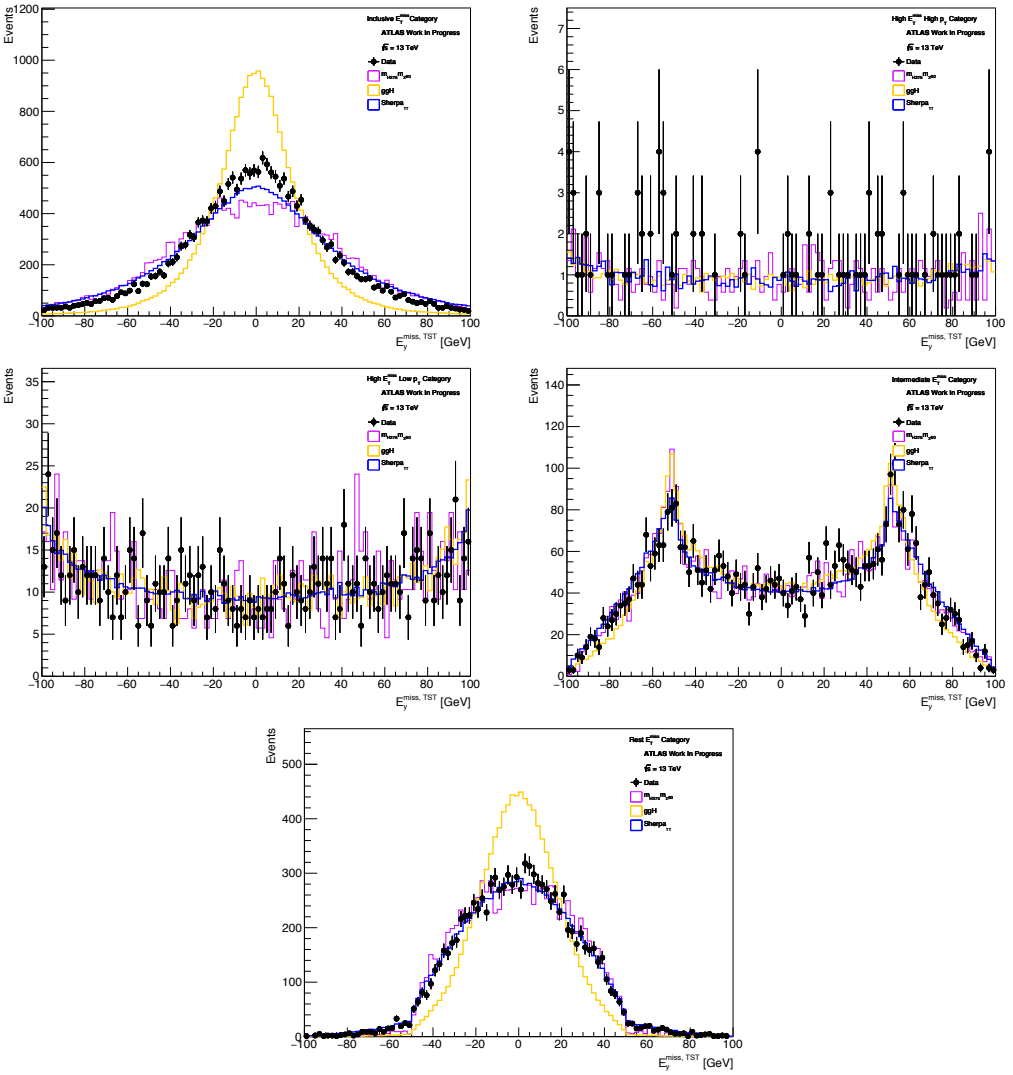

FIGURE C.8: Control plots for the TST terms for y-component of $E_{\mathrm{T}}^{\mathrm{miss}}$ Total distribution.

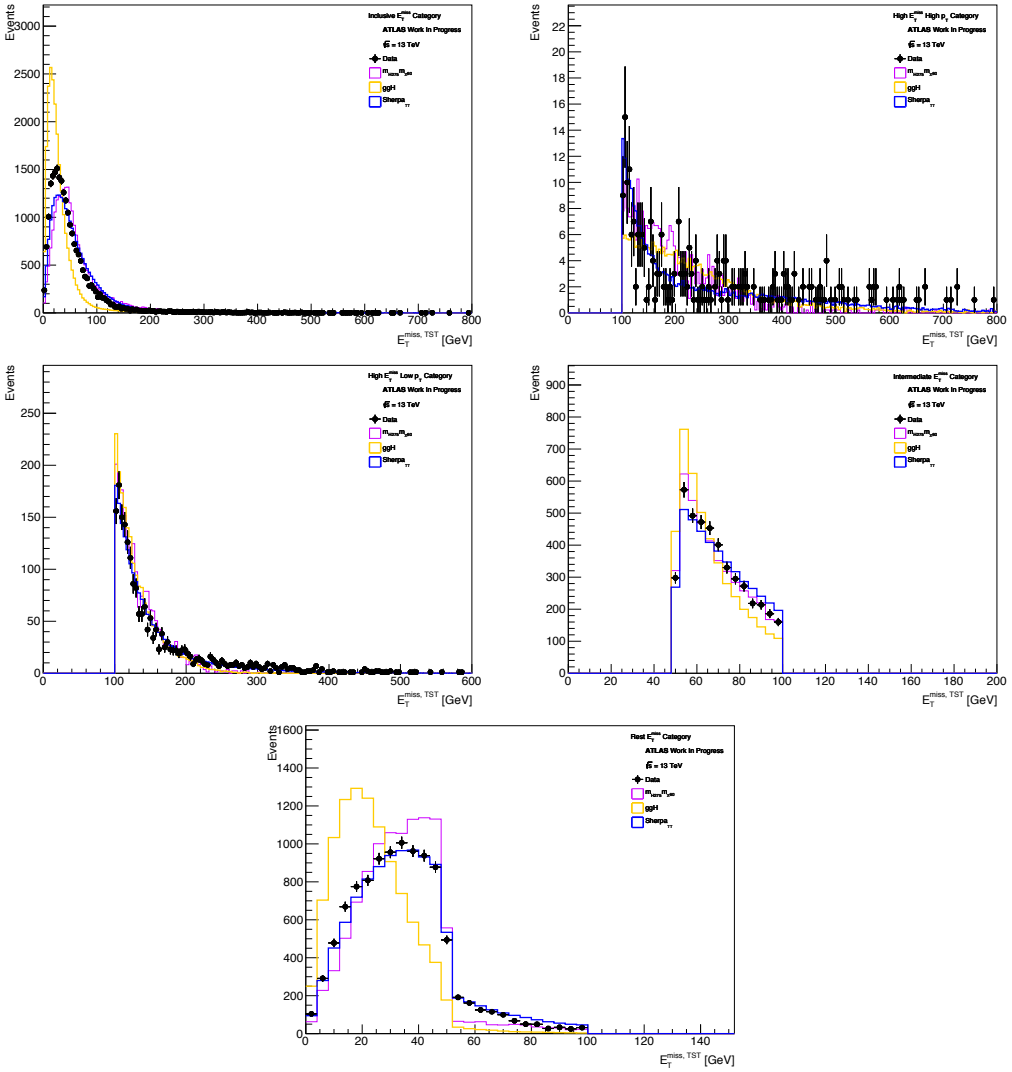

FIGURE C.9: Control plots for the TST terms for the total component of $E_{\mathrm{T}}^{\mathrm{miss}}$ Total distribution.

The total $E_{\mathrm{T}}^{\mathrm{miss}}$ TST distributions in all five categories are shown in Fig. C.9. The x- and y-components, shown in Figs. C.7 and C.8, are shown.

C.5.7 Sum of $E_{\mathrm{T}}^{\mathrm{miss}}$ for TST

Finally, presented are the plots for the summated $E_{\mathrm{T}}^{\mathrm{miss}}$ in TST for the five different categories. It is evident that there are very different distributions for data and MC.

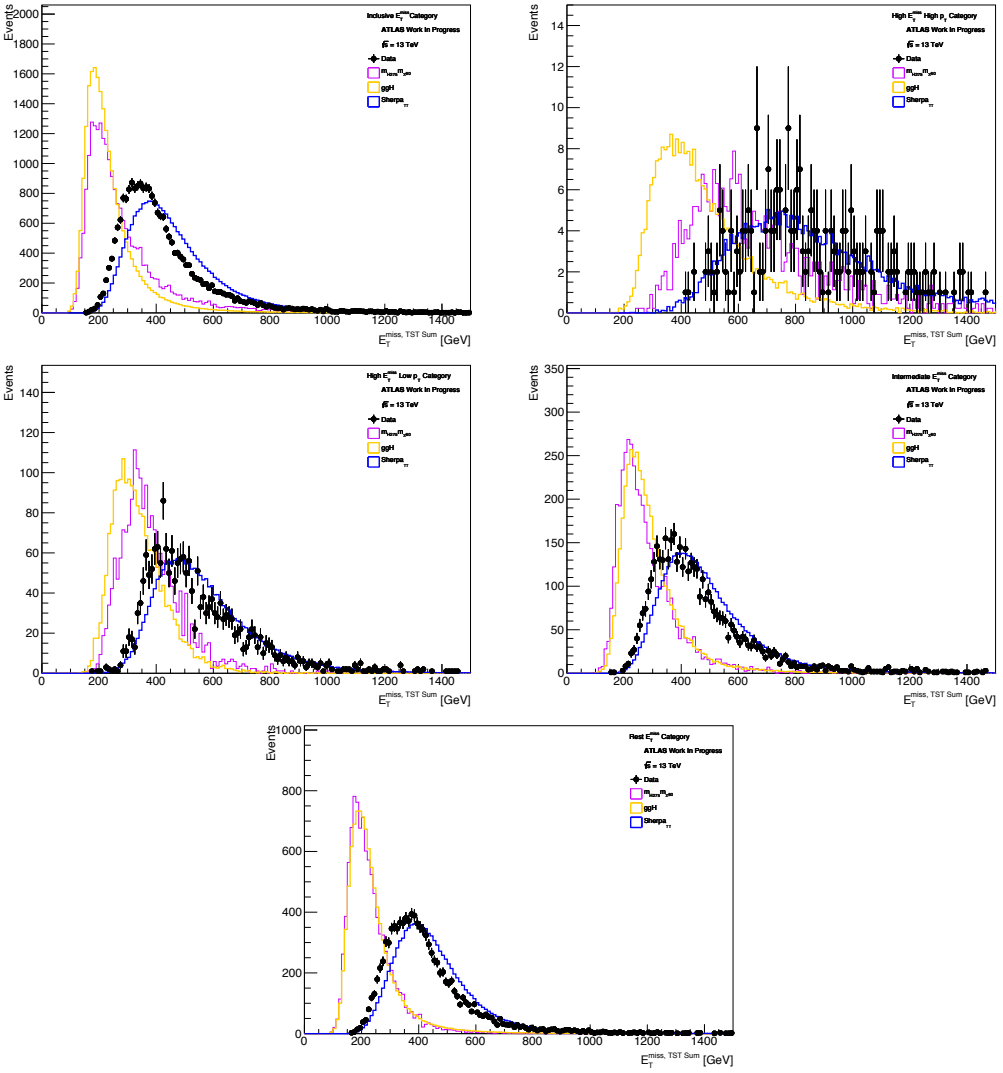

FIGURE C.10: Control plots for the TST terms for the sum of $E_{\mathrm{T}}^{\mathrm{miss}}$ distributions.

C.6 Conclusion

The expected performance of the $E_{\mathrm{T}}^{\mathrm{miss}}$ and its distributions are presented and discussed for the study searching for Higgs boson reconstructed as two photons and large $E_{\mathrm{T}}^{\mathrm{miss}}$ for pp collisions at $\sqrt{s} = 13$ TeV for the ATLAS detector. Conclusions regarding the study were as follows: no significant excess over the background expectation was observed. In the Madala hypothesis, a 95% CL upper limit of 29.6 fb was set on the production and cross section and BR for the Higgs to have a di-photon final state.